Physik-Department

A Liquid-Argon anti-Compton Veto with Silicon Photomultipliers

Diplomarbeit von Hossein Aghai-Khozani

München, den 17. November 2010

Max-Planck-Institut für Physik
(Werner-Heisenberg-Institut)

Technische Universität München

Abstract

One of today's most important open questions in particle physics is whether neutrinos are their own anti-particles as required by most extensions of the Standard Model. Currently the neutrinoless double beta decay is the most sensitive approach to answer this question. The GERDA experiment is designed to search for the neutrinoless double beta decay in ^{76}Ge. The main design feature of GERDA is the operation of bare germanium detectors enriched in ^{76}Ge in liquid argon (LAr). In its first phase GERDA is supposed to be operated with 17.66kg of target material and a background index of 10^{-2}events/(kg keV year). In phase two new germanium detectors will be added. The background index for this phase is aimed to be 10^{-3}events/(kg keV year) using additional background reduction techniques.

LAr scintillates in the UV (λ=128 nm) and a novel concept is to use this scintillation light as anti-Compton veto for background suppression in the germanium detectors. It was already shown that with a LAr anti-Copmton veto using photo multiplier tubes (PMTs) more than an order of magnitude background suppression in germanium detectors can be achieved.

However conventional PMTs contain components that have significant radioactive impurities and are thus not well suited for a low background experiment like GERDA.

A novel photon detection device, the silicon photo multiplier (SiPM), could be an alternative LAr scintillation light detection solution. Its small mass and the materials it is made of suggest that its contribution to the radioactive background is low.

In this work SiPMs are characterized at cryogenic temperatures. It is shown they can be operated with negligible dark rate and high gain at cryogenic temperatures.

It is further demonstrated that SiPMs are suited for LAr scintillation light detection. A small scale experiment is presented that demonstrates a reasonably high light collection efficiency of about ~90p.e./MeV energy deposit. With the setup being used as an anti-Compton veto for a high purity germanium detector, the ^{228}Th background in the detector was suppressed by a factor 4.2 around $Q_{\beta\beta}$ of ^{76}Ge.

Zusammenfassung

Eine der wichtigesten offenen Fragen der modernen Teilchenphysik is, ob Neutrinos ihre eigenen Antiteilchen sind. Momentan bietet der neutrinolose Doppelbetazerfall die höchste Sensitivität, um diese Frage zu überprüfen. Das GERDA Experiment wurde für die Suche nach dem neutrinolosen Doppelbetazerfall in ^{76}Ge entworfen. Hierzu sollen hochreine Germaniumdetektoren nackt in flüssigem Argon betrieben werden. In Phase I des Experiments soll GERDA einen Untergrundindex von 10^{-2}Ereignissen/(kg keV Jahr) erreichen. In Phase II soll unter Zuhilfenahme weiterer Untergrunderkennungsverfahren ein Index von 10^{-3}Ereignissen/(kg keV Jahr) erreicht werden.
Flüssiges Argon szintilliert (λ=128 nm) und daher sollen in einem neuen Untergrunderkenugskonzept Argon Szintillationslicht und Germaniumdetektoren, die in Argon betrieben werden, simultan ausgelesen werden. Unter Verwendung von Photoelektronvervielfachern (PMT) wurde so bereits eine effektive Erkennung des Untergrundes nachgewiesen. Daraus resultierend konnte der Thoriumuntergrund im Energiebereich um $Q_{\beta\beta}$ um über einer Größenordnung unterdrčkt werden.
Jedoch sind PMTs aufgrund ihrer radioaktiven Bestandteile ungeeignet für die Verwendung im GERDA Experiment.
Silliziumphotoelektronvervielfacher (SiPM) sind eine neue Art von Photosensoren und könnten eine alternative Detektionsmöglichkeit des flüssig Argon Szintillationslicht darstellen. Ihre kleine Masse legt eine geringe Radioaktivität nahe.
In dieser Arbeit werden SiPMs bei kryogenen Temperaturen charakterisiert. Es wird gezeigt, dass SiPMs bei geringen Temperaturen mit vernachlässigbarer Dunkelrate und einem hohen Verstärkunsfaktor betrieben werden können. Des weiteren wird demonstriert, dass SiPMs geignet für die Detektion des Szintillationlichts in flüssigem Argon sind. Hierzu wird ein kleinformatiges Experiment präsentiert, welches eine Lichtsammeleffizienz von ~90p.e./MeV Energiedeposition aufweist. Es wird gezeigt, dass der Aufbau als Anticomptonveto für ein Germaniumdetektor fungieren kann, welches Unterdrückung des Thoriumuntergrundes im Bereich um $Q_{\beta\beta}$ von 4,2 erreicht.

Contents

Chapter 1

Introduction

Research in elemental particle physics is carried out to investigate the fundamental constituents of matter and the forces between them. In the past decades a series of experiments and theories has helped to build up a theoretical framework, the so called Standard Model of particle physics, that describes our observations with an unprecedented precision. Only lately the observation of neutrino oscillations has opened an experimental window to new physics that cannot be explained within the Standard Model.

One of the interesting questions of this new physics is whether the neutrino is its own antiparticle, i.e. Majorana particle. Currently the only feasible approach to investigate this question is the neutrinoless double beta decay ($0\nu\beta\beta$), a lepton number violating weak process. Only if the neutrino is indeed a Majorana particle this process could exist. So far no experiment could find undoubted evidence for this process.

Among all possible target materials for the $0\nu\beta\beta$, ^{76}Ge is the of the most promising as it allows to produce detectors with excellent energy resolution out of it. The GERmanium Detector Array (GERDA) experiment, currently being commissioned, is built for the search for $0\nu\beta\beta$ with high purity germanium (HPGe) detectors enriched in ^{76}Ge. GERDA's main design feature is the operation of bare HPGe detectors in liquid argon (LAr). The LAr simultaneously acts as passive shielding and cryogenic cooling liquid.

One of the biggest challenges of GERDA is to achieve a background that is smaller than the expected signal. A reduction of the background can be achieved by adding shielding to the experiment and by careful selection of the components. After the limit imposed by the radioactivity of the cleanest materials available will be reached further reduction is only possible via background identification.

The main source of background for GERDA is the radioactivity of the surrounding material. Gammas that deposit energy in HPGe detector in the energy region of interest undergo predominantly Compton scattering. These gammas often deposit only part of their energy before escaping the detector. For such events there is a high probability the escaping gammas deposit their energy in the LAr environment. LAr like all noble liquids is an excellent scintillator. If the scintillation light that the escaping gamma produces in the LAr is detected, events with partial energy deposition in the LAr can be identified. Such an arrangement is called an anti-Compton veto because it can suppress

the Compton background between gamma lines.
The possibility to use the scintillation light as an anti-Compton veto for the HPGe detectors is unexploited in the current design of GERDA. In [1] it was shown that with a LAr anti-Compton veto for some radiation sources more than an order of magnitude background suppression can be achieved around the energy region of interest. Such a huge improvement could be decisive for the success of GERDA if it could be realized without increasing the radioactive background or changing the original design too much.

Conventionally LAr scintillation light is detected with Photo-Multiplier Tubes (PMTs). PMTs would have some disadvantages in the current GERDA design. They are not well suited for a cryogenic environment and they contain components such as glass which typically have significant radioactive impurities.
A novel photon detection device, the multipixel avalanche photodiode commonly called Silicon Photo-Multiplier (SiPM) could be an alternative to PMTs for a LAr anti-Compton veto in GERDA. SiPMs do not require high voltage and they have a quantum efficiency that is at least equal to the one of PMTs. Their small mass and the materials they are made of suggest the assumption that their contribution to the radioactive background is low.
A major drawback of existing SiPMs is their small active area. In this work this disadvantage was overcome by connecting optical light guides to the SiPMs. The light guide increases the effective surface and guides the trapped photons to the SiPM. Such a design would have the advantage of being compatible with the design of GERDA.
The main goal of this work is to provide a scintillation light detection solution with SiPMs that is suited for low background experiments in general and is compatible with the stringent radio-purity requirements and the design of GERDA. In order to verify the principle a small scale experiment was built up to demonstrate a reasonably high light collection efficiency. The measurements performed with this setup proved that the concept is viable.

❖ ❖ ❖

This work is structured as follows:

Chapter 2 outlines the exceptional status of neutrinos in the standard model. It is stated why beyond standard model physics is required to explain the experimental results obtained from neutrino oscillations.

Chapter 3 reviews the different kinds of $\beta\beta$-decay. The current status of the $0\nu\beta\beta$-decay search is summarized. The GERDA experiment is introduced.

Chapter 4 describes the different interaction processes of radiation with matter in the energy range that is of interest for this work. Important properties of germanium detectors are described.

In Chapter 5 the working principle of SiPMs is explained. The non-linearity of their response is discussed.

In Chapter 6 the experimental equipment is summarized. In particular the used SiPMs are detailed. The chapter closes with a full characterization of the used SiPMs at cryogenic temperatures.

Chapter 7 explains the mechanism of scintillation light production in liquid argon. The estimated light yield of argon scintillation light is investigated.

Chapter 8 presents a SiPM based LAr-spectrometer that was built at the MPI für Physik, München. The individual components of the setup are characterized. Measurements and estimations on the light collection efficiency are given.

In Chapter 9 the operation of the LAr-spectrometer as an LAr anti-Compton veto for a HPGe detector is demonstrated. The suppression of the thorium background under different conditions is studied.

Chapter 2

Neutrinos

In the year 1930 Wolfgang Pauli postulated a neutral particle with small mass to explain the continuous spectrum of the β-decay and thus, to save energy and momentum conservation [2]. Later this particle was named neutrino. In the year 1956 C. Cowan and F. Reines were the first to experimentally detect neutrinos [3]. In the standard model of particle physics neutrinos are set to be massless. Only lately experiments have revealed that neutrinos oscillate and thus must be massive.

2.1 Neutrinos in the standard model

The leptonic sector of the Standard Model of particle physics (SM) consist of three families (see Table 2.1). Each family contains an SU(2) singlet and an SU(2) doublet. The singlets are the fields of the right handed charged leptons. The doublets each include the field of a left handed charged lepton and a left handed neutrino. All fields are eigenstates of the chirality (or handedness) operator $\gamma^5 = i\gamma^0\gamma^1\gamma^2\gamma^3$.
Only the left handed doublets are target to the weak force. Neutrinos are charge and colorless thus the weak interaction is the only SM force that couples to them.
A right handed neutrino singlet would not couple to any force and is thus not implemented in the SM. For anti-particles the same is true with left and right chirality being interchanged. Thus it can be concluded that all neutrinos in the SM have negative chirality (left handed) and all antineutrinos positive chirality (right handed).

Table 2.1: Leptonic sector of the standard model

chirality	family		
R	e_R^-	μ_R^-	τ_R^-
L	$\begin{pmatrix} \nu_e \\ e_L^- \end{pmatrix}$	$\begin{pmatrix} \nu_\mu \\ \mu_L^- \end{pmatrix}$	$\begin{pmatrix} \nu_\tau \\ \tau_L^- \end{pmatrix}$

The charged leptons in the SM are massive. The mechanism in the SM that gives mass to the charged leptons mixes their left and right handed chiral eigenstates. This is why the mass eigenstates have contributions of both fields.
Because no right handed neutrino is implemented in the SM there is no mechanism in the SM that could give mass to the neutrinos.
According to the SM all neutrino fields are massless eigenstates of the chirality operator and also propagate in these chirality eigenstates.
For a massless particle the chirality has the following properties:

1. It is conserved

2. The operator shares a common set of eigenvectors with the Dirac Hamiltonian

3. It has the same properties as the helicity [1], which gives it a physical meaning

The helicity of neutrinos has been measured in various experiments. To this day only neutrinos with negative helicity and antineutrinos with positive helicity have been observed.

2.2 Neutrinos beyond the standard model

The observation of neutrino oscillations however has revealed that neutrinos have mass [4]. Different mechanisms to explain neutrino masses exist. In all existing mechanisms the SM has to be extended. In the following some very prominent mechanisms are discussed for the one flavor case (no flavor oscillations).

Dirac masses: Introducing a right handed neutrino singlet would enable us to give mass to neutrinos the same way mass is given to the charged leptons in the SM. SM mass terms couple to left and right handed particles and are called Dirac mass terms. However right handed neutrinos have not been observed yet. One can argue that right handed neutrinos are too heavy to be observed in current experiments. But even introducing a heavy right handed neutrino requires an extension of the SM because simple Dirac mass terms give the same mass to left and right handed particles.

Majorana masses: A new mechanism that gives mass to particles without mixing their chirality eigenstates can be introduced. These masses are called Majorana masses. Because of charge conservation Majorana masses can only be given to charge-less particles. Even though no Majorana masses can be given to the left handed neutrino chirality eigenstates in the SM without breaking the SU(2) gauge symmetry.
It is evident that neutrino masses can not be explained with Dirac or neutrino-masses

[1]The helicity is the projection of the particle spin at the direction of motion. Its operator is $\vec{\Sigma} \cdot \hat{p}$. The helicity of a particle is only Lorentz invariant as long as its mass is zero.

exclusively. Therefore it is reasonable to make a general approach in which both, Majorana and Dirac masses, are given to the neutrinos. For this a right handed neutrino singlet field is introduced. Under the reasonable assumptions, that the Majorana mass of the left handed neutrino is zero (see above) and the Majorana mass of the right handed neutrino is very large (typically around GUT scale), one finds the following relations for the masses of the two resulting mass eigenstates m_1 and m_2

$$m_1 = \frac{(m_D)^2}{m_R} \tag{2.1}$$

$$m_2 \approx m_R \tag{2.2}$$

where m_R is the Majorana mass of the right handed neutrino, m_D is the Dirac mass, which couples left and right handed neutrinos. Latter is expected to be $\mathcal{O}$(weak scale).
This approach is called seesaw mechanism because a very large mass m_2 of a heavy neutrino implies a very small mass m_1 of a light neutrino.
The two mass eigenstates are superpositions of the chiral eigenstates. However one finds that in this model the small mass eigenstate is almost equivalent to the left handed chiral eigenstate and the large mass eigenstate is almost equivalent to the right handed chiral eigenstate. This explains why no oscillations from left chiral into right chiral eigenstates are observed.
Still for massive neutrinos the properties 1.-3. listed above are not valid. In particular from the violation of 1. follows that chirality is no good quantum number meaning that one can not distinguish neutrinos and antineutrinos according to their chirality. Taking this into account some theories predict that the neutrino is its own antiparticle. A particle that is its own antiparticle is called Majorana particle.

Chapter 3

Double beta decay

Double beta decay ($\beta\beta$) is a rare, second order, weak process in which a nucleus of charge Z and atomic number A decays into a daughter nucleus of charge Z + 2 and the same atomic number A. In principle all β-decaying isotopes can $\beta\beta$-decay as long as angular momentum conservation or a higher energy level of the daughter nucleus do not forbid it. However the competing single β-decay will dominate the observation. Therefore the $\beta\beta$-decay is only detectable when the single β-decay is forbidden. This is the case for ^{76}Ge which can not decay through the single β-decay because ^{76}As is heavier. However ^{76}Ge can decay directly into ^{76}Se through $\beta\beta$-decay.

3.1 $\beta\beta$-decay types

Two types of $\beta\beta$-decay are discussed, the neutrino accompanied double beta decay $2\nu\beta\beta$ and the neutrinoless double beta decay $0\nu\beta\beta$. During the $2\nu\beta\beta$-decay two protons in the nucleus decay simultaneously into two neutrons under the emission of two electrons and two electron antineutrinos. This process is rare but has been observed. For ^{76}Ge the half life was found to be of the order of 10^{20} years.

$0\nu\beta\beta$ could not be observed yet. $0\nu\beta\beta$ can only occur if the neutrino is a Majorana particle and a chirality flip is induced in the vertex for example by an effective Majorana mass $m_{0\nu\beta\beta} \neq 0$ (for details see [5]). In this case the Feynman diagram can be written with an inner fermion line instead of the two antineutrinos.

The Feynman diagrams of the two decays are shown in Fig. 3.1.

3.2 $\beta\beta$-decay detection

In order to detect $0\nu\beta\beta$ one measures the energy deposited in the detector during a $\beta\beta$-decay. The measured energy spectrum is continuous for the $2\nu\beta\beta$-decay because a certain fraction of the energy is carried away by the two antineutrinos which cannot be detected. In case of the $0\nu\beta\beta$ no neutrinos are produced and the whole emitted energy in the decay, the $Q_{\beta\beta}$, can be measured. In the spectrum a discrete peak is expected at

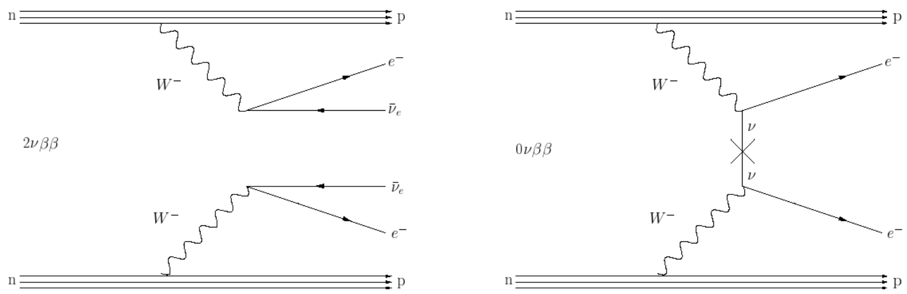

Figure 3.1: Feynman Graph of the $2\nu\beta\beta$ and the $0\nu\beta\beta$. They differ by the number of emitted antineutrinos.

$Q_{\beta\beta}$. The abstracted $\beta\beta$-decay signal is shown in Fig. 3.2.
Usually detectors can detect both types of events but cannot distinguish between them. Therefore one has to resolve the $0\nu\beta\beta$-peak from the $2\nu\beta\beta$-continuum.

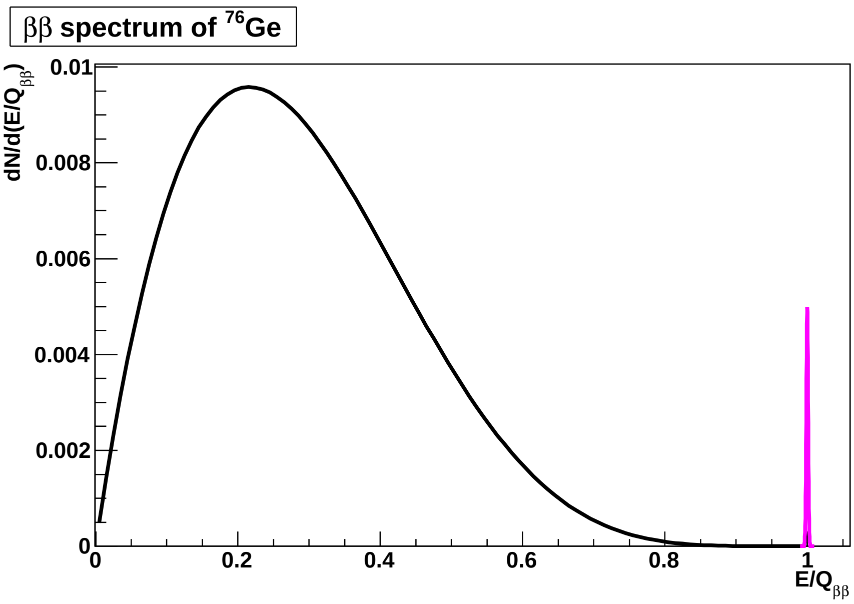

Figure 3.2: The expected energy deposition in the detector that is due to the $\beta\beta$-decay. The continuum (black) is due to the $2\nu\beta\beta$-decay. The peak is due to the $0\nu\beta\beta$. The scaling in the plot does not correspond to reality.

The decay rate of the $0\nu\beta\beta$ is given as

$$\Gamma_{0\nu\beta\beta} = \frac{1}{T_{\frac{1}{2}}^{0\nu\beta\beta}} = G_{0\nu}(Q,Z)\left|M_{0\nu}\right|^2 m_{0\nu\beta\beta}^2 \tag{3.1}$$

with $G_{0\nu}(Q,Z)$ being the phase space factor, $M_{0\nu}$ the nuclear matrix element of the $0\nu\beta\beta$ and $m_{0\nu\beta\beta}$ the effective neutrino Majorana mass.
If a significant number of $0\nu\beta\beta$ events can be detected one can deduce the effective Majorana mass $m_{0\nu\beta\beta}$ (for details see [5]).

3.2.1 Sensitivity and background of the $0\nu\beta\beta$

If the neutrino less double beta decay is observed, the number of measured events N_e will be given by

$$N_e = M \cdot \kappa \cdot \frac{N_A}{M_A} \cdot \varepsilon \cdot (1 - e^{\frac{-t}{\tau}}) \tag{3.2}$$

where M is the total target mass, κ is the fraction of the isotope under study, N_A is the Avogadro number, M_A is the atomic mass number of the isotope, ε is the detection efficiency, t the exposure time and τ is the life time of the $0\nu\beta\beta$.
As $\tau >> t$, the formula can approximated

$$N_e \approx M \cdot \kappa \cdot \frac{N_A}{M_A} \cdot \varepsilon \cdot \frac{t}{\tau} \tag{3.3}$$

The half life $T_{1/2}^{0\nu\beta\beta}$ can be written as

$$T_{1/2}^{0\nu\beta\beta} = \ln 2 \cdot \tau = \ln 2 \cdot M \cdot \kappa \cdot \frac{N_A}{M_A} \cdot \varepsilon \cdot \frac{t}{N_e} \tag{3.4}$$

The number of background N_b within the exposure time t and the energy window ΔE is Poisson distributed. The expectation value $<N_b>$ can be written as

$$< N_b >= b \cdot M \cdot t \cdot \Delta E \tag{3.5}$$

where b is the background index in units of events/(kg keV year). Given the target mass, background index, resolution and exposure of phase one GERDA one calculates $<N_b>=1$. If one inserts this value into the Poisson distribution one finds that $N_b < 3$ within 98% confidence level. Meaning that GERDA cannot resolve the signal with 98% confidence level if $N_e < 3$.

$$T_{1/2}^{0\nu\beta\beta} > \ln 2 \cdot M \cdot \kappa \cdot \frac{N_A}{M_A} \cdot \varepsilon \cdot \frac{t}{3} \tag{3.6}$$

If Eq. 3.1 is inserted into this relation an upper limit for the effective Majorana mass as a function of the experimental parameters can be estimated

$$m_{0\nu\beta\beta} = \sqrt{\frac{3M_A}{\ln 2 \cdot \kappa N_A \cdot \varepsilon \cdot G_{0\nu}(Q,Z) \cdot M \cdot t}} \frac{1}{M_{0\nu}} \tag{3.7}$$

With Eq. 3.7 the expected sensitivities of GERDA for different background scenarios can be calculated as a function of the exposure time. In Fig: 3.3 the expected lower limit on the Majorana mass/half-life of $0\nu\beta\beta$ is shown as a function of the the exposure time under different background conditions. For the calculations the matrix element from [7] was used.
As background one considers any energy deposition in the energy window in the peak of the $Q_{\beta\beta}$ ($\Delta E = 2039\,\text{keV}$) which is not due to the $0\nu\beta\beta$. It is evident from the figures that the achievable background level determines the useful exposure of the experiment.

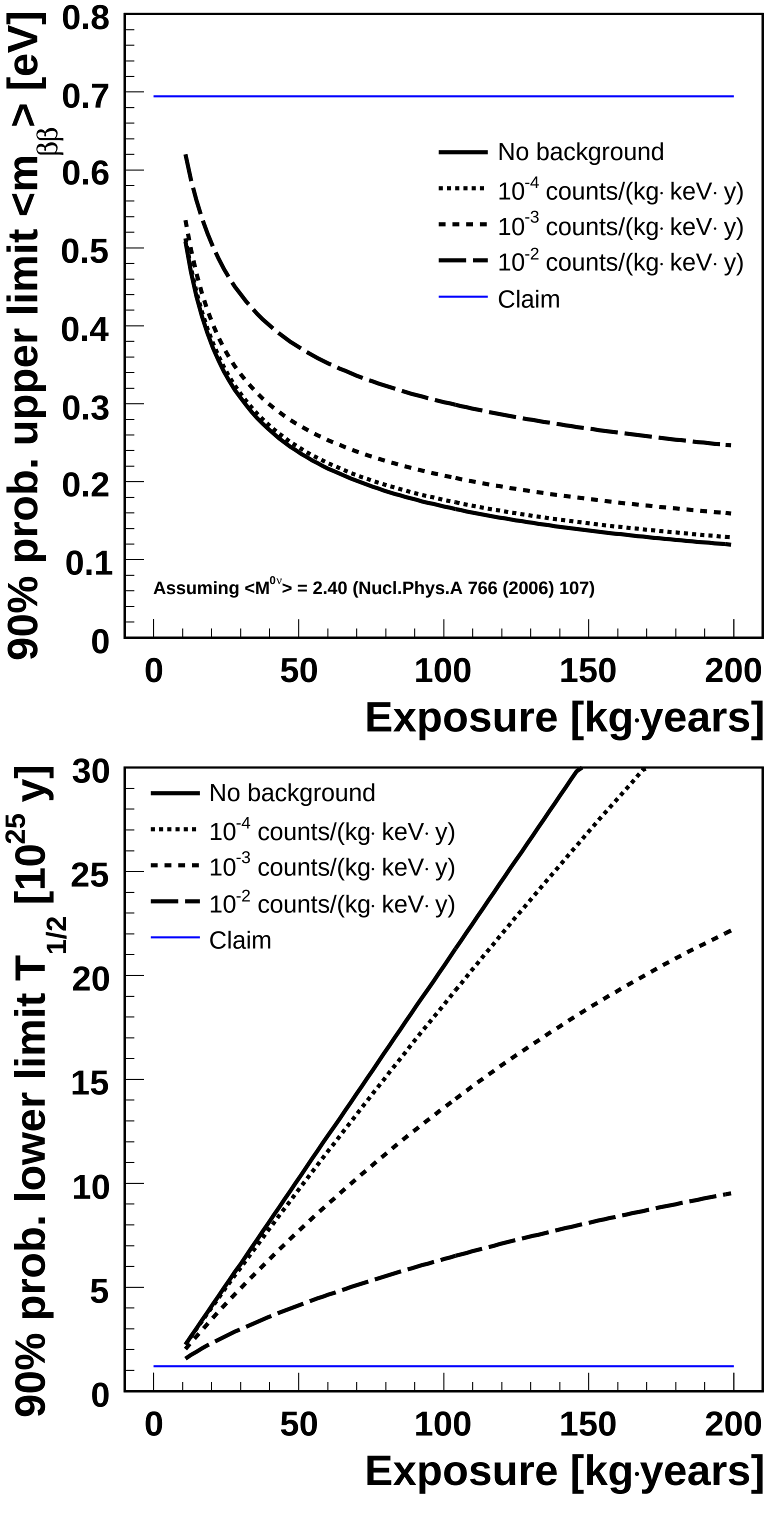

Figure 3.3: Figures were extracted from [6].

3.3 Experimental status of the $0\nu\beta\beta$ search

Today double beta experiments are the only feasible way to study whether neutrinos are Majorana particles or not. But the long half life of the $0\nu\beta\beta$ is a challenge to any design. In this chapter several former double beta experiments are briefly reviewed. The GERDA experiment is introduced.

3.3.1 Former experiments

So far no experiment has delivered undoubted evidence for $0\nu\beta\beta$ but a series of experiments has set stringent limits.
The Cuoricinio collaboration operates TeO_2 bolometer detectors with an active mass of 40.7kg at ~8mK for the $0\nu\beta\beta$ search. The detectors are made out of the target material. The isotope under study is ^{130}Te. ^{130}Te has certain advantages compared to ^{76}Ge. It has an abundance in natural tellurium of 34%. The $Q_{\beta\beta}$ of ^{130}Te is at 2528.8keV. The collaboration set an upper limit for the effective Majorana mass between 0.2 and 1.1eV with (90% CL) for the effective Majorana mass depending on the nuclear matrix element of ^{130}Te [8].
The IGEX and the Heidelberg-Moscow collaboration both used HPGe-detectors. In both experiments the detector was also the source of the decay. The isotope under study was ^{76}Ge. The natural abundance of ^{76}Ge is below 8%. Thus natural germanium had to be enriched. HPGe detectors have excellent energy resolution (below 2keV at 1332keV) and are produced with a high intrinsic purity level. Limits between 0.33eV and 1.35eV and between 0.32eV and 1.00eV, respectively were set [9] [10]. Parts of the Heidelberg-Moscow experiment claimed for an evidence of the $0\nu\beta\beta$ with $m_\nu = 0.2$ - 0.6eV (99% CL) [11]. One goal of GERDA is to confirm or disprove this claim. The claim is illustrated in Fig. 3.3.

3.3.2 The GERDA Experiment

The GERmanium Detector Array experiment (GERDA) is built for the search of the $0\nu\beta\beta$ of ^{76}Ge [12]. Its main design feature is the operation of bare HPGe detectors in ultra pure cryo-liquid (currently argon).
The experimental setup is structured as follows (see Fig. 3.4): Germanium diodes enriched in ^{76}Ge serve as target material and detector at the same time. They are hold via strings in a cryo-tank that is filled with liquid argon. The argon serves as coolant and shielding at the same time. Around the argon tank there is a second tank that is filled with water. The water serves as a second shielding and is in addition used as water Čerenkov-veto for cosmic muons. On top of the tanks a clean room is installed to guarantee clean environment when the germanium detectors are mounted into the cryo-tank. The experiment is situated in Hall A of the INFN Gran Sasso National Laboratory (LNGS) in Italy. The average overburden of rock is approximately 3400 meters of water equivalent and serves as a natural shielding against cosmic radiation.
GERDA is planned in two phases. Currently the first phase in which 17.66kg of enriched

germanium are used as target material is commissioned. Germanium diodes exist and are from the two previous experiments IGEX and Heidelberg-Moscow. The target background index is 10^{-2} events/(kg keV year) [13]. In phase two new Germanium detectors will be added. Using additional background reduction techniques the background index in phase two is aimed to be 10^{-3} events/(kg keV year). Beyond GERDA a third phase is discussed. It is desired to include a cooperation with the Majorana collaboration and aiming to be at the ton-scale.

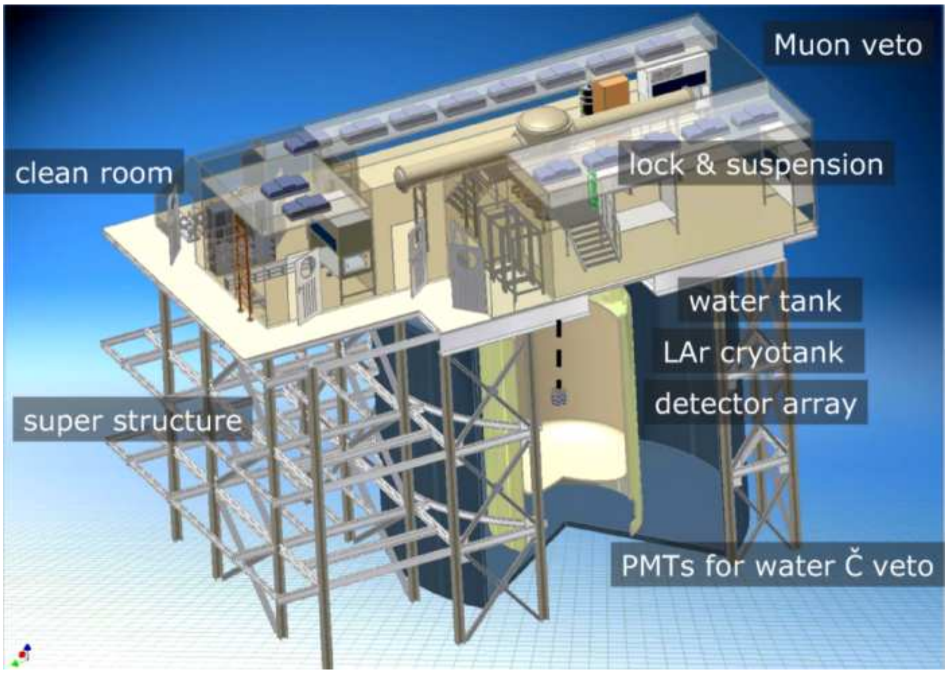

Figure 3.4: GERDA setup. The germanium diodes are operated in a liquid argon tank that is surrounded by a second water tank. Both serve as shielding.

Chapter 4

Interaction of radiation in matter and its detection with HPGe detectors

In this chapter the interaction of radiation in matter and its detection with HPGe detectors is reviewed.
First, the interactions of electrons, positrons and photons in the relevant energy region are discussed, the cross section and mean free paths of gammas are given. Further the general properties of germanium diodes and the signal development in them are are introduced. The chapter closes with the discussion of the radiation spectrum of ^{228}Th recorded with a HPGe detector. For a general overview of the properties of germanium detectors see e.g. [14].

4.1 Electrons and positrons

When electrons and positrons traverse through matter they loose energy through bremsstrahlung and the ionization end excitation of atoms. Ionization and excitation are the dominant processes at lower energies. At high energies bremsstrahlung dominates. The critical energy E_c above which bremsstrahlung becomes the dominant process can be estimated as follows [15]

$$E_c = 600/Z \text{ in MeV} \tag{4.1}$$

where Z is the atomic number of the of the material. For germanium and argon E_c are 19MeV and 33MeV, respectively. In our experiments no particles with energies above a few MeV were involved. Hence it can be assumed that all electrons and positrons in the measurements described in this work lose their energy mainly through ionization and excitation.
Being antimatter positrons furthermore annihilate with electrons into two 511keV photons after having lost their kinetic energy in collisions. The range of an electron in matter depends on its energy. The range of an 1MeV electron in germanium is approximately 1mm [16]. In argon the range of electrons with an energy up to 2MeV is below the cm level [17].

4.2 Photons

During their passage through matter gammas deposit their energy in point like interactions. They can undergo the following interaction processes: Photoelectric effect, Compton scattering and pair production. In all cases energy is passed to electrons or positrons which subsequently lose their energy as described above.
Photons emitted by the radiation sources used in the experiments described in this work (^{228}Th, ^{60}Co and their daughter isotopes) are in an energy range from a few keV to ~3MeV. Photons in this energy range can in principle undergo three kinds of interaction.

Photoelectric effect The photoelectric effect is the transfer of the entire energy of a photon E_γ to an electron either in an energy band or in an inner atomic shell. If the transferred energy exceeds the binding energy of the electron E_B, the electron leaves the crystal and becomes a free particle with the energy E_γ-E_B. Outer electrons fill the vacancy which the primary electron left behind leading to characteristic x-ray emission or secondary Auger electrons.

Compton scattering Compton scattering is the interaction between a free or loosely bound electron and a photon that results in the electron being given part of the energy, and a photon with the remaining energy being emitted in a different direction. If the photon still has enough energy left, the process might be repeated. The transferred energy E_{trans} is a function of the scattering angle ϕ and can be written as

$$E_{trans}(\phi) = E_\gamma \left(1 - \frac{1}{1 + \frac{E_\gamma}{m_e c^2}(1 - \cos(\phi))} \right) \tag{4.2}$$

where E_γ is the photon energy.
The energy transfer is maximal for backwards scattered photons.

$$E_{trans}^{max} = E_{trans}(\phi = \pi) = \frac{2E_\gamma^2}{m_e c^2 + 2E_\gamma} \tag{4.3}$$

E_{trans} can take any value between 0 and E_{trans}^{max}. The region between these two points is called Compton continuum. For a given gamma line a gap arises in the spectrum between E_{trans}^{max} and the peak at E_γ that is due to the full absorption. This gap is called Compton gap. Its width $E_{Compton}$ is

$$E_{Compton} = E_{trans}^{max} - E_\gamma \tag{4.4}$$

The falling edge of the Compton continuum is called Compton edge. A 1.33 MeV photon in Germanium Compton scatters on average three times before losing its entire energy through full absorption [13].

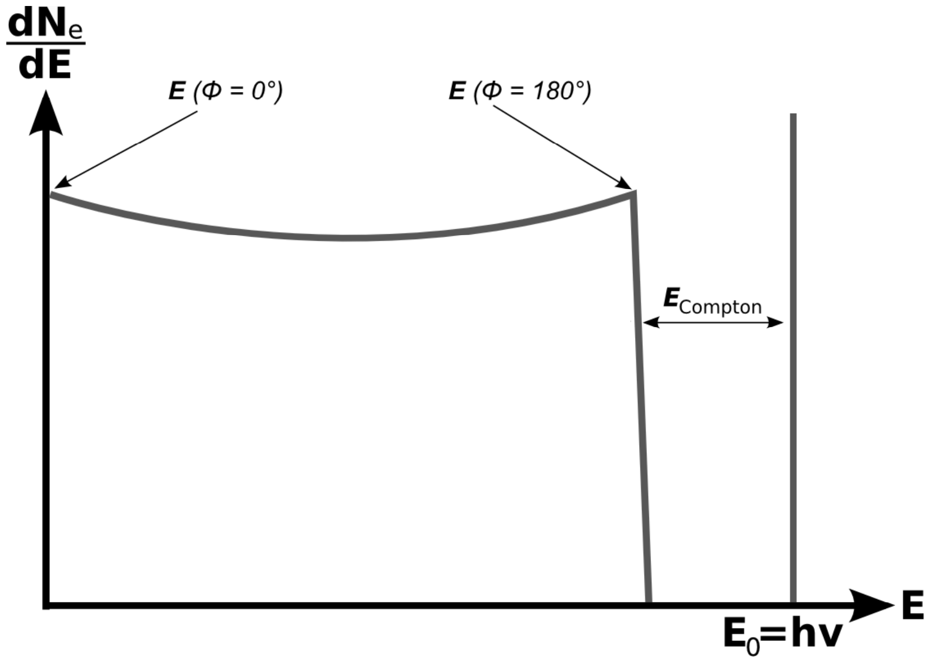

Figure 4.1: Hypothetical gamma spectrum of a mono-energetic gamma source. The continuum is due to the Compton scattering. The peak is due to the full absorption. Gammas that Compton scatter multiple times without depositing their entire energy in the detectors can lead to energy deposition in the Compton gap. These events are not included in this figure.

Pair production Pair production is the interaction of a photon with an electric field (typically the nucleus' field) in which an electron and a positron are produced. The energy threshold for this process is twice the electron mass (511keV). The fraction of the photon energy that exceeds this threshold is transferred to the kinetic energy of the leptons. Pair production becomes the dominant process for gamma with energies above few MeV.
Fig. 4.2 shows the cross section for the interaction of a gamma with a germanium and an argon atom, respectively as a function of the gamma's energy. In addition the distinct cross sections for the three discussed processes are shown. In both materials the photo-electric effect is the dominant process in the low keV region. For energies between 100keV and 8MeV-10MeV Compton scattering dominates. Above pair production is the dominant process. With total cross section σ and the particle density n, the mean free path λ in a medium can be calculated

$$\lambda = \frac{1}{\sigma \cdot \mathrm{n}} \tag{4.5}$$

In the Fig. 4.3 the calculated mean free path of gammas in germanium and LAr given as a function of the energy of the gamma.
The mean free path of of a 500keV gamma in germanium is about 2cm. In argon it is almost 9cm. This quantity is a stringent limit for any LAr based anti Compton veto.

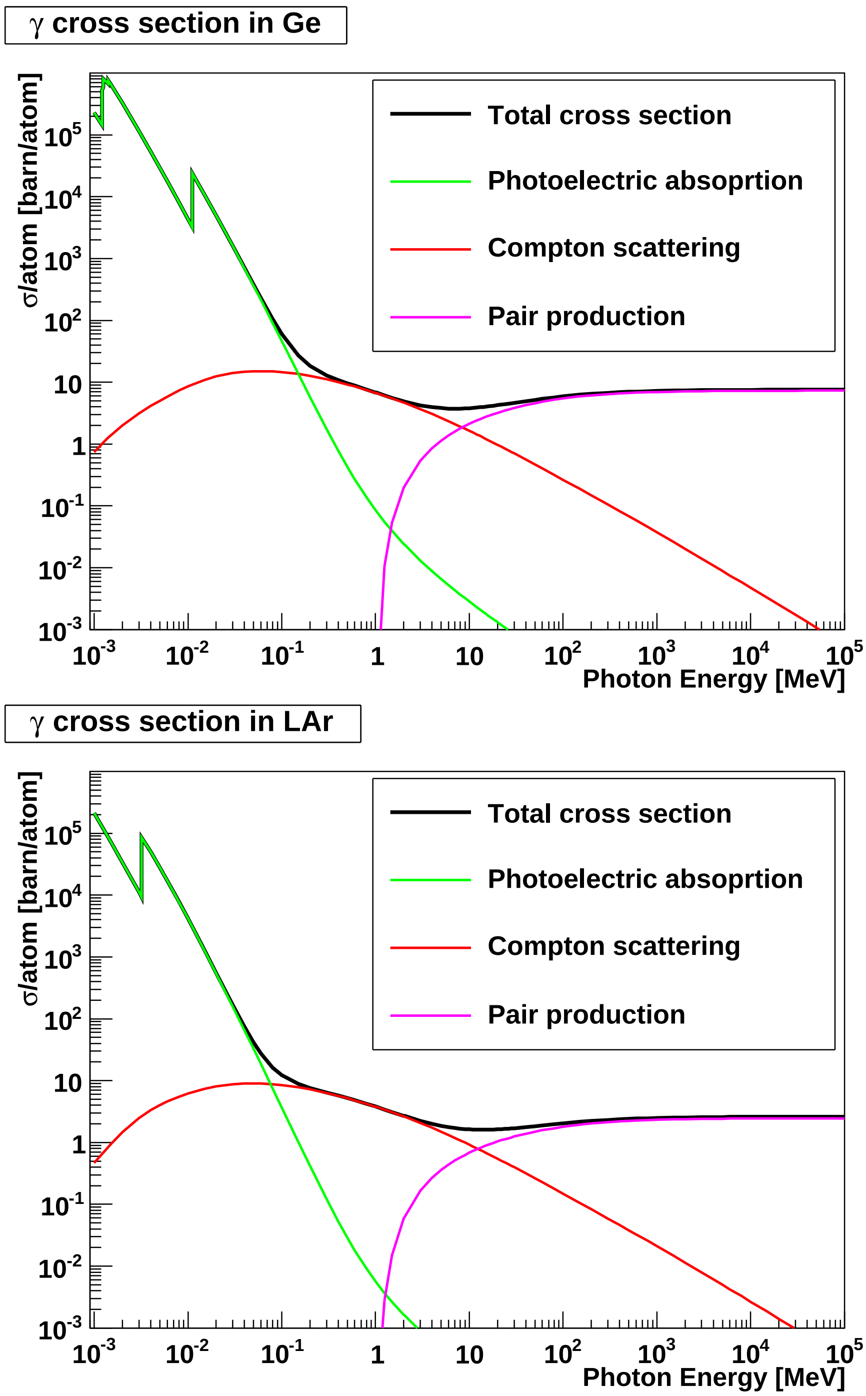

Figure 4.2: Total interaction cross section per atom for a photon in Ge and LAr. In addition the cross sections for the three distinct processes discussed above are given. The sharp peaks in the low keV region come from discrete energy levels of the inner atomic shells. Data from [18].

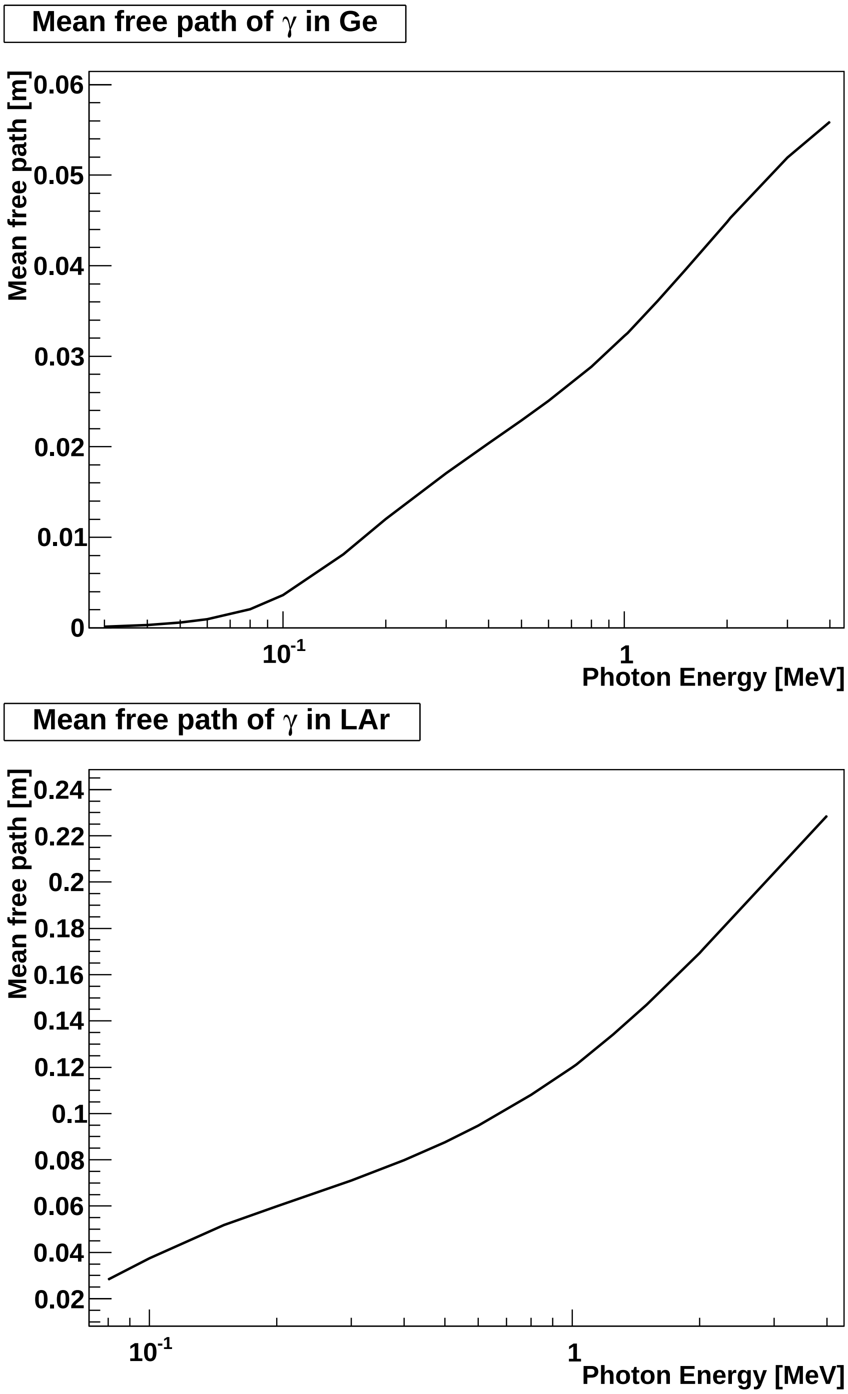

Figure 4.3: Mean free path of gammas as a function of the energy in germanium and LAr.

4.3 Detection of radiation with HPGe detectors

When energy is deposited a germanium detector electron-hole pairs are generated. The average energy deposit needed to generate one electron hole pair is called, pair energy. For electrons, positrons and gammas in germanium it is 2.96eV [14]. The number of generated electron-hole pairs can be interpreted in terms of the energy deposition in the detector. In germanium 1MeV energy deposition equals the generation of ∼340000 electron-hole pairs.

A second quantity of interest is the variance in the number of generated charge carriers. It is typically expressed in form of the Fano factor F which is a function of the deposited energy:

$$F(E_{\mathrm{deposit}}) = \frac{\text{observed statistical variance}}{E_{\mathrm{deposit}}/\text{ pair energy}} \tag{4.6}$$

A close connection of this parameter and the resolution can be found (for details see [14]). Germanium detectors typically have small Fano factors (below 0.15) resulting in an excellent resolution (down to 1.7keV FWHM at 1.33MeV).

4.4 ^{228}Th Calibration spectrum

Aim of this section is to present and explain typical features of a gamma spectrum recorded with a HPGe detector. This is done for the example of ^{228}Th spectrum, which is of particular interest in this work.

In Fig. 4.4 the gamma spectrum of ^{228}Th and its daughter isotopes is shown. Most peaks in this spectrum are full absorption peaks (FAP). Full absorption means that a gamma deposits its entire energy in the germanium detector. At 2614keV there is a FAP. The corresponding gammas origin from the decay of ^{208}Tl. ^{208}Tl is a daughter of ^{228}Th. In the ^{228}Th decay chain ^{208}Tl emits 2614keV gammas with a probability of ∼100%. At this energy Compton scattering is the dominant process. It is likely that such a gamma Compton scatters several times in the detector before depositing its remaining energy through the photoelectric effect. The mean free path of a 2614keV gamma in germanium is ∼5cm. Thus the energy deposition will in general be widespread.

Below the 2614keV gamma line the corresponding Compton gap and the Compton continuum can be found. The Compton edge is around 2400keV. The continuum originates from gammas that Compton scattered in the germanium without depositing their entire energy in the detector.

Peaks at lower energies lie on top of this Compton background.

Incoming 2614keV gammas can also perform pair production in the detector. In this case the electron and the positron deposit their summed kinetic energy, which is 2614keV minus twice the electron mass, in the detector. Subsequently the positron annihilates with an electron under the emission of two 511keV gammas. If one of these gammas is fully absorbed while the other escapes, the total energy deposition is 2103keV. In the spectrum these events can be found under the single escape peak (SEP). If both gammas escape

in total 1592keV are deposited. The corresponding peak is called double escape peak (DEP). As only the electron and the positron deposit energy in the detector, the deposition happens within a radius of a few mm. This radius is small compared to the energy deposition radius of events under FAPs.
The peak at 1620keV is a FAP and comes from the γ-decay of ^{212}Bi, a daughter isotope of ^{228}Th. It is typically of the same intensity as the DEP.
The peak at 1460keV is also a FAP and comes from the gamma decay of ^{40}K. ^{40}K is a radioactive isotope which is not in the decay chain of ^{228}Th but very abundant in the environment. The decay of ^{40}K typically does not come in a cascade with other decays. This is why these events will be of particular interest for our analysis.
The region of interest (ROI) for the $0\nu\beta\beta$ of ^{76}Ge is around the $Q_{\beta\beta}$ which is at 2039keV. The background from ^{228}Th and its daughter elements in this region is flat and is mainly due to singly Compton scattered gammas.

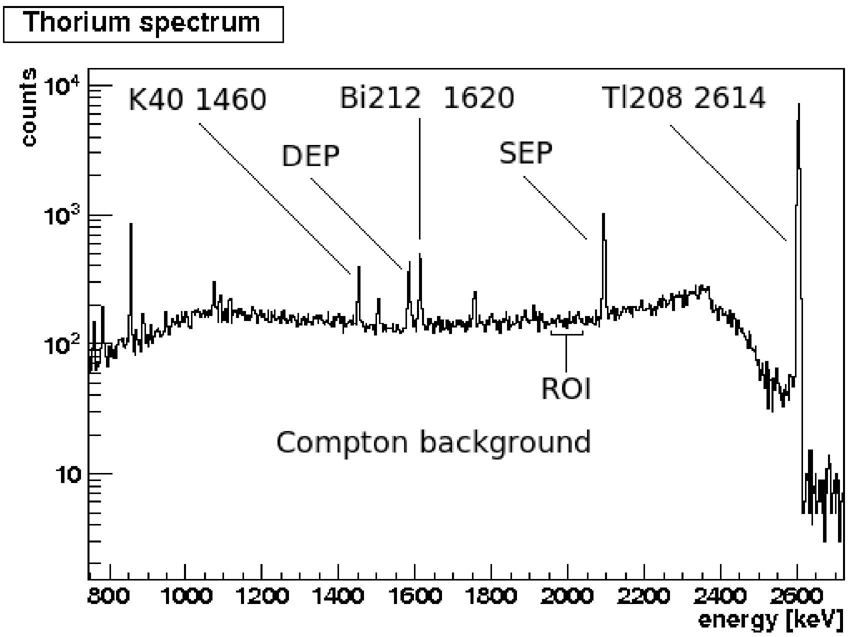

Figure 4.4: Gamma spectrum of a ^{228}Th source.

Chapter 5

Silicon photomultipliers (SiPM)

In this work a LAr scintillation light detection solution is provided that is based on SiPMs. Silicon Photomultipliers are photon detection devices that are based on the avalanche effect in photodiodes. SiPMs used for this work are sensitive on light from a wavelength of ∼270nm to ∼900nm (peak sensitivity: 400nm). They achieve a gain of 10^6 which is comparable to the gain of photo multiplier tubes. They are operated at voltages below 100V with photon detection efficiencies above 30% [19]. In this chapter the working principle of SiPMs is explained.
In the applications studied in this thesis the SiPMs need to be operated in a cryo-liquid. Thus, their characterization at cryogenic temperatures will be presented.

5.1 Working principle

A SiPM is an array of Avalanche Photodiodes (APD) (see Fig. 5.2) where the APDs are operated at voltages where they are in an instable equilibrium. In this state a single free charge carrier in the high field region will cause a charge carrier avalanche in the APD. Incident photons can induce electron hole pairs which drift in the APD to the high field region where they generate secondary charge carriers (Fig. 5.1). Because of the high charge acceleration in the high field region the generation of secondary electron hole pairs does not come to an end; the avalanche is self-sustaining. The discharge has to be extinguished separately. This is done by reducing the voltage and thus the electric field in the high field region. This process is called quenching. If the discharge of the APD would not be quenched a constant current would flow through the device. This would correspond to an infinite gain factor. However even for a quenched APD any information about the original number of incident photons and their energy is lost. An APD in this mode is thus a binary device, giving a uniform pulse for all events depending only on the quenching mechanism. This mode of operating APDs is called Geiger mode.
Only the fact that SiPMs consist of an array of APDs, makes them capable to detect multiple photons. When the number of incident photons is much smaller than the number of APD cells the SiPM can be used to count single photons. For this thesis SiPMs with 100, 400 and 1600 APD cells were studied. The APD cells will be referred to as pixels.

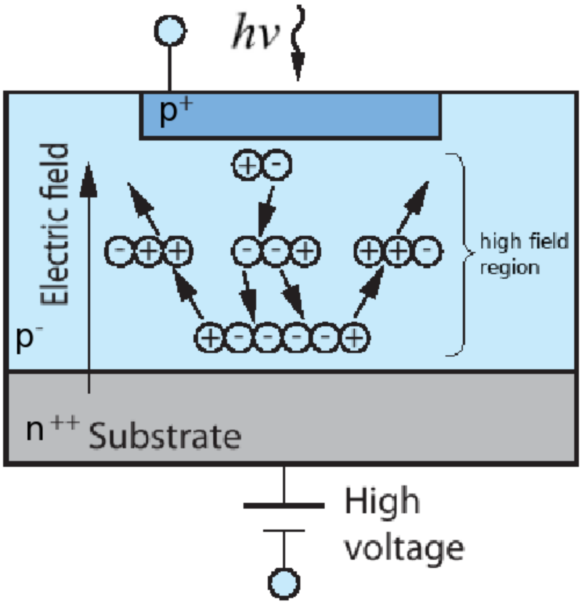

Figure 5.1: Scheme of an APD cell. An incoming photon excites an electron hole pair in the p^+doped region. The electron drifts to the high field region between the p^- and the n^{++} layer. Here the high electric field accelerates the charge carriers such that secondary electron hole pairs are created. Picture taken from [20]

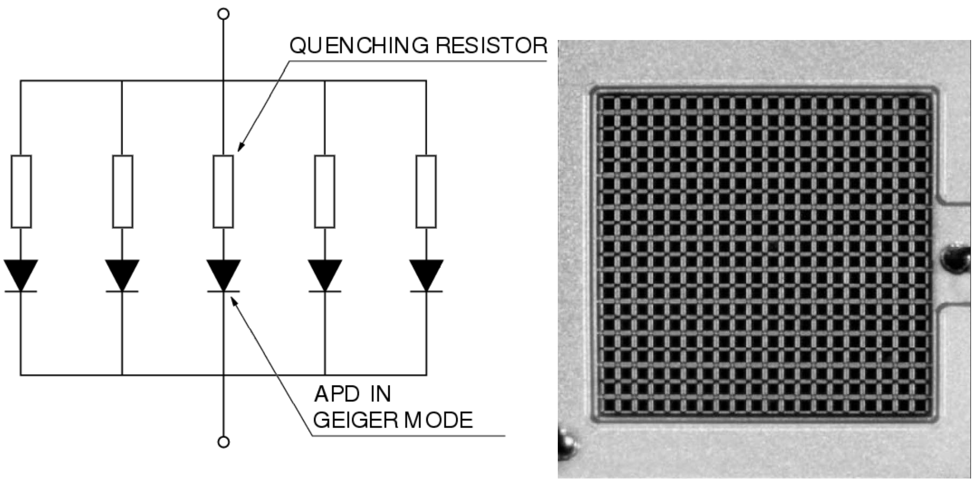

Figure 5.2: **Right:** A SiPM is an Array of APDs. To each APD a quenching resistor is connected in series. The quenching resistor extinguishes the avalanche discharge. **Left:** Hamamatsu MPPC(SiPM) chip with 400 APD cells. Each cell is an APD. The quenching resistors can not be seen from outside.

In the following some of the most crucial parameters of a SiPM are listed and explained.

Gain: The gain refers to the charge amplification of a SiPM. It is defined by the amount of charge that is produced by one pixel of the SiPM when hit by a photon divided by the elementary charge [20].

$$\text{gain} = \frac{\text{Charge of the one p.e. pulse}}{\text{elementary charge}} \tag{5.1}$$

For SiPMs the gain is typically of the order of 10^5 - 10^6 at reasonable operation voltages. At varying temperatures the gain remains stable as long as an adequate bias voltage is applied.

Breakdown voltage: The breakdown voltage $V_{\text{breakdown}}$ is the minimum voltage that is required to operate an APD in Geiger mode. It is often reported that by definition the gain of a SiPM is zero when operated at this voltage $V_{\text{breakdown}}$ [20]. However this is only a conventional definition. A $V_{\text{breakdown}}$ defined this way is typically derived from the extrapolation of the fit of the gain as a function of the bias voltage to the point of gain = 0. In practice the APD is no longer in Geiger mode when operated at such low voltages. Even in linear mode the smallest achievable gain of an APD is one. Nevertheless the conventional definition will be used in this work.
The breakdown voltage declines with decreasing temperature (see Sec. 6.2.4). This is because the mobility of the charge carriers is higher at lower temperatures [21]. Thus, a weaker electric field is required to give them the energy necessary to trigger an avalanche. The difference between the bias voltage and the breakdown voltage is called over voltage. $V_{\text{over}} = V_{\text{Bias}}$-$V_{\text{breakdown}}$. Most SiPMs parameters are functions of V_{over}.

Afterpulses: During the avalanche discharge some charge carriers get trapped within the high field region. This is usually due to impurities or crystallographic defects. These trapped charge carriers are typically released a few ns later and trigger a secondary avalanche in the same APD. This results in a secondary pulse which is called afterpulse. If the afterpulse occurs before the APD fully recovers it has a smaller amplitude than a regular pulse [21].
If V_{over} is reduced fewer charge carriers are produced during a discharge. The smaller number of charge carriers then reduces the charge trapping and thus the probability for afterpulses.

Cross-talk: The phenomenon when a triggered pixel fires simultaneously with a second one that was not hit is called cross-talk.
During the avalanche discharge it might happen that an electron and a hole recombine creating a infra red photon that triggers a neighboring pixel [20]. In such a case the number of fired pixels is higher than the number of p.e. created. The cross-talk probability is a function of V_{over}. Cross-talk events cannot be distinguished from multi photon events.

Dark count: Even in complete darkness pixels will fire occasionally. This is due to the thermal generation of charge carriers in the APD [20]. These charge carriers result in pulses that cannot be distinguished from photon induced pulses. The thermally generated pulses, their related afterpulses and cross-talk pulses are considered as the dark count. Thermally generated dark pulses are typically single pixel events. As the cross-talk mechanism is the same for photon induced and dark pulses the dark rate can be used to measure the cross-talk probability.

Photon Detection efficiency (PDE): The PDE is the ratio between the number of detected photons and the number of incident photons [20]. The PDE is the product of the quantum efficiency of a single APD cell and the fill factor. The fill factor is the ratio of the active surface of the APDs and the total surface of the SiPM. The fill factor is constant for a certain SiPM but the quantum efficiency increases with V_{over}.

Quenching resistor: After an APD in Geiger mode triggered it is necessary to reset it before it can re-trigger. This reset is called "quenching". So called passive quenching is based on a quenching resistor. This resistor is connected in series to each APD in a SiPM. If a pixel fires the Geiger discharge in the APD results in a current flow through the resistor and the APD. Thus, the voltage in the high field region drops below the voltage necessary to operate the APD in Geiger mode. The avalanche is extinguished.
The quenching resistor and capacity of the APD cell determine the wave form of the APD. The triggering of an APD can be regarded as the discharge of a capacitor. The capacity of the capacitor C and the resistance of the quenching resistor R form an RC-circuit. The decay time τ of an APD pulse is given as:

$$\tau = \mathrm{R} \cdot \mathrm{C} \tag{5.2}$$

Thus, an increase of R results in a longer decay time of the pulse. The used SiPMs are all passively quenched. As their quenching resistor have temperature dependent resistances the APDs have longer decay times and smaller amplitudes at low temperatures.

5.2 SiPM spectra

A big advantage of SiPMs is the single photon resolution. The amplitude spectrum of a SiPM typically consists of sharp peaks, the photo electron peaks (p.e.). Each peak corresponds to a certain number of pixels that triggered. If the light intensity is low enough one can say that single photons were detected. With the SiPMs used for this work single photon resolution for all temperatures between LN temperature 77.36K and room temperature $\sim$ 300K (RT) was observed.
The resolution is better for higher temperatures. This can be explained by the decrease of the signal amplitude at low temperatures [22]. In this case the SiPM response is more affected by the electronic noise.

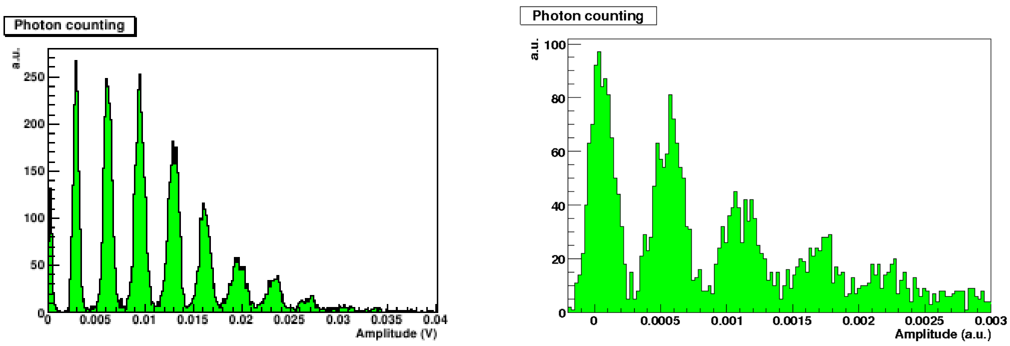

Figure 5.3: Left: SiPM amplitude spectrum at RT. The sharp peaks are p.e. peaks and correspond to a certain number of pixels firing. **Right:** SiPM amplitude spectrum in LN. The resolution is worse than at RT. This is because the amplitude of the SiPMs decreases with decreasing temperatures [22]. Thus it is affected more by the electronic noise at low temperatures.

5.3 Dynamic range and correction curves

At high light intensities it can occur that multiple photons hit the same pixel at the same time. Thus it is evident that the response of a SiPM is not linear at higher light intensities. The response of a SiPM to an arbitrary number of photons was calculated and can be found in appendix A. The expectation value of the number of firing pixels <k> as a function of the number of incident photons n can be written as:

$$< k(n) >= N_{pix} \cdot \left(1 - \exp\left(-\frac{n \cdot PDE}{N_{pix}}\right)\right) \tag{5.3}$$

where N_{pix} is the number of pixels and the PDE is the photon detection efficiency of the SiPM. In Fig. 5.4 the calculated and a linear response function are plotted for a SiPM with 100, 400 and 1600 pixels. The effect of afterpulses and cross talk were neglected and a PDE of 1 was inserted. As long as the number of incident photons is small the two plots match very well. For the SiPM with 100 pixels the linear range ends at ~20 pixels, for the one with 400 pixels at ~100 pixels and for the SiPM with 1600 pixels at ~300 pixels.

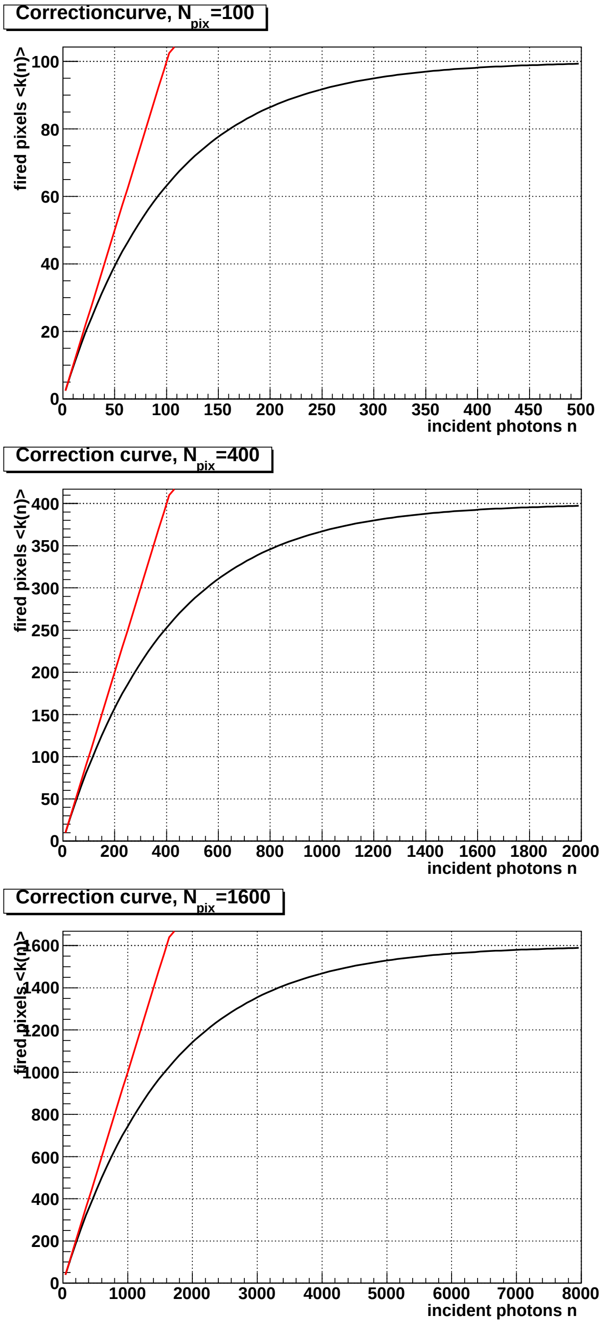

Figure 5.4: Calculated and linear response function of a SiPM with 100, 400 and 1600 pixels to a light pulse with a given number of photons

However in experiments one typically knows the number of fired pixels k and wants to deduce the number of incident photons n. The number of incident photons for a given number firing pixels is given by a probability distribution P(n|k). Using Bayes' Theorem this distribution can be extracted from P(k|n), the probability distribution for the number of pixels firing k given the number of incident photons n:

$$P(n|k) = \frac{P(k|n) \cdot P_0(n)}{\sum_{n=0}^{N} P(k|n) \cdot P_0(n)} \tag{5.4}$$

In a simplified model it can be assumed that the apriori probability $P_0(n)$ is constant for any n≥k and otherwise 0. This means that we know that the number of incident photons is always bigger than the number of fired pixels. But except for this restriction any number of incident photons has a priori the same probability. Eq. 5.4 can now be simplified to

$$P(n|k) = \frac{P(k|n)}{\sum_{n\geq k}^{N} P(k|n)} = C \cdot P(k|n) \tag{5.5}$$

where C is a constant. This means that the two probability density functions are proportional and can easily be derived from each other.
P(k|n) can be expressed with a recursion formula:

$$P(k|n) = P(k|n\text{-}1) \cdot \frac{k}{N_{\text{pix}}} + P(k\text{-}1|n\text{-}1) \cdot \left(1 - \frac{n-1}{N_{\text{pix}}}\right) \tag{5.6}$$

The first term in Eq. 5.6 considers that possibility that the first out of n photons does not trigger a pixels. In this case the n-1 photons left must trigger k pixels. This value must be weighted with $\frac{k}{N_{\text{pix}}}$, which is the probability for the first photon not to trigger a pixel. The second term considers the possibility that the first photon does trigger a pixel. Thus the n-1 photons left must trigger k-1 pixels. This value is weighted with $1 - \frac{n-1}{N_{\text{pix}}}$, which is the probability for the first photon to trigger a pixel. This recursion allows to code a simple program that delivers P(k|n). As initial values P(0|k≠0)=0 and P(0|0)=1 can be inserted.
In Fig. 5.5 the probability density function P(k|n) is shown for SiPMs with 100, 400 and 1600 pixels. It is worth noting that in the linear range P(k|n) is very sharp. For higher k P(k|n) is spread over a large range of n. This means that the number of incident photons can not be derived from the number of pixels hit. This is a purely statistical effect and will bias the energy resolution of a SiPM regardless of the electronics. The effect is bigger for SiPMs with a small number of pixels.

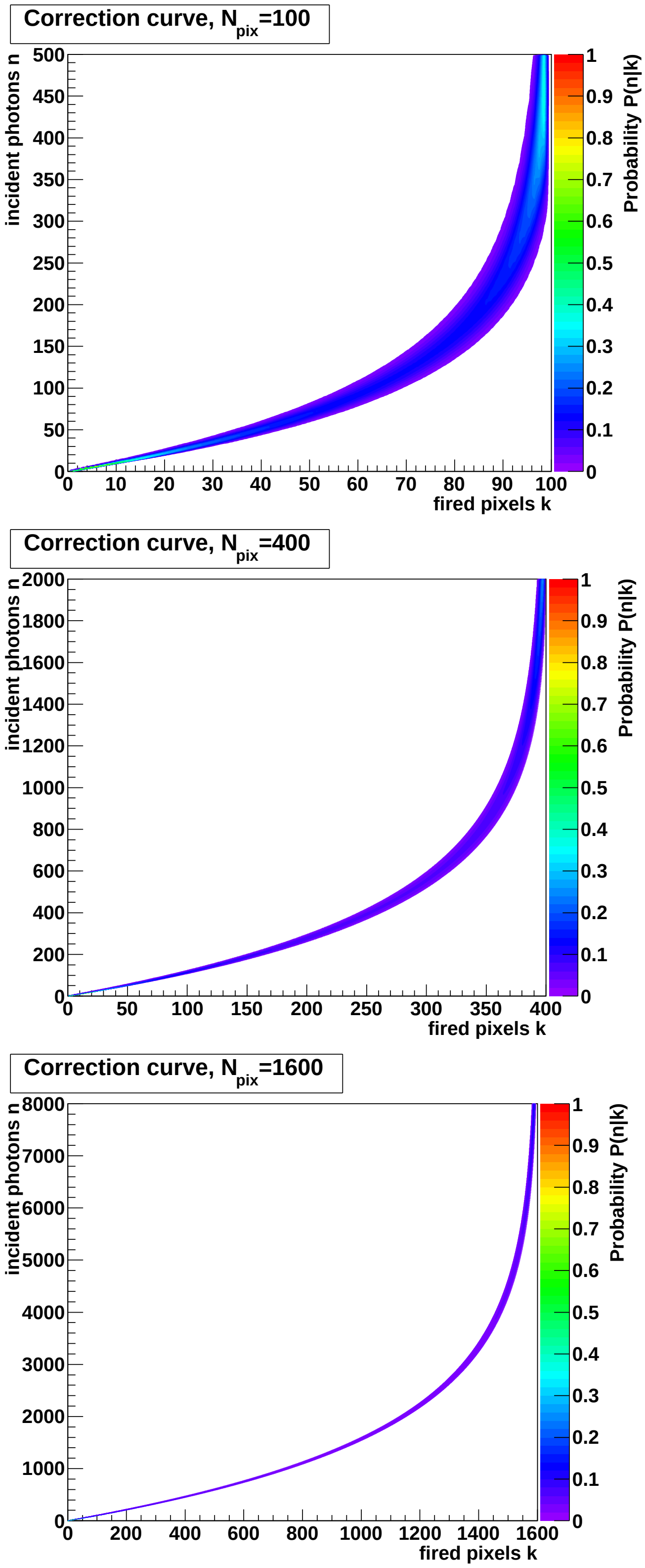

Figure 5.5: Probability distribution P(k|n) for SiPM with 100, 400 and 1600 pixels.

Chapter 6

Experimental equipment

In this chapter the experimental equipment used for the final experiment is described. The chapter is divided into two parts. In a first part the characteristics of all used devices, in particular of the used SiPMs, are summarized. In a second part the characterization of the used SiPMs at cryogenic temperatures is presented.

6.1 List of used equipment

Oscilloscope Lecroy waveRunner 104 MXi Oscilloscope with a analog bandwith of 1GHz and four channels [23].

DAQ 75 MHz XIA Pixie-4 DAQ with up to five four-channels modules. For each event, energy, time and pulse shape informations can be stored [24].

Charge sensitive preamplifier CR-112 charge sensitive preamplifier. The electronic schematics and a picture of the preamplifier are shown in Fig. 6.1.
The charge sensitive preamplifier integrates the input signal. The amplitude of the response is proportional to the integrated charge. The charge sensitive preamplifier is an analog device. The smallest detectable charge will be limited by the noise. The largest detectable charge is $2.1 \cdot 10^{-10}$C.
Specifications: gain: 15 mV/pC, rise time: 6ns, decay constant: 50μs [25].

Linear preamplifier Preamplifier board made by the electronics workshop of the MPI (see Fig. 6.2). The amplifier is an analog device. Downwards the detectable range will be limited by the noise. The amplification saturates at 5V.
Specifications: gain: 10, rise time: 1-2 ns

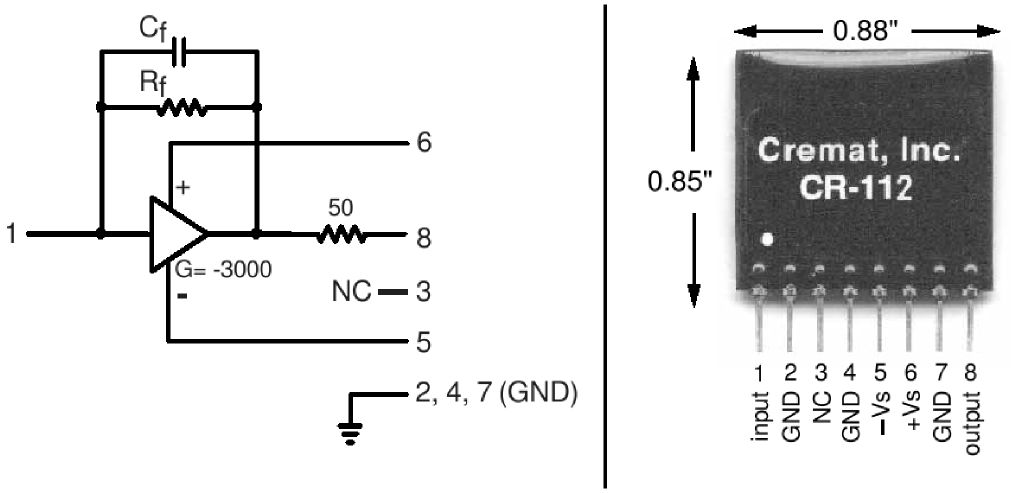

Figure 6.1: **Left:** Schematic ciruit of the Cr-112. The Cr-112 is a operational amplifier that integrates the input pulse. The amplitude of the response is proportional to the integrated charge. **Right:** Picture of the CR-112. Pictures taken from [25].

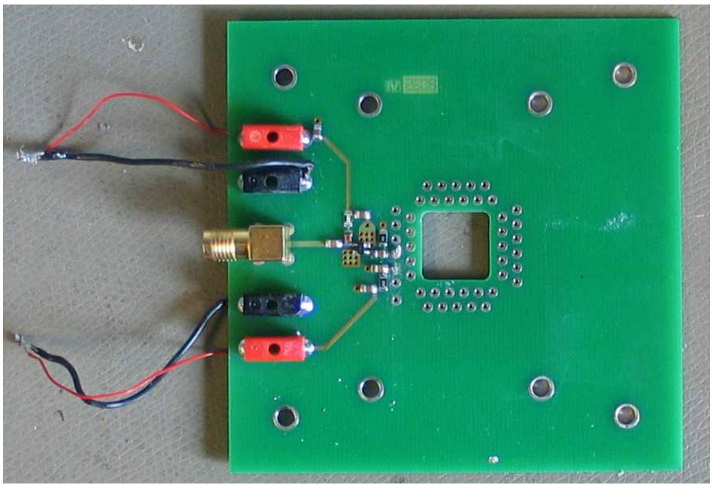

Figure 6.2: Testboard with a linear preamplifer in the center. Testboard made by the workshop of the MPI for Physics in Munich.

Amplifying shaper EG&G Ortec amplifying shaper, Model 572. Delivers standard pulse for every input pulse.
Input: positive or negative pulses, rise time: 10ns to 650ns, amplitude: 5mV to 20V, decay time : 40μ s - ∞
Output: Standard Semi-Gaussian pulse on all ranges, shaping time: 0.5-10μs, gain:1-1500, maximum output: 20V

Discriminator LeCroy Octal Discriminator, Model 623B. [23]
Delivers standard rectangular pulse for every input pulse above a certain threshold.
Input: amplitude 30mV to 1V, maximum rate: 0MHz - $\sim$100MHz
Output: amplitude: 800mV, rise time: 2.1ns, width:10ns

Counting module Jorway Corporation counting module, Model 1883. Counts the number of input pulses [26].
Input: rate: 0MHz to 100MHz, pulse pair resolution: 40ns, minimum pulse width: 3ns, adjustable threshold: 300mV to 500mV

Dewar KGW Isotherm cylindrical dewar, Model: 34C/Cal [27]. Diameter: 240mm, height 480mm, volume 21l

The Multi Pixel Photon Counter (MPPC): All SiPMs that were used for this work were made by Hamamatsu [28]. They are sold under the name Multi Pixel Photon Counter (MPPC). Their series numbers are S10362-11- 100C/050C/025C. In the following they will be only referred to as SiPM. The SiPMs were delivered in three versions different in their number of pixels. SiPMs with 100 (S10362-11-100C), 400 (S10362-11-050C) and 1600 (S10362-11-025C) pixels were delivered. All three SiPM types were mounted in the same ceramic holder which had a size of 5mm $\times$ 6mm. The active surface was 1.0mm $\times$ 1.0mm for all three SiPM types (See Fig. 6.3).
The pixel size of the SiPM types differed and lead to differences in the their characteristics as e.g. gain, dark rate and photon detection efficiency. All characterization measurements were performed for all three of types of SiPMs.
The specifications given by Hamamatsu [20] are listed in Table 6.1.

Table 6.1: Specifications of the Hamamatsu S10362-11 series [20]

Number of pixels	100	400	1600
Pixel size	$100\mu m \times 100\mu m$	$50\mu m \times 50\mu m$	$25\mu m \times 25\mu m$
Fill factor	78.5%	61.5%	30.8%
PDE at peak (400nm)	65%	50%	25%
Dark count at RT	600-1000 kHz	400-800 kHz	300 - 600 kHz
Gain at RT	2.75×10^{6}	7.5×10^{5}	2.4×10^{5}
Spectral response range	270nm to 900nm		
peak sensitivity	400nm		

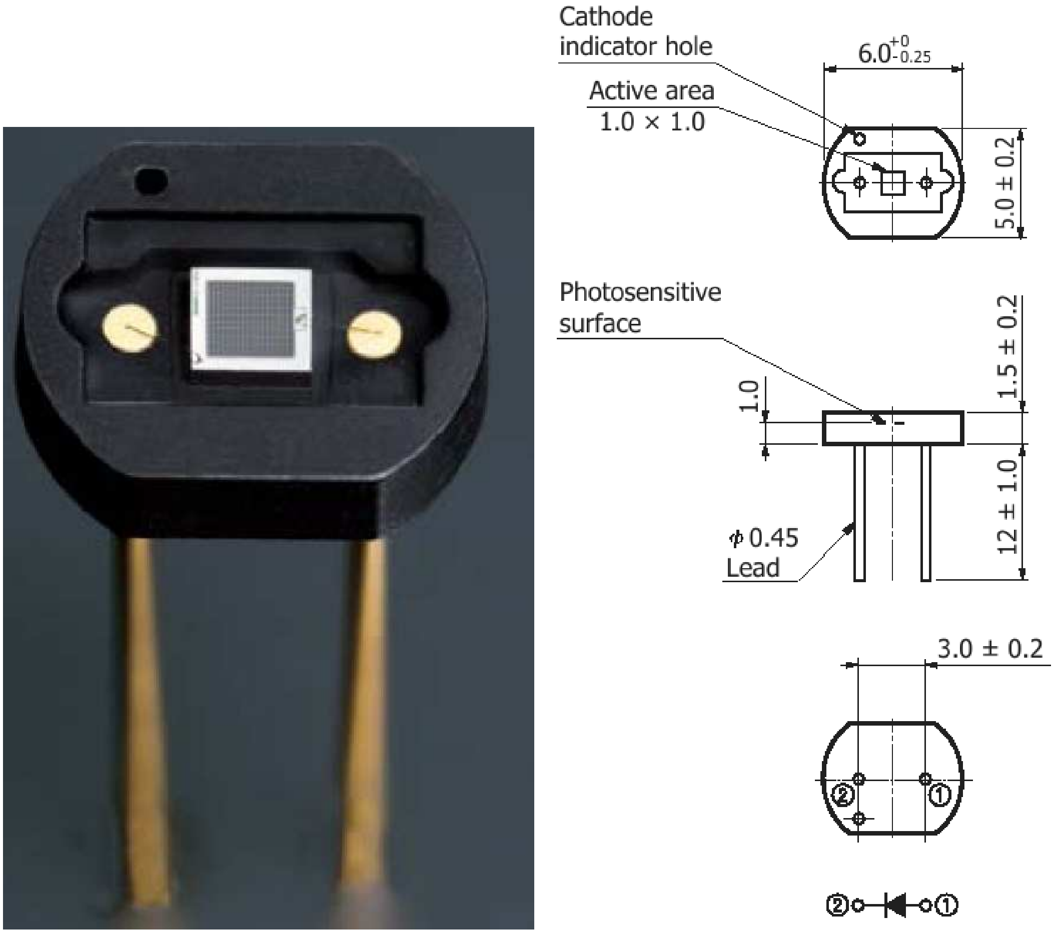

Figure 6.3: **Left:** Picture of a SiPM with 400 pixel-chip. The chip is mounted in a ceramic holder and protected by a layer of epoxy. Two connectors are istalled below the epoxy layer. The other two SiPM chip-types were mounted in the same way. **Right:** Dimensions of the SiPMs used in this work. All vales are given in mmm. Both pictures were taken from [20].

6.2 Characterization of the SiPMs at cryogenic temperatures

In this work a LAr scintillation detection solution is provided that operates SiPMs directly in LAr. The boiling temperatures of argon (87.3K) is very close to the boiling temperature of and nitrogen (77.4K). Thus, it can be assumed that the SiPMs perform similarly in the two liquids.
In this section measurements that were performed to characterize the SiPMs at cryogenic temperatures are presented. The aim of these measurements was to prove the suitability of the SiPMs for light detection at cryogenic temperatures. The gain and the dark rate as a function of the temperature were measured directly. With the data collected during these measurements the breakdown voltage and the cross talk probability as a function of the temperature were calculated. In addition the waveforms at LN temperature were studied.
All measurements were done for all three types of SiPMs. The studied properties are similar for all three types (100, 400 and 1600 pixel).
It was decided to use the SiPM with 400 pixels for the final LAr scintillation light detection solution. This type has a PDE (32% at wavelength 465nm) which is comparable to the PDE of the SiPM100 (35%) and superior to the SiPM1600 (20%) [19]. However the dynamic range the SiPM400 it is better than the dynamic range of the SiPM100 (see Fig. 5.4). At the end of the section a measurement of the afterpulse probability is presented. This measurement was only performed for SiPM400.

6.2.1 Experimental setup

In order to study the SiPMs at different temperatures a setup was used that provided a continuously increasing temperature.
The three SiPMs (100,400 and 1600 pixel) and a PT100 for temperature monitoring were mounted in a light- and air-tight dewar. In addition aluminum foil was wrapped around the dewar to improve the light tightness. The dewar was filled with LN until all SiPMs and the PT100 were submerged in the LN. With time the LN evaporated and the LN level decreased. After enough LN evaporated the SiPMs were above the LN surface and in nitrogen gas. The temperature of the nitrogen atmosphere around the SiPMs increased as the LN surface decreased further (see Fig. 6.4). The increase of the nitrogen atmosphere's temperature was slow enough to perform measurements at stable conditions ($\Delta T/\Delta t =$ (211K in 140hours) $\approx$ 1.5K/h). The SiPMs were connected with 50Ohm coaxial cables to preamplifiers that were operated at room temperature. The bias circuit and the preamplifiers were mounted on the same printed circuit board (PCB) and at room temperature. The amplified signal was connected either to an oscilloscope or a data acquisition-system (DAQ) depending on the requirements of the experiment (see Fig 6.5).

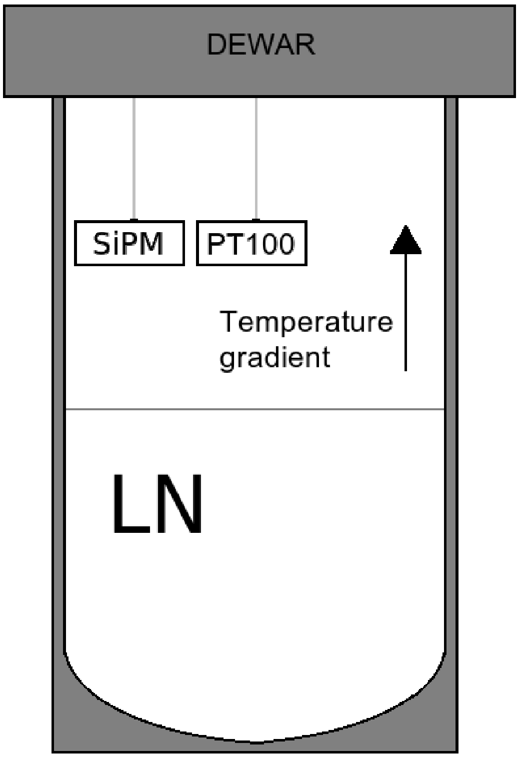

Figure 6.4: **Left:** Scheme of the setup in the dewar. The dewar was filled with nitrogen. As the LN evaporated the nitrogen atmosphere around the SiPMs slowly warmed up. The SiPMs were studies under slowly increasing temperatures. **Right:** picture of the dewar.

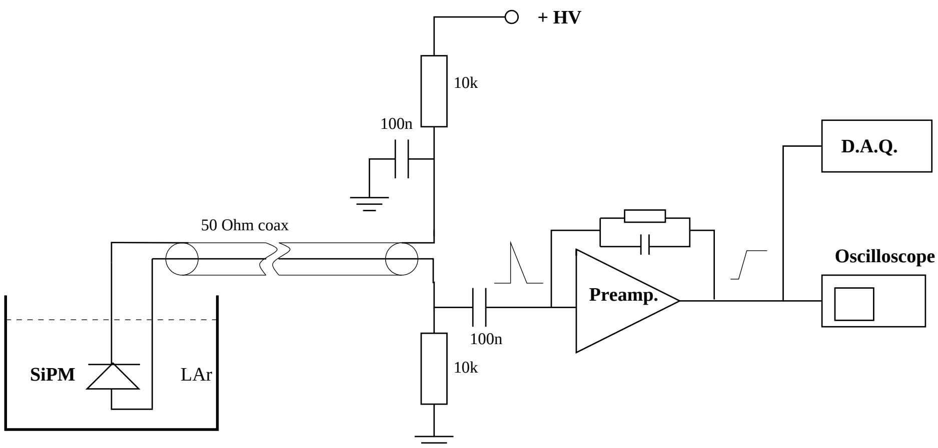

Figure 6.5: Electronic setup of the experiment. The SIPMs were operated in LN. The bias circuit and the preamplifiers were installed on the same PCB and operated at room temperature. In this figure the setup with the charge sensitive preamplifier is shown.

6.2.2 Waveform at cryogenic temperatures

In Fig 6.6 the waveform of the same SiPM (SiPM100) at RT and in LN is shown. The recorded waveforms show strong temperature dependence.
In liquid nitrogen the decay time of the pulse increases by a factor of $9.7^{+0.8}_{-0.6}$ compared to room temperature. Further a sharp peak was observed at the beginning of the pulse. The sharp peak is due to the parasitic capacitance that are hidden in the circuit (see Fig. 6.7). At room temperature this peak cannot be seen as its amplitude is lower than the amplitude of the main pulse at RT with which it coincides. The decay time of this parasitic pulse was too small to be resolved with our oscilloscope. It was below 1ns. The increase of the decay time can be explained by the temperature dependence of the

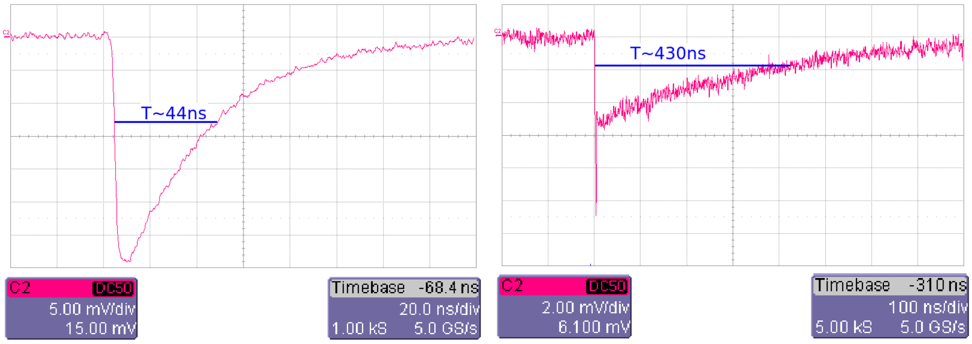

Figure 6.6: Left: Waveform of a SiPM at RT. **Right:** Waveform of the same SiPM in LN. The pulse at RT drops to 1/e of its original value after 44ns, the pulse in LN after 430ns. The two decay times differ by a factor 10.

resistance of the quenching resistor R (see Fig. 6.7). In Sec. 5.1 it was explained how R determines the decay time of a pulse ($\tau = R \cdot C$). In order to verify this explanation the resistance of the quenching resistor as a function of the temperature was measured. For this a forward voltage of 2V was applied to the SiPMs and the current was measured. At such a high forward voltage the diodes are open. Thus, the current is only limited by the resistance of the quenching resistors. In the SiPM $\mathrm{N_{pix}}$ identical resistors with the resistance R are connected in parallel, where $\mathrm{N_{pix}}$ is the number of pixels in a SiPM (see Fig. 5.2 in Sec. 5.1). The total resistance of the SiPM $\mathrm{R_{total}}$ is given as

$$\frac{1}{\mathrm{R_{total}}} = \sum_{i=1}^{\mathrm{N_{pix}}} \frac{1}{\mathrm{R}} \tag{6.1}$$

Thus the resistance of one quenching resistor R is

$$\frac{\mathrm{N_{pix}}}{\mathrm{R_{total}}} = \mathrm{R} \tag{6.2}$$

$\mathrm{R_{total}}$ is an ohmic resistance. Thus it is defined by $\mathrm{R_{total}} = \mathrm{V/I}$, where V is the applied voltage and I is the measured current. Thus R is given as

$$\mathrm{R} = \mathrm{N_{pix}} \cdot \frac{V}{I} \tag{6.3}$$

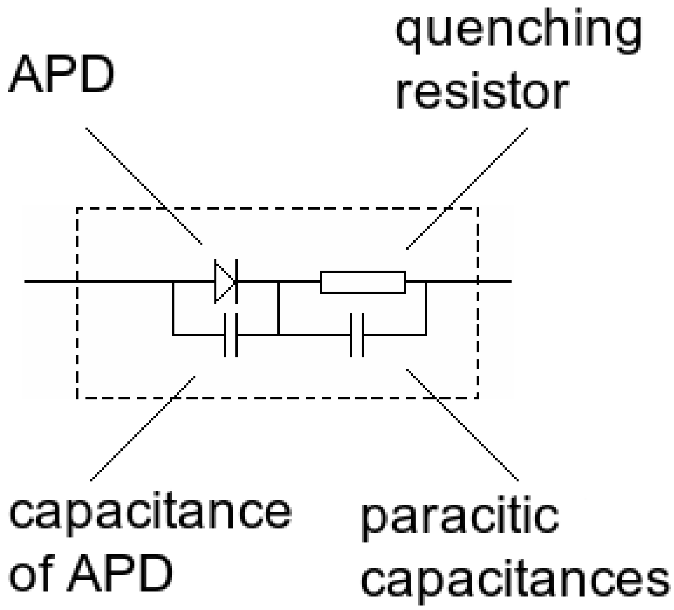

Figure 6.7: Effective circuit: The decay time is determined by the capacity of the APD cell and the quenching resistor. Parasitic capacitances lead to a fast component in the signal. This signal can not be seen at RT because it coincides with the primary signal and is smaller.

In Fig. 6.8 R was plotted as a function of the temperature. A significant temperature dependence of the resistance was observed. The ratio between the resistance at LN and RT was found to be 9.45 ± 0.34 (for the SiPM100).
This result matches well with our observation of the increasing decay time at LN-temperature. In all following experiments the long pulses and small amplitudes of SiPMs being operated in LN made it difficult to record good resolution spectra. This was in particular the case when the device was operated in noisy environment and separated by long cables from the front end electronics. This problem was later overcome by the usage of charge sensitive amplifiers. The amplitude delivered by the charge sensitive preamplifier is proportional to the integrated charge of the SiPM, which is temperature independent. Thus, a resolution in LN comparable to the one at RT was be achieved.

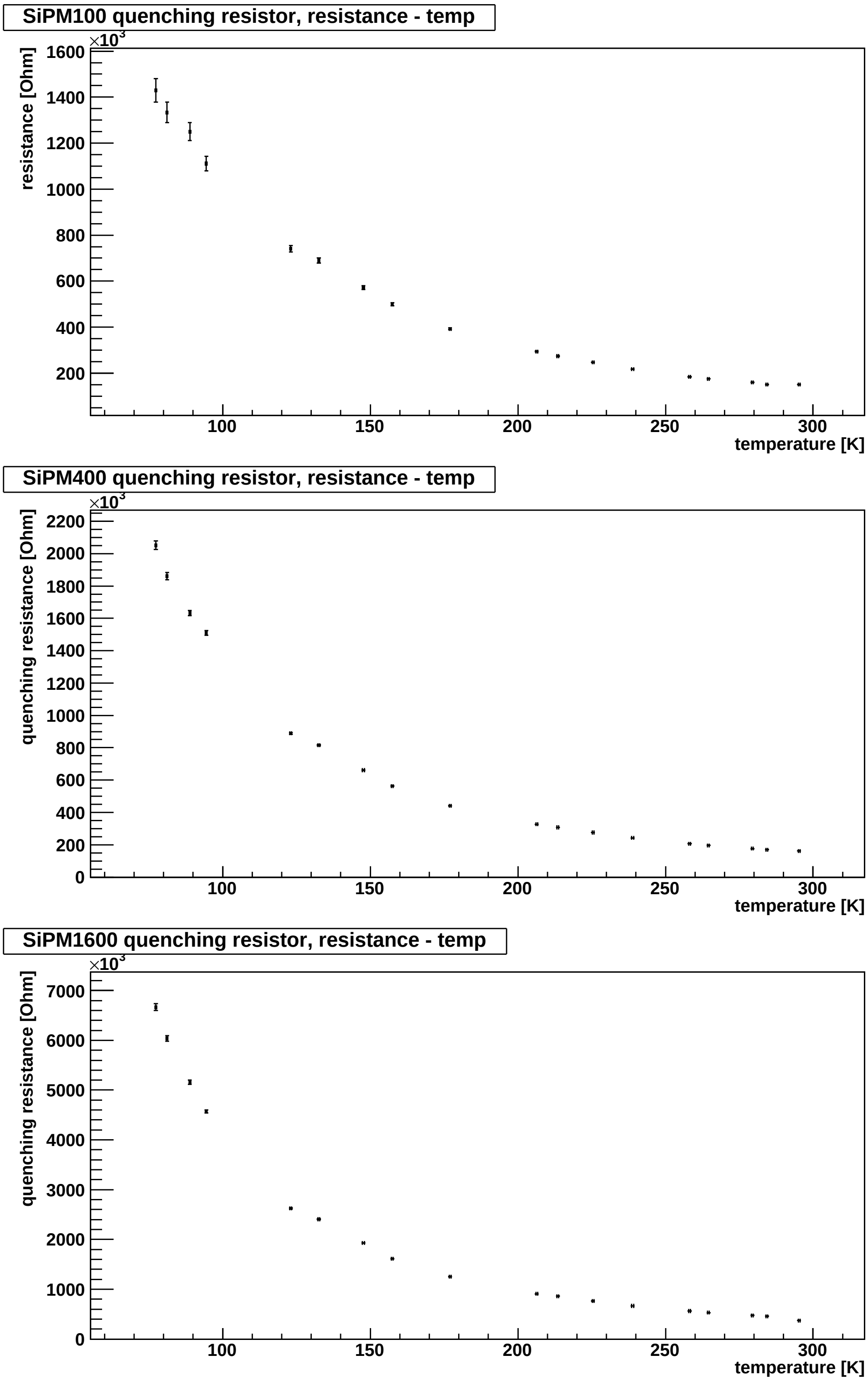

Figure 6.8: Resistance of one quenching resistor in the SiPM as a function of the temperature. The resistance was measured by applying forward voltage to the SiPMs and measuring the current. The resistance of an APD that is operated with forward voltage is negligible. Thus the resistance is quenching resistor could be deduced this way.

6.2.3 Dark rate and Crosstalk

Occasionally an APD cell fires without being illuminated. These events are typically thermally induced. The dark rate is the sum of these thermally induced pulses, their afterpulses and their cross-talk pulses in a unit time [20].

Dark rate as a function of the temperature: The setup described in Sec. 6.2.1 was used. In addition the SiPMs were covered with black tape to ensure that no UV or optical photons hit the SiPM. In the following the dark rate was measured at different temperatures but at constant V_{over}. An V_{over} of 1.5V for the SiPM100, 2.8V for the SiPM400 and 6.5V for the SiPM1600 was set. These over voltages are in the middle of the reasonable range of the individual SiPMs and higher than recommended by Hamamatsu.
Different methods of determining the dark rate were used depending on the frequency of the dark rate. Dark rates below 100Hz required long measurement times and were measured with the SiPMs being connected to charge sensitive preamplifiers (see 6.2.1) and read out by the DAQ. The charge sensitive preamplifiers were used because the rise time of linearly amplified pulses were so short (3-8 ns) that the DAQ system could not trigger on them. The charge sensitive preamplifiers integrate the pulse and thus increase the rise time of the pulse up to $\sim$400ns. The DAQ could trigger on such pulses.
With this setup spectra of the SiPM were recorded (see Fig 6.9). The spectra were integrated to get the number of dark events. The number of dark events was divided by the run time to get the rate.
The pile up veto of the DAQ rejects two consecutive pulses that are separated by less than $\sim 8\mu s$. Assuming that the pulses are uniformly distributed in time and given a dark rate of 100Hz, the probability of two consecutive pulses to trigger within $8\mu s$ is below 0.1% and thus still negligible. However dark rates above 100HZ had to be measured with the counting module (see Sec. 6.2.1) instead of the DAQ to be sure that the pile up veto did not affect the mesurement. For the measurement with the counting module the SiPMs were connected to the charge sensitive preamplifiers. The resulting signal was then fed into the shaping amplifier (see Sec. 6.2.1). This module delivered a Gaussian-like pulse with a width of 500ns and an amplitude which was 50 times the input amplitude. The shaping amplifier was used to separate pile up pulses. These pulses were fed into the discriminator. The discriminator delivered a uniform square shaped pulse for every input pulse with an amplitude above a threshold that could be set . These final pulses were fed into the counting module which counted the number of pulses. The number of counts within a given time is the dark rate.
For dark rates higher than 5kHz the charge sensitive preamplifiers were replaced by the linear preamplifiers (see 6.2.1). 1ms long traces were recorded with the oscilloscope (see Fig. 6.9). The dark rate was deduced from the number of p.e. peaks in the trace.
Linearly amplified and thereby short pulses were used because it is easier to count short pulses in a trace file than long pulses which often lie on top of each other.
The dark rates, received in the three different measurements, were plotted as a function of the temperature and are shown in Fig. 6.10. The error bars are the statistical errors

of the measurement. Dark counts are Poisson distributed. Thus, the statistical errors are given by the square roots of the measured counts. The errors are too small to be seen in Fig. 6.10.

The measured dark rate as a function of the temperature decreases exponentially with decreasing temperatures. At 170K the dark rate drops below 1Hz. At around 130K the curve flattens out. At these temperatures the rate is of the order of 10^{-2}Hz. This decrease can be explained with the absence of thermally induced pulses at low temperatures [21]. The out flattening might be explained by cosmic muons. Assuming a rate of cosmic muons of 1 muon per minute and cm^2 [29] and a PDE of 25% one calculates a count rate of $1.5 \cdot 10^{-2}$Hz. This number is close to the measured dark rates at very low temperatures.

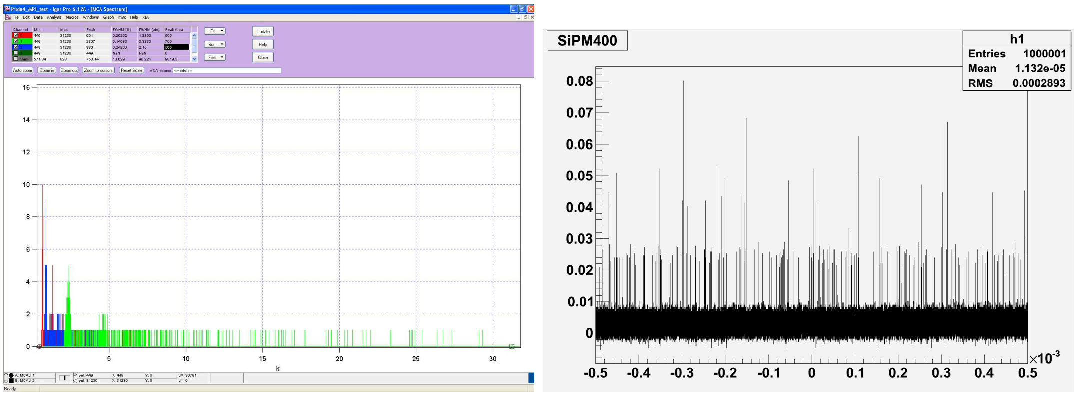

Figure 6.9: Right: For dark rates below 100Hz the SiPMs were connected to the DAQ and a spectrum was recorded. The dark count is the integral of the spectrum. **Left:** Dark rates above 5kHz were measured with the oscilloscope. A 1ms trace was recorded and the number of events was counted.

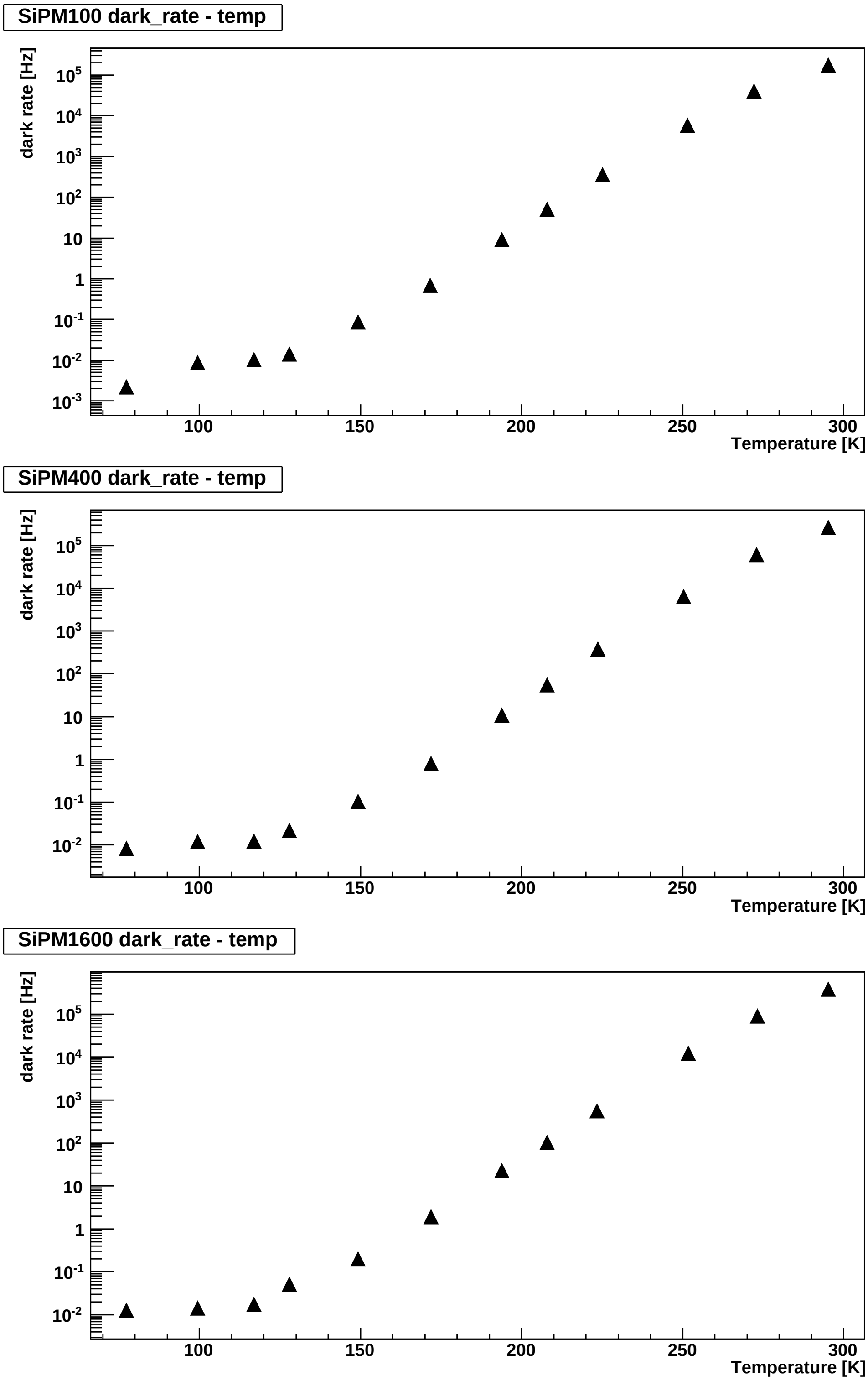

Figure 6.10: Dark rate as a function of the temperature for SiPMs with 100, 400 and 1600 pixels.

Cross talk as a function of the temperature: In all dark rate measurements the dark rate was below 10^6Hz. Given such a rate and assuming that the dark events are distributed uniformly in time, two dark events are on average separated by 1μs. Multiple pixel dark events are dark events that are separated by less than the rise of a pulse which is <10ns. Thus the probability of a multiple pixel dark event is less than 1%. Therefore nearly all dark two pixel events must come from cross talk between the pixels. The number of one pixel events and the number of two pixel events were deduced for dark rate measurements at different temperatures. The fraction of dark two pixel events to the sum of the one pixel and two pixel events can be used to approximate the cross talk probability.
With the same argumentation as above the fraction of the three pixel events can be deduced to verify the measured cross talk probability, but for most of the measurements the count rates were too low to identify the 3p.e. peak. The count rate was slightly higher for many pixel events (n>30). However these events are due to cosmic muons and external radioactivity and not due to the dark rate. Fig. 6.11 shows the calculated cross talk probability as a function of the temperature. In the measurement the same V_{over} as in the dark rate measurement were used. The errors in Fig. 6.11 are the statistical errors of the dark count that were treated with error propagation.
As a result the cross talk probability can be regarded as temperature independent. Deviations can be explained with fluctuations in the V_{over}.

Dark rate as a function of the overvoltage. With the same setup as above the dark rate as a function of V_{over} was measured at room temperature. Since the dark rate at room temperature is higher than 5kHz the method that based on a 1ms trace was used. Fig. 6.12 shows the dark rate as a function of V_{over}. The dark rate increases exponentially with V_{over}. This is well understood and matches with the results of other groups [21] [30].

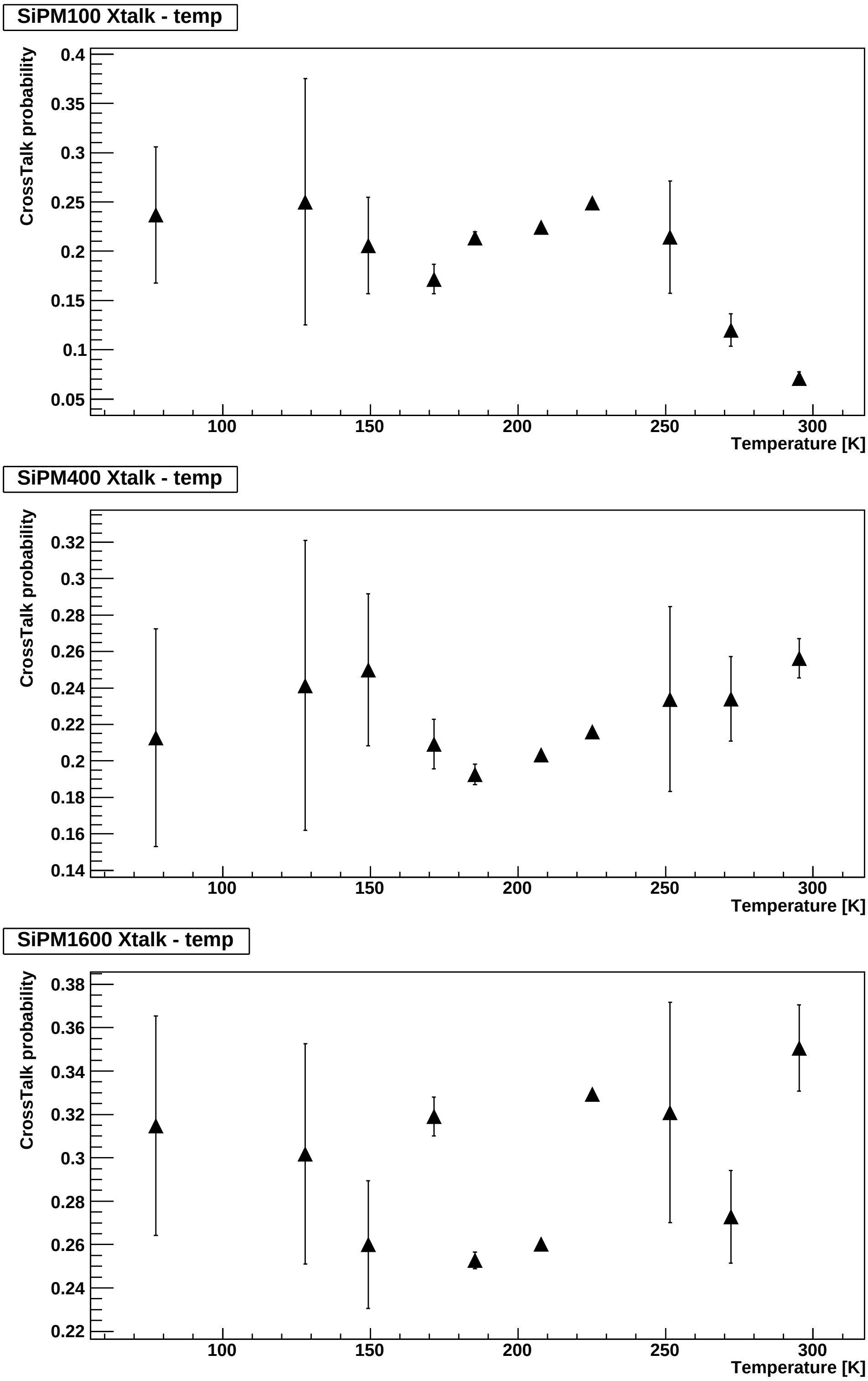

Figure 6.11: Cross talk as a function of the temperature for SiPMs with 100, 400 and 1600 pixels.

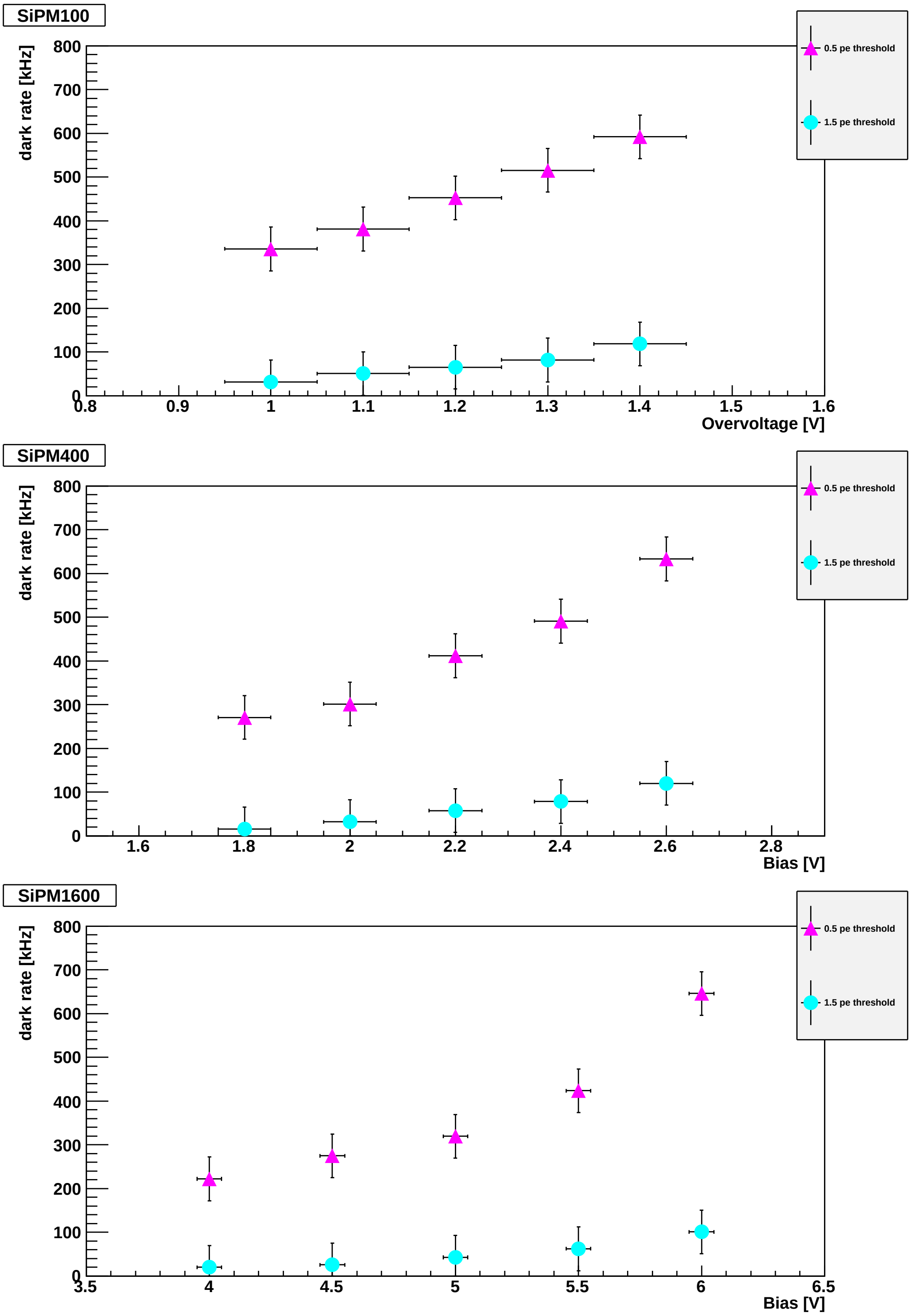

Figure 6.12: Dark rate as a function of the over voltage for SiPMs with 100, 400 and 1600 pixels.

6.2.4 Gain Measurement and breakdown voltage calculation

Gain measurement In order to measure the gain one has to measure the charge of the one p.e. events. For this the SiPMs were connected to charge sensitive preamplifiers. The charge sensitive preamplifiers integrate the pulse. The amplitude of their response is proportional the discharge of the SiPM. The preamplifiers were connected to the DAQ and spectra were taken. The spectra were calibrated into units of charge. This was done by connecting a 1pF capacitor to the system which was pulsed with a pulser of known voltage. In the calibrated spectra the position of first peak delivered the charge of one p.e. events.

Spectra were taken at different temperatures and for different bias voltages. In each measurement the charge of the one p.e. events was extracted through fitting the 1p.e. peak in the spectrum. In order to prevent pile up dark events were measured instead of photon induced events. The avalanche mechanism for dark events is the same as for photon induced events. Therefore there is no difference in the gain for the two different kinds of events.

In Fig. 6.13 the gain as a function of the bias voltage is shown for different temperatures. Each line corresponds to a set of measurements at a fixed temperature. Each point on these lines corresponds to a measurement at a certain bias voltage. The gain as a function of the bias voltage was fitted with a linear function for each temperature individually. The error bars come from the Gaussian fit of p.e. peaks in the spectra. The standard deviation of the fit was taken and propagated into the errors of the the final gain.

At high dark rates pile up biased the measurement. The measurement at high temperatures ($\gtrsim$ 220K) thus suffer from a systematical error that is due to pile up.

In Fig. 6.13 the following features can be observed.

1. SiPMs can be operated at a gain of 10^5 to 10^6 at all studied temperatures
2. With increasing bias voltage the gain increases linearly
3. The slope is nearly the same for all studied temperatures
4. The bias voltage necessary to operate SiPMs at a given gain increases with the temperature

No. 4 is due to the temperature dependence of the breakdown voltage as will be shown.

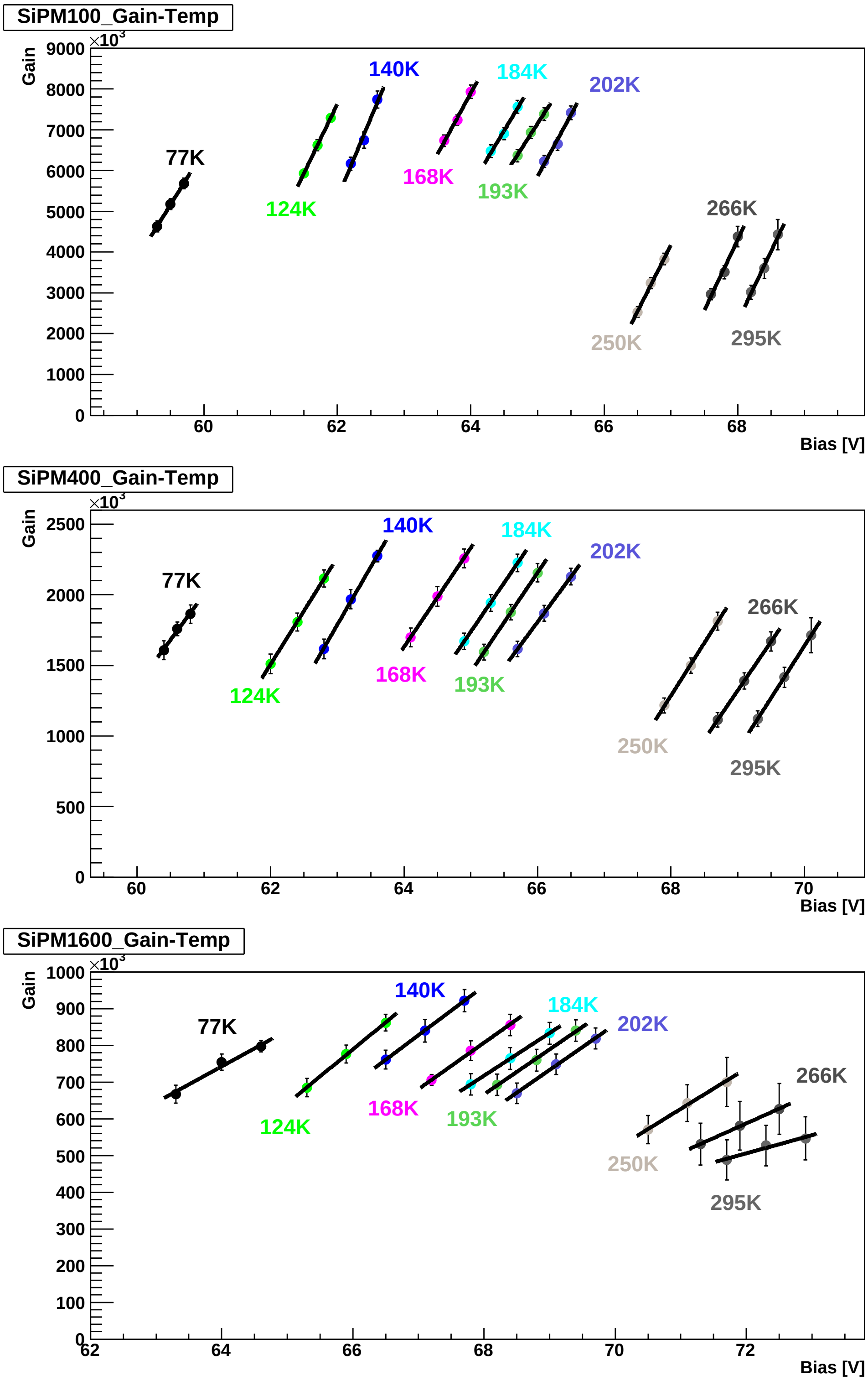

Figure 6.13: Gain as a function of the bias voltage at different temperatures. Each line stands for a set of measuremtents at a certain temperature and each point on these lines is the measured gain for certain bias voltage. The values at higher temperatures are biased by pile up effects.

Breakdown voltage calculation The fits of the gain measurement were extrapolated to the point of gain=0 which is by definition the breakdown voltage V_{Br}. This way V_{Br} was extracted for different temperatures. It was observed that V_{Br} increases with the temperature. The relatively large error bars are due to the errors from the fit. The data was fitted with a linear function.
The decrease of the breakdown voltage with decreasing temperatures can be explained with the increase of the charge carrier mobility at low temperatures. At low temperatures the scattering rate of the charge carriers with phonons and other charge carriers decreases. As a results the charge carrier mobility increases. Charge carriers with higher mobility reach the required energy for the avalanche effect already at weaker electric fields [21].
Due to the temperature dependence of the breakdown voltage different bias voltages have to be used for SiPMs at different temperatures. The exact value of the gain is a function of V_{over}. V_{Bias} has to be reduced at low temperatures in order to keep V_{over} constant. Knowing the breakdow voltage as a function of the temperature one can now operate the SiPM at any temperature at the same over voltage.

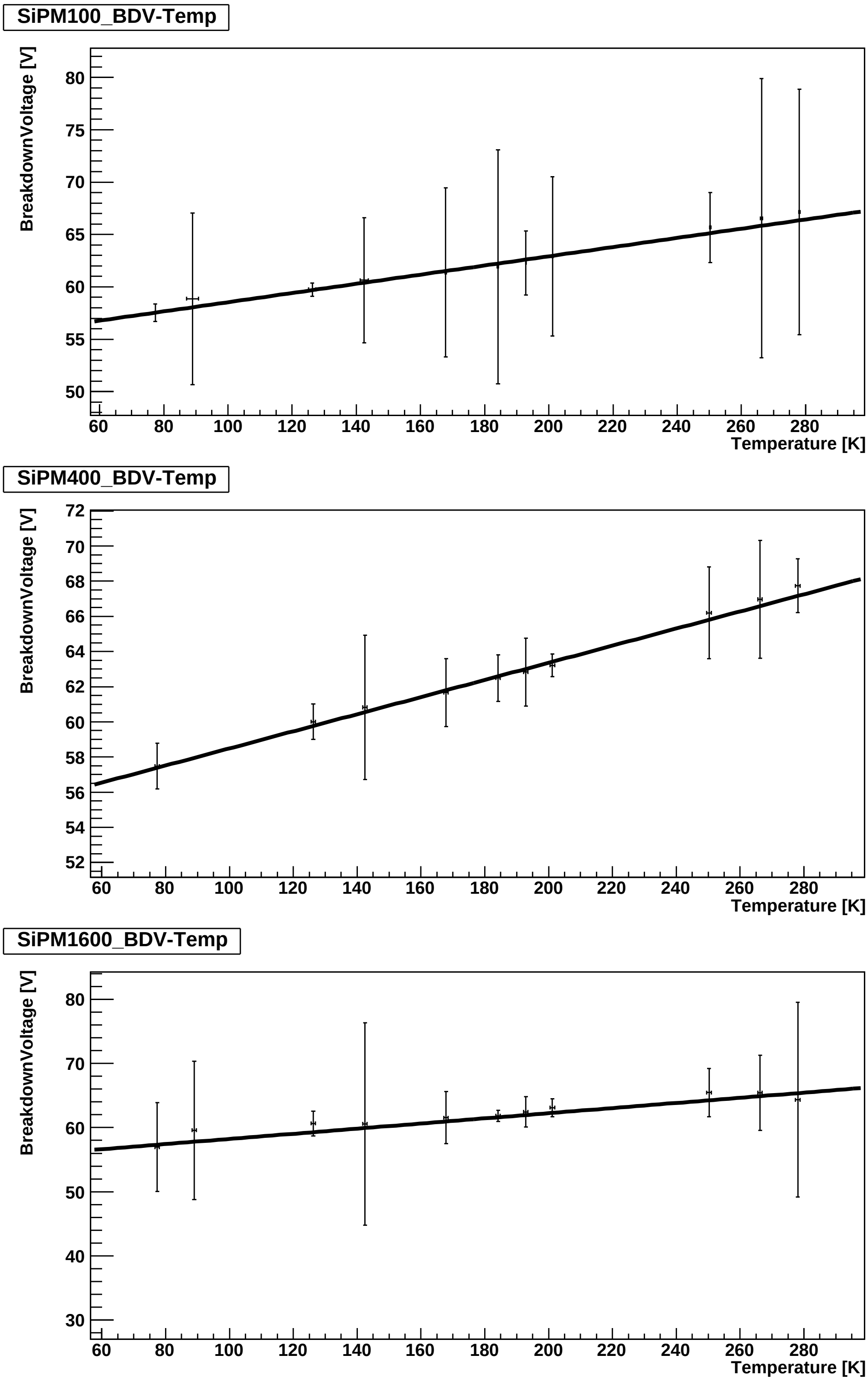

Figure 6.14: Calculated breakdown voltage as a function of the temperature for SiPMs with 100, 400 and 1600 pixels.

6.2.5 Afterpulses

For this measurement the setup presented in Sec. 6.2.1 was used. The afterpulse probability as a function of the bias voltage was estimated. As the SiPM400 was the only type used for the LAr anti-Compton veto it is also the only type for which the afterpulse probability was measured.
The dewar was closed in an air and light tight way. Then the additional light shield around the top of the dewar was removed slowly until a SiPM signal with 100Hz was measured . The SiPM was triggered only by the environmental light. The measured light intensity was so low that nearly all events were one p.e. events (see Fig. 6.15). In the following the bias voltage of the SiPM was increased in small steps. A spectrum was recorded with the DAQ for every bias voltage. In the spectra the number of events in the 1p.e peak was calculated as well as the number of events between the 1p.e. and 2p.e. peak (see Fig. 6.15). From the literature it is known that nearly all afterpulses come within ns after the original pulse [21]. Afterpulses that come after the recovery time of the SiPM (∼500ns) cannot be identified as afterpulses.
The triggering of an afterpulse after a regular p.e. pulse leads to an additional discharge. Since charge sensitive preamplifiers were used the amplitude of the two pulses sum up. As the discharge of the afterpulse is smaller than the discharge of the regular pulse the amplitude recorded by the DAQ will be between the amplitude of an 1p.e pulse and a 2 p.e pulse. Thus in the spectrum afterpulse events $\mathrm{N_{ap}}$ are the events that are between the 1p.e. and the 2.p.e. peak (see Fig. 6.15). One can estimate the afterpulse probability by :

$$\mathrm{p} = \frac{\mathrm{N_{ap}}}{\mathrm{N_{ap}} + \mathrm{N_{1p.e.}}} \tag{6.4}$$

where $\mathrm{N_{ap}}$ is the number of afterpulse events and $\mathrm{N_{1p.e.}}$ the number events under the 1p.e. peak.
In this model we can regard $\mathrm{N_{ap}} + N_{1p.e.}$ as the number of trials and $\mathrm{N_{ap}}$ as the number of successes to get a binomial distribution where the the standard deviation σ of the afterpulse probability is given by

$$\sigma^2 = \langle p\rangle(1 - \langle p\rangle)\frac{1}{\mathrm{N_{ap}} + \mathrm{N_{1p.e.}} + 3} \tag{6.5}$$

$\langle \mathrm{p}\rangle = \frac{\mathrm{N_{ap}}+1}{\mathrm{N_{ap}}+\mathrm{N_{1p.e.}}+2}$ is the expectation value of p.
The measured afterpulse probability was plotted against the over voltage voltage of the SiPM and the data was fitted with an exponential function (see Fig 6.15). The error bars in the figure are given by Eq. 6.5. Our estimate of the afterpulse probability is consistent with other measurements [21].
Events with multiple afterpulses can also lead to amplitudes between the 1.p.e and the 2.p.e. peak and thus bias our estimate. However for this the discharge of all afterpulses together must not exceed the discharge of a regular one p.e. event. Furthermore every afterpulse will scale with the afterpulse probability which is below 0.37. Thus the contribution of these effects will be below 0.1.

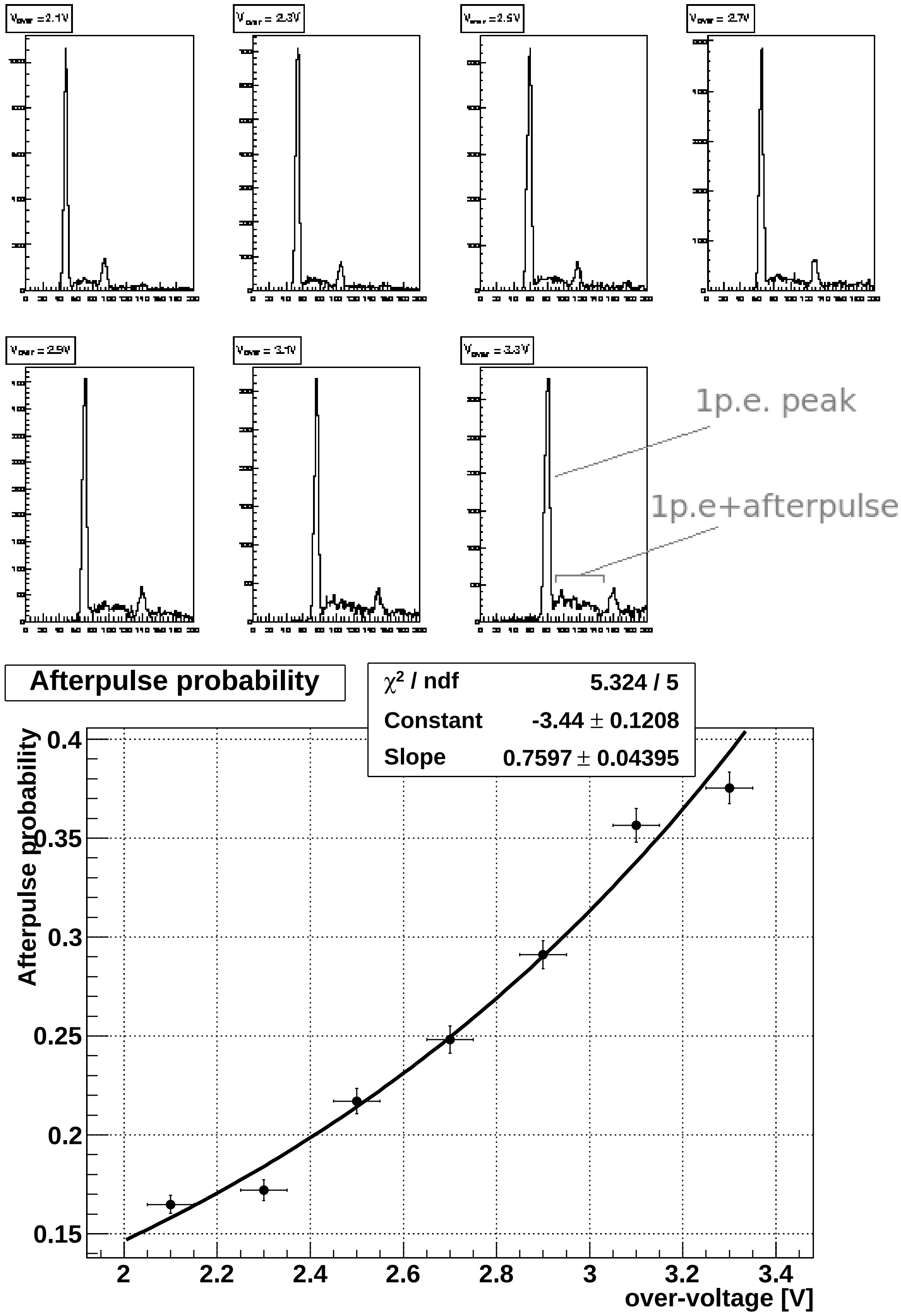

Figure 6.15: Up: Spectrum of the SiPM400 at different V_{over} at LN temperature. The events between the first and the second p.e. peak are attributed to afterpulses.**Down:**The measured afterpulse probability as a function of V_{over} was fitted with an exponential function.

6.2.6 Conclusion

In can be concluded that the studied SiPMs can be operated at LN temperature at about the same gain as at room temperature. At LN temperature the dark rate is negligible for all three SiPMs. Their cross talk probability does not change with the temperature.
One drawback for the operation of SiPMs in LN is the change of the SiPM waveforms. At LN temperature the pulses become longer and the amplitudes smaller resulting in a worse resolution. This problem can be overcome by using charge sensitive preamplifers.

Further the afterpulse probability of the SiPM400 was investigated at LN temperature. It was found out that afterpulse probability is between 17% and 37% depending on V_{over}.

Chapter 7

Liquid argon scintillation

Argon is the chemical element with atomic number 18. Argon is a noble gas and the third most abundant gas in the atmosphere.
Table 7.1 lists some basic properties of LAr that will be of use.

Table 7.1: Liquid Argon properties

Density at 87.3K and 1 bar	1.4g/cm^3
Boiling point at 1bar	87.3K
Refraction index	1.22

7.1 Scintillation mechanism

The electron configuration of an argon atom in its ground state is [Ne](3s)^2 (3p)^6, resulting in a $^1S_0$ state. This state can be excited by lifting an electron to the 4s shell. There the electron can occupy a state of parallel or anti-parallel spin with respect to the rest of the atom. If the two spins are anti-parallel they combine to a singlet state $^1P_1$, if they are parallel they combine to a triplet state $^3P_0$, $^3P_1$ or $^3P_2$ [31].

Table 7.2: Argon's lowest atomic energy levels [31].

configuration	state	Energy [eV]
$[Ne]3s^23p^6$	$^1S_0$	0
$[Ne](3s)^2(3p)^5\uparrow(4s)^1\downarrow$	$^1P_1$	11.82
$[Ne](3s)^2(3p)^5\uparrow(4s)^1\uparrow$	$^3P_0$	11.72
$[Ne](3s)^2(3p)^5\uparrow(4s)^1\uparrow$	$^3P_1$	11.62
$[Ne](3s)^2(3p)^5\uparrow(4s)^1\uparrow$	$^3P_2$	11.54

When ionizing radiation penetrates LAr it does not cause any permanent chemical changes. But it ionizes and excites argon atoms. Being a noble gas argon usually does

not occur in molecular form, but in certain excited states. When being ionized argon atoms can form bonds with other atoms. A composition of one excited and one regular argon atom is called excimer (excited dimer) Ar_2^* [32].
Among the four low lying excited atomic states only the $^3P_1$ and the $^3P_2$ form excimers. Therefore two distinct excimer states arise: A singlet-state $^1\Sigma_u = (^3P_1 + {}^1S_0)$ and a triplet state $^3\Sigma_u = (^3P_3 + {}^1S_0)$ [32]. While the decay of $^1\Sigma_u^+$ ($\tau(^1\Sigma_u^+) = 6$ ns) is allowed the decay of $^3\Sigma_u^+$ is forbidden by angular momentum conservation. Thus the $^3\Sigma_u^+$ state has a much longer lifetime ($\tau(^3\Sigma_u^+) = 1.59\mu$s) [33]. The scintillation light of pure argon always contains both components. Light due to the decay $^1\Sigma_u^+$ is called fast component and light due to the decay $^3\Sigma_u^+$ is called slow component. For electrons or photons the ratio of the two components is $I_{\text{fast}}/I_{\text{slow}}$=0.3 [34].

LAr scintillation light is predominantly produced through the decay of these two states into the ground state. The distinct peaks of the single and triplet state cannot be resolved because various rotational energy levels of both excimer states overlap [35]. Therefore only a broad peak can be measured. The authors of [36] measured the emission peak at 128nm with a FWHM of 10nm.

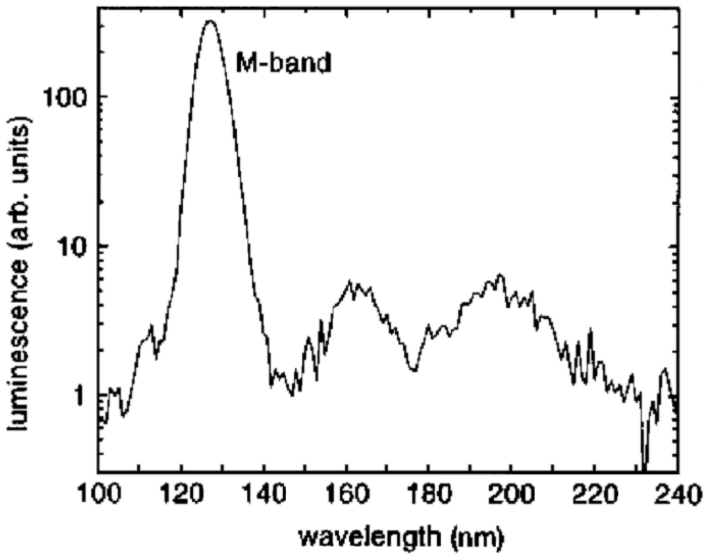

Figure 7.1: LAr scintillation spectrum, peaks at a wavelength of 128nm

Table 7.3: Liquid Argon scintillation properties

wavelength (peak value)	128nm [36]
attenuation length in LAr	(0.66±0.03)m [37]
light yield	(42.4±0.5)photons/keV [38]

Photons that come from the direct decay of excited atoms Ar^* are resonance trapped and thus have a short attenuation length. Photons from excimer decay however do not have enough energy to get absorbed by argon atoms and Argon dimers Ar_2 that could in principle absorb them are hardly present. Thus the attenuation length of photons of this wavelength is very high. In table 7.3 some crucial parameters of the LAr scintillation light are listed.

7.2 Excimer formation

Excimers Ar_2^* can be formed when ionizing radiation passes through argon. There are two different mechanisms how this can happen. Either through direct excitation or via ionization.
Both mechanisms produce the short living ${}^1\Sigma_u^+$ state and the long living ${}^3\Sigma_u^+$ state.
In the following the two mechanisms are detailed. A summary of both mechanisms is given in Table 7.4.

Direct excitation: An argon atom is excited directly by radiation. The excited atom Ar^* posses a binding potential towards regular argon atoms. It thus can form an excimer Ar_2^* together with a regular atom. Because of angular momentum conservation excimer formation can not occur in a two body collision.

Ionization: In a first step an argon atom Ar gets ionized. Its electron thermalises in the environment of the resulting ion Ar^+ on a time-scale of $\mathcal{O}(100ps)$. Thus the ion can form a charged dimer Ar_2^+ with a regular argon atom Ar before the electron and the ion can form an e^--ion pair [39]. In this case the recombination of the electron with the charged dimer Ar_2^+ splits up the dimer creating a highly excited atom Ar^{**}. However for this recombination to happen the electron must have thermalised within a critical radius, the Onsager radius [40]. The highly excited atom Ar^{**} can then de-excite non-radiatively into a regularly excited atom Ar^* [41]. Now the excited atom forms an excimer Ar_2^* as explained above.

The ratio of excitation to ionization in LAr is $\sim$1:2 [42].

7.3 Quenching mechanisms and total light yield

In order to estimate the light yield it is necessary to take into account processes that reduce the number of excimers producing photons and thus quench the scintillation light.

Table 7.4: Excimer production mechanisms

Direct excitation:		
$\gamma + \mathrm{Ar}$	$\rightarrow$	Ar^*
$\mathrm{Ar}^* + \mathrm{Ar} + \mathrm{Ar}$	$\rightarrow$	$\mathrm{Ar}^*{}_2 + \mathrm{Ar}$
Ionisation:		
$\gamma + \mathrm{Ar}$	$\rightarrow$	$\mathrm{Ar}^+ + \mathrm{e}^-$
$\mathrm{Ar}^+ + \mathrm{Ar} + \mathrm{Ar}$	$\rightarrow$	$\mathrm{Ar}_2^+ + \mathrm{Ar}$
$\mathrm{Ar}_2^+ + \mathrm{e}^-$	$\rightarrow$	$\mathrm{Ar}^{**} + \mathrm{Ar}$
Ar^{**}	$\rightarrow$	$\mathrm{Ar}^* + \mathrm{heat}$
$\mathrm{Ar}^* + \mathrm{Ar} + \mathrm{Ar}$	$\rightarrow$	$\mathrm{Ar}_2^* + \mathrm{Ar}$

Bi-exitonic self quenching: In this process two excitons combine forming a regular argon atom and an ion.

$$\mathrm{Ar}^* + \mathrm{Ar}^* \rightarrow \mathrm{Ar} + \mathrm{A}r^+ + e^-. \tag{7.1}$$

Although the ion can again form an exciton, as discussed above, one exciton is lost in total [34]. The probability of this process scales with the exciton density.

Escaping electrons: After the ionization process the electron might thermalise beyond the Onsager-radius [40]. Electrons that thermalise behind the Onsager radius do not recombine with the ion. The third process described in the in Table 7.4 does not occur. The excimer can not be formed - at least not in the time frame of the measurement.

In [41] a theoretical estimation of the scintillation light yield in pure argon is given that takes into account these two processes. The calculated light yield is (41 ± 2)photons/keV. This result agrees well with the experimentally obtained light yield of (42.4 ± 0.5)photons/keV [38] .
However contaminations of LAr with impurities also quench the scintillation light. Prominent quenching processes are:

Charge carrier trapping: Electrons happen to get captured by electro-negative impurities, most notably oxygen, preventing the recombination of the electron with the ion and thus interrupting the excimer production. This process scales with the argon impurity.

Electronic energy transfer to impurity atoms: Collisions with impurity atoms can lead to the transfer of the excitation energy of an excimer to the atom. Thus excimers are lost and the scintillation light is quenched [31] [43]. This is in particular the case for nitrogen.

$$Ar_2^* + N_2 \rightarrow 2Ar + N_2 \tag{7.2}$$

Because of the different lifetimes quenching is different for the the $^1\Sigma_u^+$ and the $^3\Sigma_u^+$ state. In [43] it was found that the life time of $^3\Sigma_u^+$ is a function of the impurity concentration of N_2. This can be understood by the increased probability for radiation less excimer disintegration.
In Fig:7.2 (taken from [43]) it can be seen, that electronic energy transfer is a effective quenching mechanism. The lifetimes of the distinct components of the scintillation light are given as functions of the N_2 contamination.

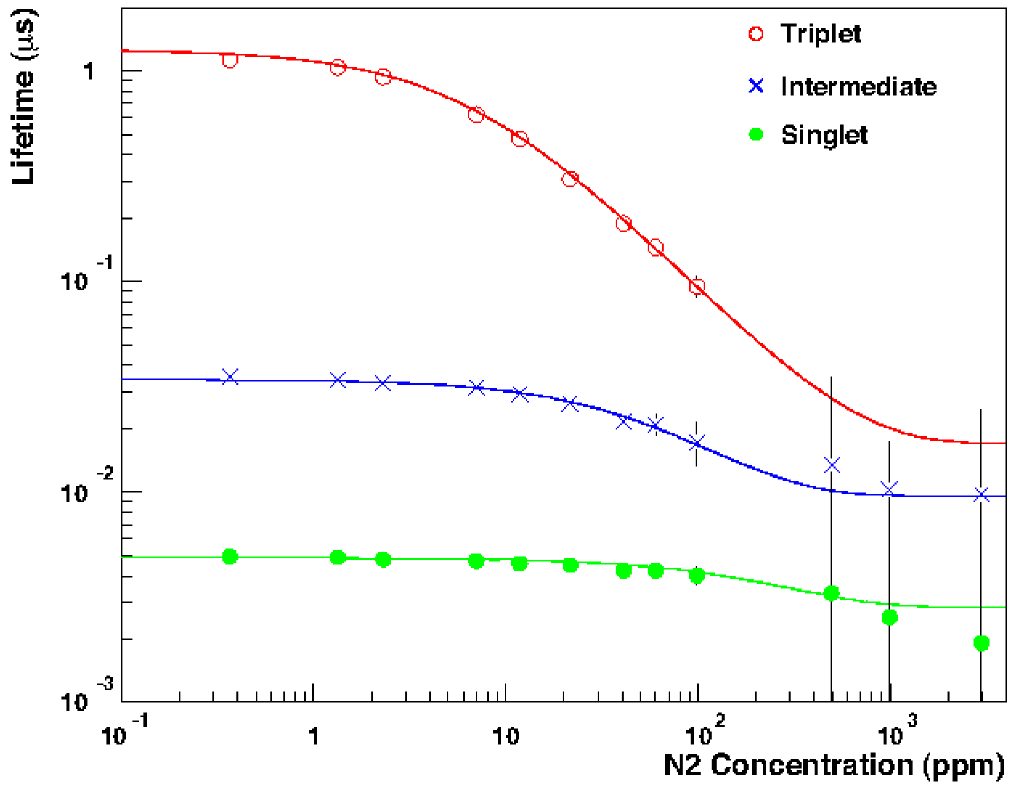

Figure 7.2: Figure taken from [43]. Lifetime of the triplet and the singlet state as a function of the N_2 contamination (for details see [43]).

Chapter 8

A SiPM based LAr-spectrometer

In chapter 5 the suitability of the SiPMs being operated at cryogenic temperatures was proven. This knowledge was used to build a LAr spectrometer that is based on SiPMs. The main design feature was the operation of the bare SiPM directly in LAr. The assembling and the operation of the LAr-spectrometer are described in this chapter.

The design of the setup is shown in Fig. 8.1. A dewar was filled with LAr and closed in a light and air tight way. Inside the dewar nearly all surfaces of the dewar and the support structures were covered with reflecting mirror foils creating a contained light cavity. In the dewar light guides were coiled up around the dewar walls and the SiPMs were connected to the ends of the light guides.

Ionizing radiation that passes the LAr creates scintillation light. As explained in chapter 7 LAr scintillation light peaks at 128nm (see Sec. 7.1). The peak sensitivity of the used SiPMs is at 400nm. Thus, scintillation light has to be shifted to longer wavelength before it can be detected. In the experimental realization the UV-light is shifted with the large area mirror foils. It was found that the scintillating VM2000 foil with a reflectivity of $\sim$95% was suited for this design. To improve the wave length shifting (WLS) of the foil it was coated with a fluorescent dye, TPB. The coating absorbs LAr scintillation and emits blue light. Thus the incident light is shifted on the foils to the optical wavelength and then trapped in the cavity until it is detected or absorbed.

The sensitive surface of the SiPMs is very small. This makes efficient light detection difficult. To overcome this problem the SiPMs are connected to optical light guides. This way the effective surface of the SiPM is defined by the surface of the optical light guides multiplied with some light trapping efficiency. The light guide used in the setup is in addition wave length shifting (WLS). In the following the light guide will be referred to as WLS fiber. The WLS fiber shifts the light from blue to green wavelength. The fiber was connected to the SiPMs with a homemade optical coupling.

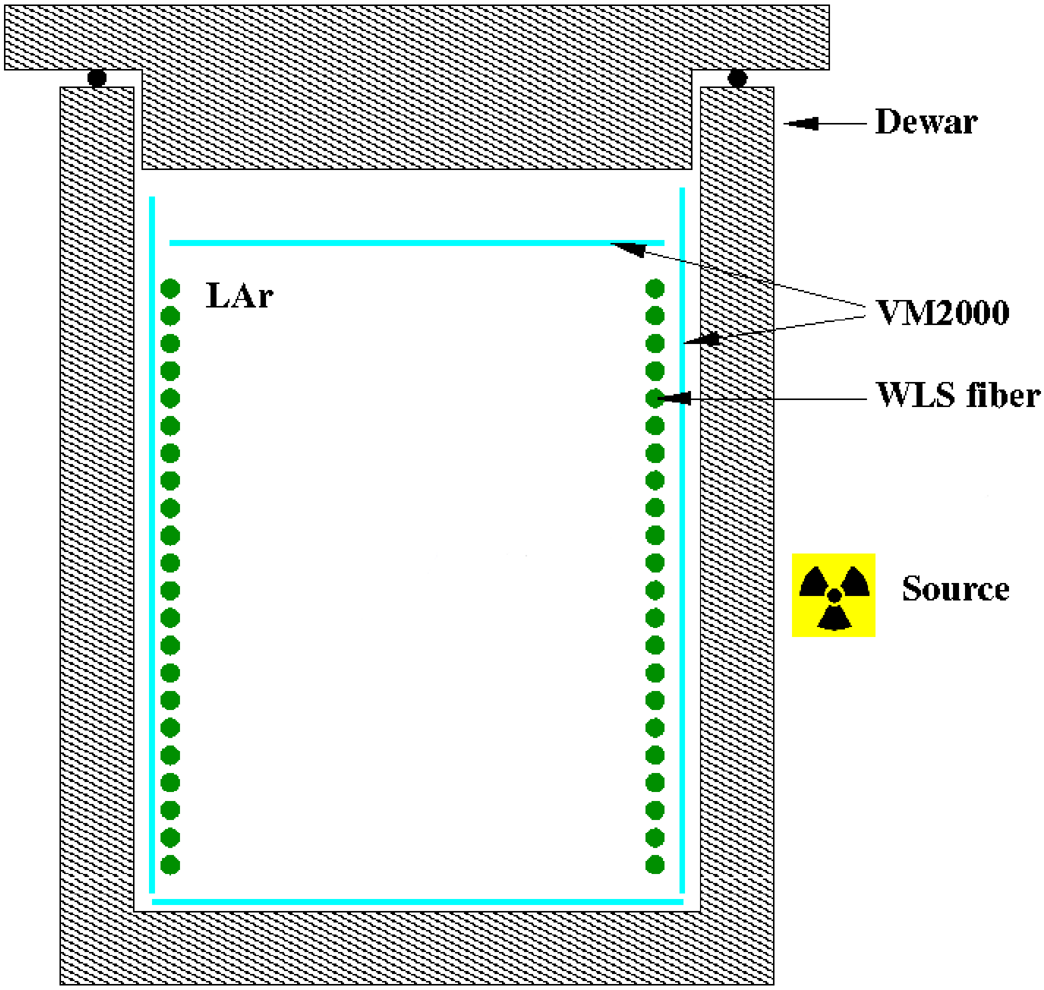

Figure 8.1: Setup of the LAr-spectrometer. The inner walls of a dewar are covered with reflecting mirror foil. Light guides are coiled up along the dewar walls. To the end of the light guides SiPMs are connected. The dewar is filled with LAr.

8.1 Components

In this section the mirror foil, its coating, the WLS fiber and the optical coupling will be presented. Characterizations of the individual parts are given, light collection efficiencies are measured and discussed.

8.1.1 The mirror foil

The used mirror foil is sold under the name $3M^{TM}$ radiant mirror Film [44]. It is also known as VM2000 foil. In [45] it was reported that this mirror foil has a reflectivity of ~95%. It is in addition scintillating. Its scintillation light peaks at 430nm (see 8.2).
In order to improve the detection efficiency of the LAr scintillation light the scintillation properties of the foil were improved. For this the foil was coated with a dye that fluoresces in the sensitive range of the SiPMs.

The mirror foil consists of poly-ethylene-naphtalate (PEN) that resistant to most common solvents. In order to attach any fluorescent dye to the foil the dye was solved in toluene. Toluene weakly solubilises PEN and thus creates strong bonds between the foil and possible dyes.
In [46] it was proven that poly-styrene (PST) doped with tetraphenyl-butadiene (TPB) and solved in toluene is a suitable dye to shift LAr scintillation light to the optical range. When the toluene evaporates PST and TPB remain. The PST absorbs the UV-scintillation light from the LAr and transfers the absorbed energy non-radiatively to the TPB. The TPB emits photons in the optical range. The emission of TPB peaks at 450nm [47].
PST is transparent to the fluorescence light of TPB. Both materials are soluble in toluene. Fig. 8.2 [46] shows the emission spectrum of the mirror foil coated with different concentrations of TPB in PST. From the plot it is evident that the best emission in the optical range can be achieved with a concentration of 10% TPB in PST.

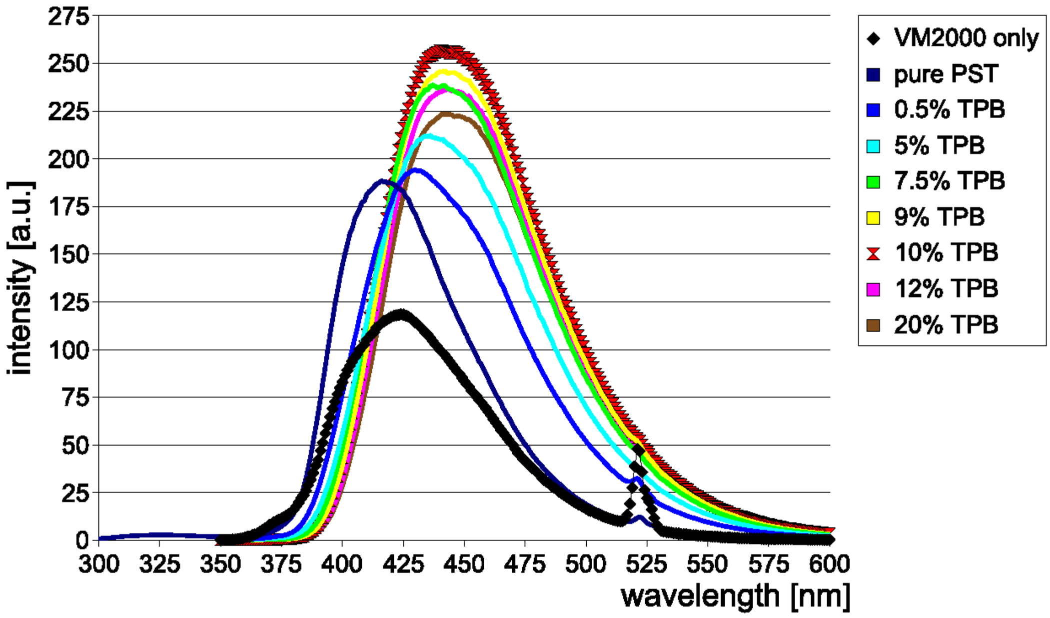

Figure 8.2: Emission spectrum of the mirror foil with different coatings. The excitation wavelength was 260nm. The best emission was achieved with a coating of 10% TPB in PST. Taken from [46].

A 10% TPB in PST solution was painted to the VM2000 foil with a tissue. The surface tension of the solution formed a smooth film on the foil. No inhomogeneities could be observed. The foil was exposed to air until the toluene evaporated.
The wave length shifting was verified by illuminating the foil with a UV-LED (λ=290nm) and visually observing blue fluorescence light.

8.1.2 The optical coupling

In order to couple the SiPMs to the WLS fiber an optical coupling was developed together with the engineering department of the MPI für Physik, München. The main design

feature of the coupling is the option to adjust the precise position of the fiber-end relative to the SiPM. The technical drawing is shown in Fig. 8.3. The coupling consists of an aluminum main body (1) and a plastic block (2). Both are connected via four screws (23). Another four screws are placed in the aluminum body perpendicular to the fiber (21). With these screws the precise position of the fiber can be tuned. A SiPM can be placed at the bottom of the main body. The two connectors of the SiPM stick out of the coupling such that the SiPM can be connected to the voltage supply.
Before the plastic block and the aluminum body are connected the fiber has to be glued into the plastic block. For this the fiber is led through the plastic block such that ∼1cm of the fiber sticks out. Epoxy glue is then attached to the fiber-end that is sticking out. The fiber is then pulled into the plastic block such that there little layer of glue remains between the fiber and the plastic block. Finally the construction is stabilized with a fixing guide (see Fig. 8.4) that prevents the fiber from twisting inside the plastic block.

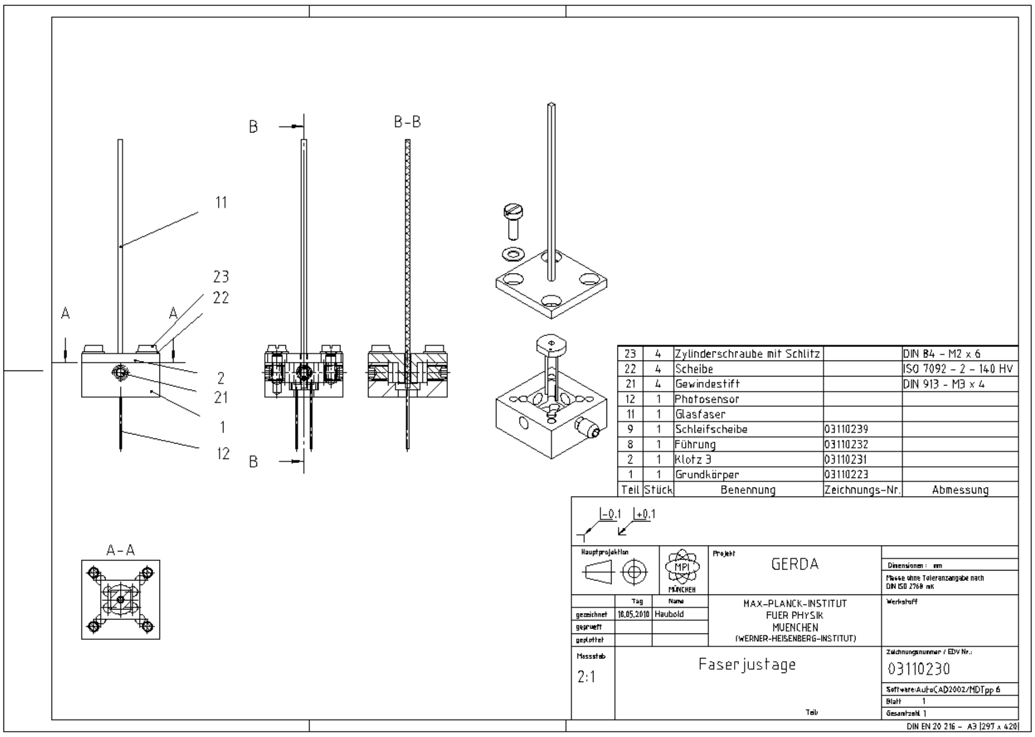

Figure 8.3: Technical drawing of the optical coupling. It consists of an aluminum main body, a plastic block and eight screws. The fiber is glued into the plastic block. The plastic block is then screwed onto the aluminum main body. Four screws are placed in the main body perpendicular to the fiber. These screws are used to adjust the exact position of the fiber. A SiPM is placed at the bottom of the main body with its connectors sticking out.

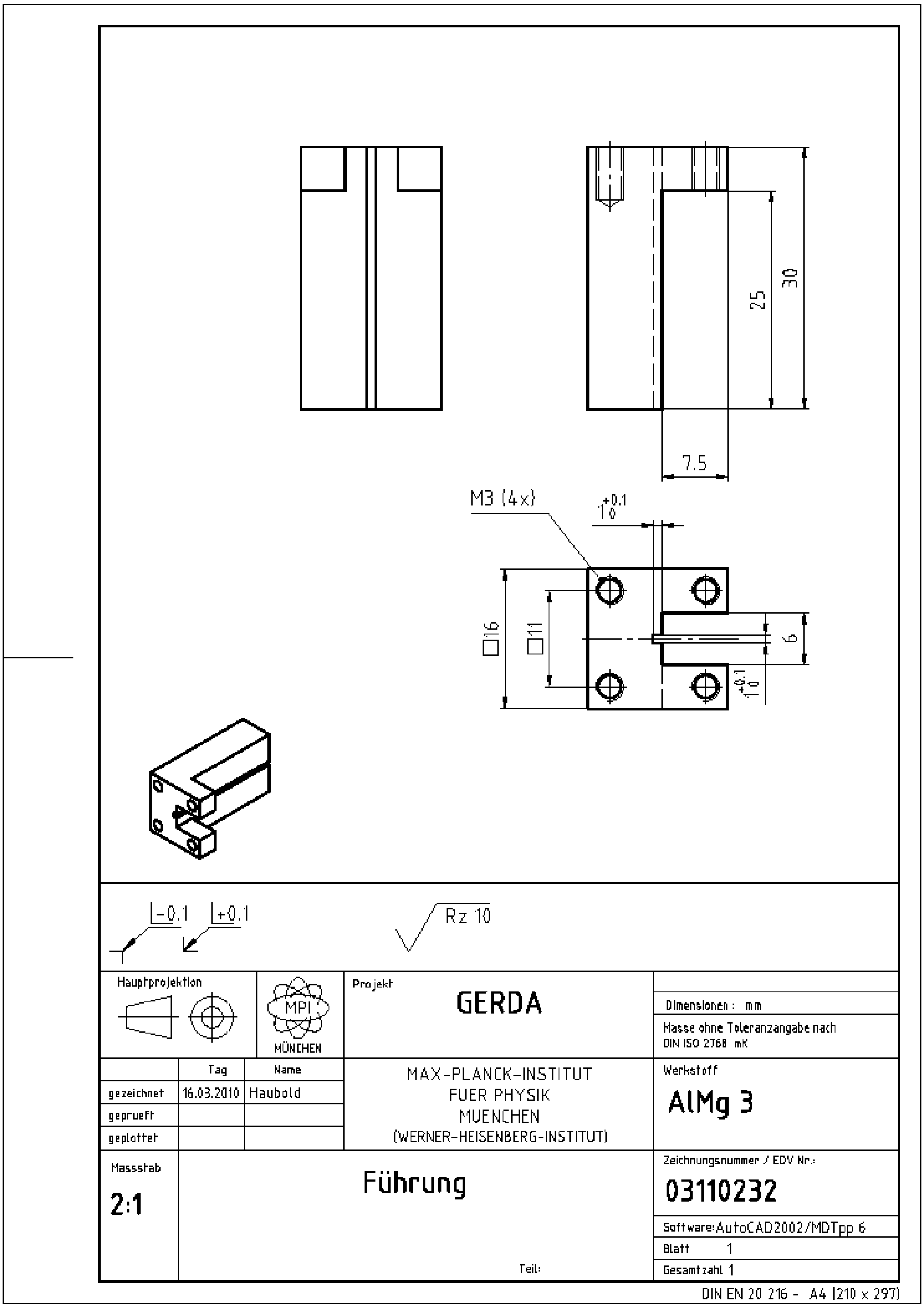

Figure 8.4: Technical drawing of the fixing guide. It fixes the WLS-fiber to the plastic block when it is glued.

Reproducibility of the coupling

In order to verify that the quality of the coupling is reproducible it was shown that the response of a SiPM in a coupling is the same before and after un- and remounting the coupling. The following measurement was performed. In a darkened room a SiPM was coupled to one end of a two meter long WLS fiber. An LED was mounted at the side of the fiber. Measurements with the LED being connected close to the SiPM and with the LED being connected far away to the SiPM were taken. The light transmitted through the fiber was measured with the SiPM being connected to an oscilloscope. The light intensity of the LED was kept constant through all measurements. Three measurements were taken subsequently without changing the setup and three measurements were taken after un- and remounting the coupling.
Fig. 8.5 shows the measured light intensities. The error was deduced from the response of the SiPMs in the same measurements but without the light source (LED switched off). No significant difference between the datasets with and without un- and remounting the coupling can be seen. It can be concluded that the reproduced couplings are of the same quality as the original one.

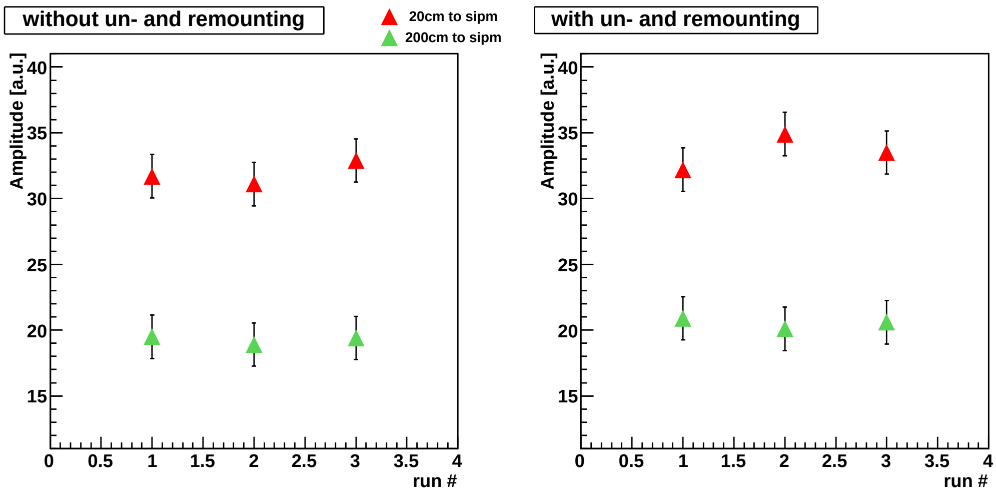

Figure 8.5: Left: Measurements done without opening the coupling before every measurement. Right: measurements done with opening the coupling. The measured light intensities are the same for both datasets.

Operation in LN

The performance of the coupling in LN and at RT was compared in a dedicated measurement. Due to the temperature dependence of the quenching resistor which leads to a different pulse shape at low temperatures (see Sec. 6.2.2), the amplitude of the response pulses could not be taken as the parameter to compare. Instead the integral of the pulse was compared. The integral of the pulse is proportional to the discharge of the SiPM which is temperature independent [21].
In a darkened room a SiPM in a coupling was illuminated with the same light source at RT and in LN. The used LEDs did not work in LN. Therefore the LED was mounted at RT and light was transmitted to the SiPM via the WLS fiber. The SiPM response to the light transmitted by WLS fiber was measured with an oscilloscope and integrated online. Measurements were performed with the coupling being submerged in LN and being at RT. The light intensity of the LED and V_{over} of the SiPM was the same at RT an in LN. The corresponding bias voltage in LN was calculated with the fit in Fig. 6.14.
In five measurements with different LED light intensities it was found that the SiPM discharges at RT and in LN agree within an error of ∼15% (see Table 8.1.2). The error was deduced form a measurement with no light source (LED being switched off). The deviation can be explained with the different pulse shapes. Further there might be a systematical error that is due to uncertainties in the calculation of the bias voltage at LN temperature.
Measurement 4 and 5 in Table 8.1.2 have been performed with the same light intensity. Between the two measurements the coupling was warmed up and cooled down to LN temperature 10 times. The measured light intensities in both measurements agree within the error. This shows that the quality of the coupling does not decrease within the first 10 cooling cycles. This number is sufficient for this work.

Table 8.1: Measured light intensities with the setup in Fig. **??** in LN and at RT.

run	discharge in LN	discharge at RT
1	(1.8±0.2)nVs	(1.6±0.2)nVs
2	(2.4±0.2)nVs	(2.6±0.2)nVs
3	(3.6±0.2)nVs	(3.6±0.2)nVs
4	(4.0±0.2)nVs	(3.6±0.2)nVs
5	(4.2±0.2)nVs	(3.7±0.2)nVs
average	(16.0n±0.45)nVs	(13.9±0.45)nVs

8.1.3 The wavelength shifting fiber

In the final experiment wavelength shifting (WLS) fiber was coiled up cylindrically along the dewar walls. SiPMs were connected to both ends. The fiber collected the light that was emitted by the TPB coated VM2000 foil and guided it to the SiPMs.
The fiber with the highest available trapping efficiency was used. The fiber is sold under the name BCF-91A by St. Gobain crystals. It consists of a scintillating core material and two claddings (see Fig. 8.6). When an UV or optical photon, interacts with the core green scintillation light (~500nm) is produced and emitted isotropically within the fiber. The absorption and emission spectra of the fiber are shown in Fig. 8.6. Scintillation light is totally reflected in the core if it falls onto the cladding under an angle of 21.5 degrees or smaller with respect to the fiber-wall. Thus, the light is guided within the fiber to the fiber-ends where it can be detected by SiPMs. In Table 8.1.3 the specification given by St. Gobain are listed.

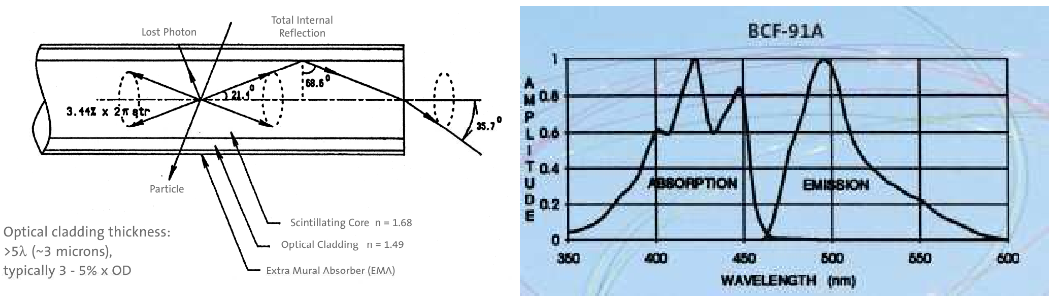

Figure 8.6: Left: Cross-section of the WLS-fiber. **Right**: Absorption and emission spectra of the WLS fiber. The fiber is made of scintillating material. When a photon deposits energy in the fiber scintillation light is produced. The scintillation light is emitted under a 4π angle. Most of the light is totally reflected at the cladding. Light is guided through the light guide by repeated total reflection. Pictures taken from [48]

Attenuation in the fiber

St. Gobain Crystals, the supplier of the used fiber, claims an attenuation length in the fiber of more than 3.4m.
To verify this claim the following measurement was performed. In a darkened room a SiPM was coupled to 2.2m of WLS fiber. In varying distances to the SiPM an UV-LED (370nm) was connected to the WLS. The light intensity at the fiber-end was measured with SiPMs being connected to the oscilloscope. The measurement was performed at RT. The light intensity was measured as a function of the distance of the LED to the SiPM (see Fig. 8.7). Each measurement point was measured six times. The values of each measurement point were averaged and normalized. The uncertainties were calculated with the central limit theorem. In order to extract the attenuation length of the scintillation light that is induced in the fiber the following function was fitted to the data:

$$C_1 \cdot e^{\frac{-x}{\lambda_1}} + C_2 \cdot e^{\frac{-x}{\lambda_2}} + \text{offset} \tag{8.1}$$

Table 8.2: Specifications of the Bicron 91A WLS fiber given by St. Gobain Crystals

Bicron 91A	
Shape	square shaped
Diameter	1mm
Density	1.05g/m
Numerical aperture	0.78
Trapping efficiency	7.4%
attenuation length	> 3.4m
Core material Core refractive index	Polystyrene 1.6
Cladding material Cladding thickness Cladding refractive index	Acrylic 4% of fiber size 1.49
Second cladding material Second cladding thickness Second cladding refractive index	Flour-acrylic 2% of fiber size 1.2

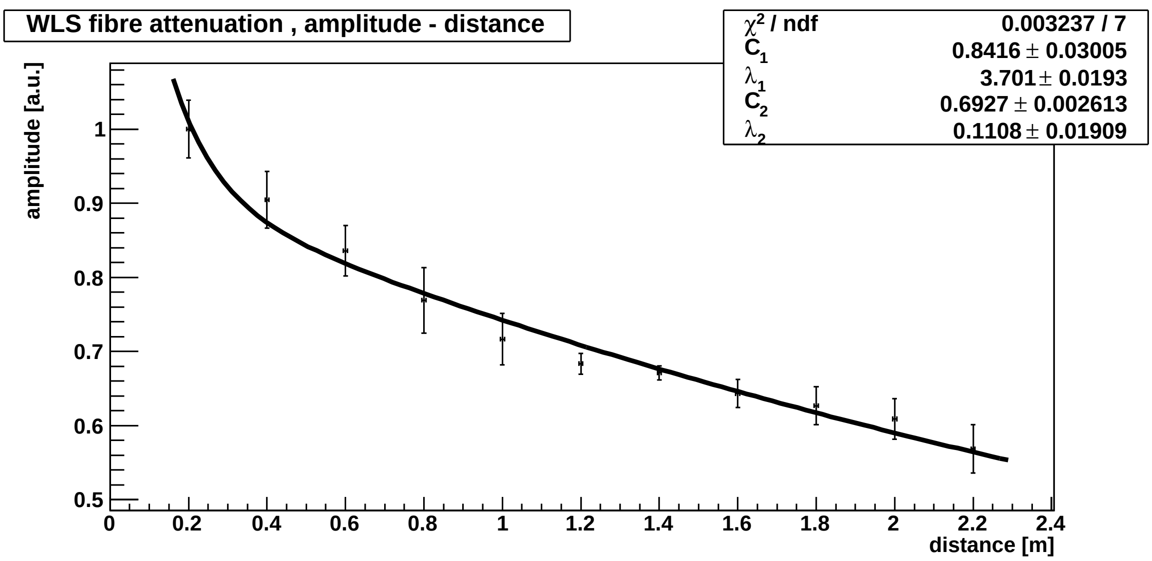

Figure 8.7: Measured attenuation of fiber at RT using an UV-LED. Two attenuation lengths were extracted. λ_1 corresponds to the attenuation of the green scintillation light, λ_2 corresponds to the UV-light of the LED.

λ_1 corresponds to the attenuation length of the green scintillation light that is produced in the fiber (~500nm). It is expected to be above 3.4m. λ_2 corresponds to the attenuation of the UV-light that is emitted by the LED (370nm) and might get trapped in the fiber as well. Because the material of the fiber is scintillating the attenuation length of the UV-light is expected to be very short. The offset was deduced from the response of the SiPM to a measurement with no light source. C_1 and C_2 take the light intensity of two

different wavelength into account. Two parameters were used because the PDE of the SiPM is slightly different for the two wavelength.
From the fit an attenuation length of (3.7±0.1)m was obtained for the green scintillation light and an attenuation length of (0.09±0.02)m for the UV-light. The attenuation length of the green light is in good agreement with the claim of St. Gobain. However it has to be noted that only ten measurement point were fitted with three free parameters.
As the used LED could not be operated in LN. The measurement of the attenuation length was not performed at LN temperature.

Losses at the fiber-end

In Fig. 8.8 the schematic cross section of the contact point of WLS fiber and SiPM is shown. The fiber has a square shaped surface of 1mm × 1mm. This is also the size of the SiPM-chip. The highest angle under which total reflection occurs in the fiber is 21.5 degrees with respect to the fiber-wall. Therefore it can be assumed that no light is emitted at the fiber-end under a bigger angel than the maximum emergent angle α=21.5 degrees. This light is emitted in form of a light cone at the fiber-end. Consequently the illuminated surface increases and the light intensity decreases with the distance. For optimal light detection it is reasonable to bring the fiber-end as close as possible to the SiPM-chip.
However the SiPM-chip is protected by a protective epoxy layer which limits the distance between the SiPM-chip and the fiber-end.

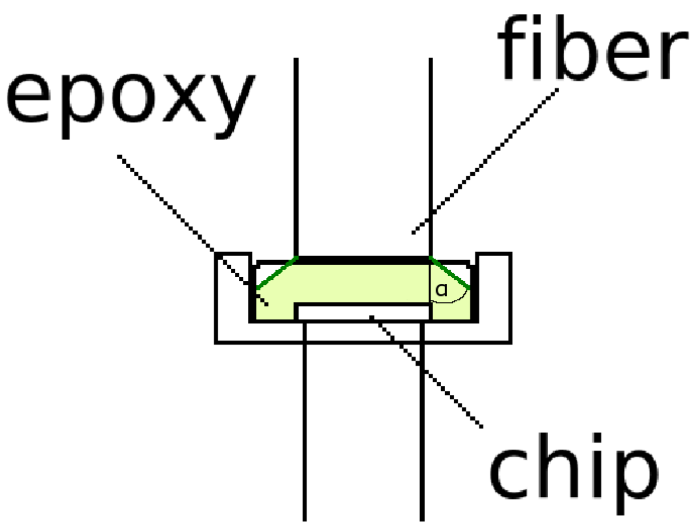

Figure 8.8: Schematics of a SiPM. The chip is protected by a protective epoxy layer. Due to this epoxy layer the WLS-fiber cannot be brought in direct contact to the chip. Light exits the fiber under a maximum angle of α=21.5 degrees. In a realistic scenario the illuminated surface is the 1.7 fold the surface of the chip.

Estimations on the light collection at the fiber-end: The light loss due to the light cone was estimated under consideration of refraction at the change over of two media. For this the thickness of the epoxy layer was estimated. A SiPM was investigated under a microscope. First the focus was put on the SiPM-chip and the position of the lens was noted. After that the lens was moved such that the focus was on the epoxy layer. The position of the lens was noted again. The relative distance of the two measured points can be regarded as an estimate for the thickness of the epoxy layer. An averaged value of (0.33 ± 0.05)mm was measured. The measurement agrees well with the used values of other groups [49]. The refraction index of the epoxy is 1.5 [50].
The illuminated surface at the distance to the SiPM-chip can thereby be calculated:

$$A = (2 \cdot \tan(\beta) \cdot d_{\mathrm{epoxy}} + 1\,\mathrm{mm})^2 \tag{8.2}$$

A = illuminated surface
d = thickness of epoxy layer-layer
β = the maximum emergent angle with respect to the fiber walls in the epoxy layer
β can be calculated with Snell's law.

An illuminated surface of 1.7mm^2 was calculated. If the surface was illuminated homogeneously, approximately 60% of the light would hit the SiPM chip. However it is evident from the properties of the WLS fiber that the intensity is the highest in the center of the illuminated surface. Thus the estimate that 60% of the light hit the SiPM is conservative.

Due to the different refraction indices of the WLS fiber and the epoxy layer the reflectivity at the change over of the two media is finite. The experience with SiPMs and optical fibers however has shown that only little light is lost due to reflections at this changeover. In a similar setup but with a larger difference between the two refraction indices a total reflectivity of 4% was measured [51]. This value will serve in the following as an upper limit.

Fiber-end preparation: Two different ways of preparing the fiber-end were tested. One is to carefully melt the fiber-end. This way the fiber forms a lens at its end. The lens could focus the emitted light of the fiber to the center of the SiPM-chip. Thus a higher photon intensity on the SiPM's chip might be achieved. In addition the heat delivers a smooth surface without any asperities.
A small gap was drilled into the plastic block so that the widened end of the fiber would fit into it. The fiber was glued into the plastic block.
The second way of preparation is to polish the fiber-end. Polishing removes roughnesses and thus arbitrary reflections. For this the fiber was first glued to the plastic block. After the glue dried and hardened the plastic block was screwed to a steel made polishing tool (see Fig. 8.9). The tool delivered stability while polishing. In its original form the plastic block was designed such that it was 0.3mm to high to fit into the optical coupling. The dimensions of the polishing tool were chosen such that the plastic block was sticking out

by 0.3mm. Thus, the polishing tool prevented the plastic block from loosing more than 0.3mm in height.
In a first step the plastic block with the fiber inside was polished with polishing papers of 3μm and 1μm granularity. After the block was shortened by 0.3mm the polishing tool was removed and the block was additionally polished with polishing paper of 0.3μm granularity but without the polishing tool. The advantage of abandoning the tool is that one gets rid off little steel grains that peel off the tool and cause scratches on the fiber. During all polishing the papers were flooded constantly with water. Thereby most grains and dirt were washed away.

Dedicated measurements were performed to compare the two techniques quantitatively. The ends of a 2 meter fiber were prepared, each with one technique. An LED was connected in the middle of the two ends and the room was darkened. With the LED being turned on the signal of the SiPMs was measured by an oscilloscope. The output of the two different ends were compared. The whole procedure was repeated six times with constant LED light intensity. After each measurement the couplings were opened and the SiPMs were exchanged. The results of the measurements are listed in Table 8.3. The error was deduced from a measurement with no light (LED being switched off). It was found that the polished fiber performs significantly better (17%) than the molten one.

Table 8.3: Light intensities for different fiber-end preparation techniques. In the runs with and without the star two different SiPM configurations have been used (exchange SiPMs).

run	molten end	polished end
1*	11.6±0.4mV	13.4±0.4mV
2	12.2±0.4mV	13.0±0.4mV
3*	10.7±0.4mV	13.3±0.4mV
4	11.3±0.4mV	12.8±0.4mV
5*	12.3±0.4mV	14.3±0.4mV
6	14.1±0.4mV	17.2±0.4mV
average	12.0±0.9mV	14.0±0.9mV

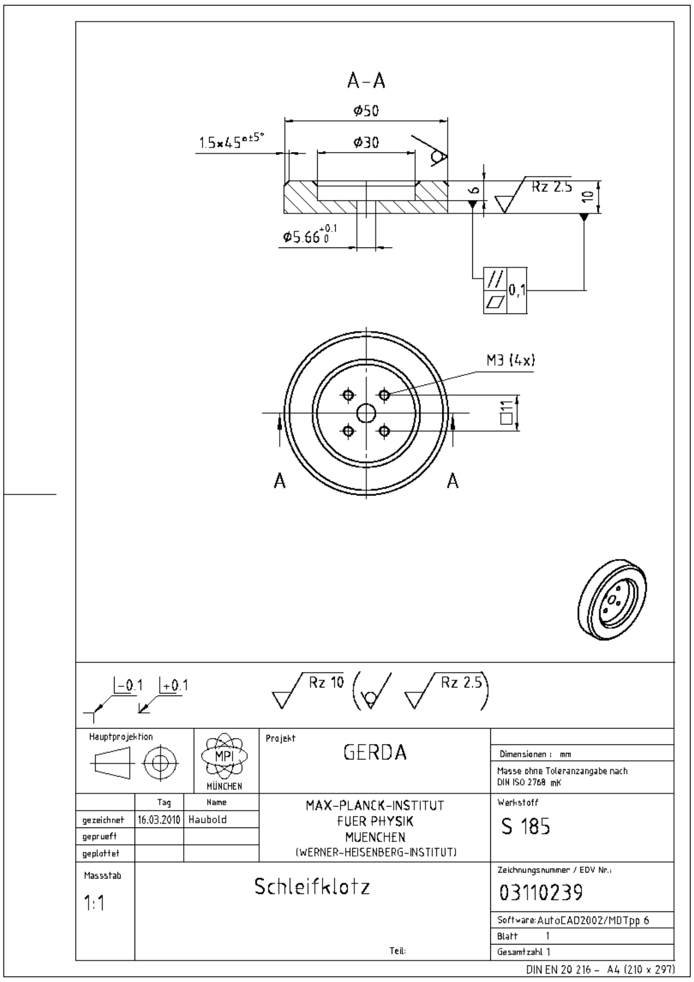

Figure 8.9: Technical drawing of the polishing tool for preparation of the fiber ends

8.2 Preliminary tests in LN

The dewar was cleaned from inside using clean tissues and ethanol. The fibers and all mechanical parts were sprayed with ethanol and dried with gaseous nitrogen. The individual parts were mounted into the dewar. In total 6 × 2.5m of WLS-fiber were connected to 12 SiPMs with each 400pixels. In Sec. 8.4 it will be explained why 2.5m long fibers were used. The available space on top of the dewar limited the number of feedthroughs and thus the number of SiPMs that could be mounted. In Sec. 6.2 it was explained that SiPM400 was used for the experiment as its PDE is superior to the PDE of the SiPM1600 and its linear range is much bigger than the linear range of the SiPM100.
In Fig. 8.10 the setup is shown. 6 SiPMs were mounted at the top and 6 at the bottom of the the Dewar. The fibers were held by an aluminum construction. All cables, couplings and other mechanical parts were covered with the TPB coated VM2000 foil. In addition the dewar wall was covered with the TPB coated VM2000 foil from inside.
The diameter of the used dewar is 24cm. Two plates were coated with VM2000 foil and inserted into the dewar such that a light cavity was formed. The active volume of the cavity was 17l.
Before the setup was put into the dewar all SiPM couplings were optimized in position. For this the lab was darkened and an LED was connected to the WLS fiber that was connected to the SiPM. The SiPM was connected to an oscilloscope and the light detection of the SiPM was monitored visually. Now the position of the WLS with respect to the SiPMs was tuned until the light detection of the SiPM was maximal. The coupling with the optimal light detection was fixed.
The dewar was closed in an air and gas tight way. Aluminum foil was wrapped around the dewar to improve the light tightness. In order to make some preliminary tests the dewar was filled with LN. Using the fit in Fig. 6.14 the bias voltage at LN temperature was calculated that equals the over voltage suggested by Hamamatsu.

Comparison of the individual channels: In order to determine whether all SiPMs and couplings are of same quality, a background measurement with a coincidence trigger on two channels was taken. The run time of the data taking was 8.5hours. The energy threshold was set to 0.5p.e. The average number of fired pixels for the individual channels was compared. In Fig. 8.11 the recorded spectra of the individual channels are shown. The average number of fired pixels was extracted from the spectra by averaging over all events. The averaged number of fired pixels is displayed in Fig. 8.12. All channels were working and detected an averaged number of of fired pixels between 5.5 and 7.5. The coincidence trigger was set on SiPM 2 and 5. This is why the number of 1 pixel events is increased for this two SiPMs. Consequently their averaged number of fired pixels is reduced. The SiPMs 1 and 2 are from a different batch. For these two SiPMs the applied bias voltage equals a different V_{over}. The averaged number of fired pixels by these two SiPMs is slightly higher.

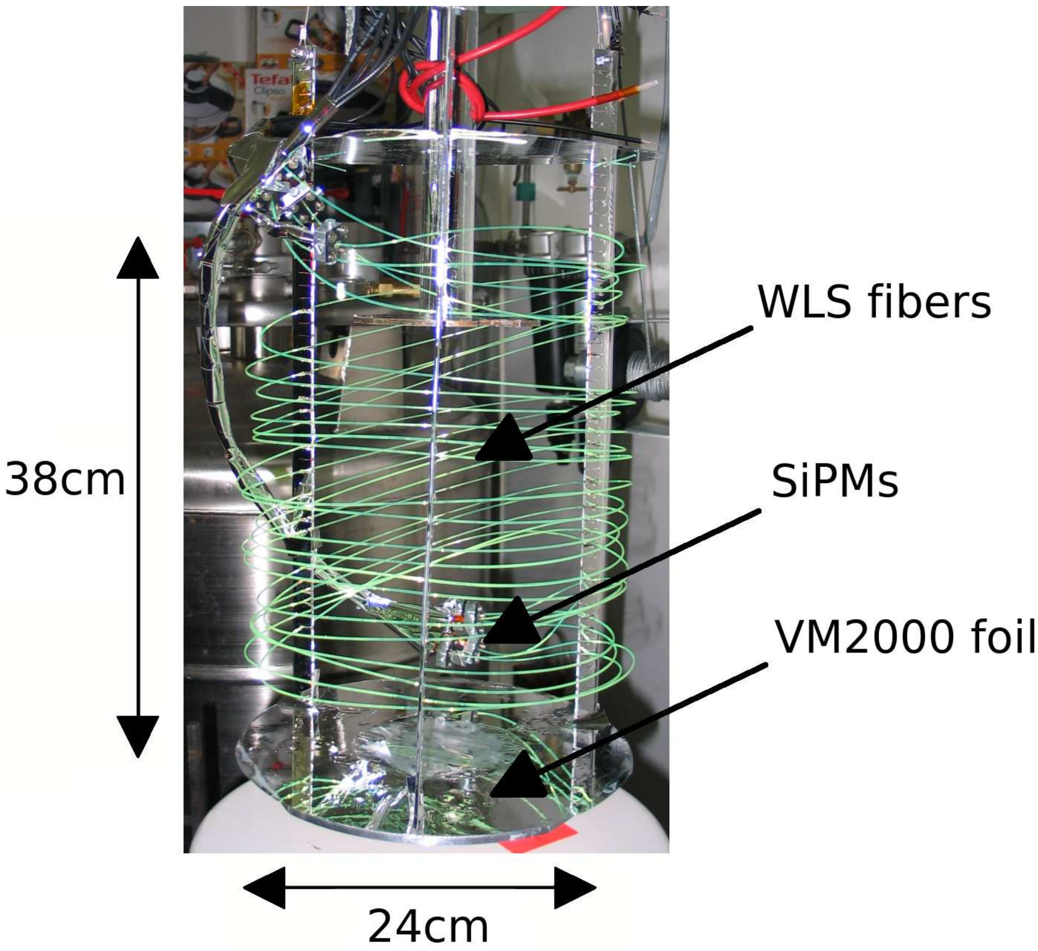

Figure 8.10: Final setup. 6 2.5m of WLS-fiber were connected to 12 SiPM of which six are mounted at top and bottom of the dewar, respectively. the active volume if the setup is about 17liters.

SiPM based LN-Čerenkov-veto The summed trigger rate of the 12 SiPMs was measured to be 6.5Hz. The error of the trigger rate is negligible. The rate can be explained with Čerenkov light that is produced in the LN by cosmic muons.
This identification is supported by comparing the expected muon rate with the total trigger rate.
The dewar has a surface of 320cm^2. One can approximate the number of cosmic muons per surface and time with 1 muon per cm^2 and minute [52]. Under the reasonable assumption that all muons are so high energetic that they produce Čerenkov light in LN a trigger rate of the setup of 5.3Hz is calculated. This value matches well with the measured one of 6.5Hz. The deviation between the calculated and the measurer rate can be explained with muons that pass the dewar horizontally and cross talk in the SiPMs.

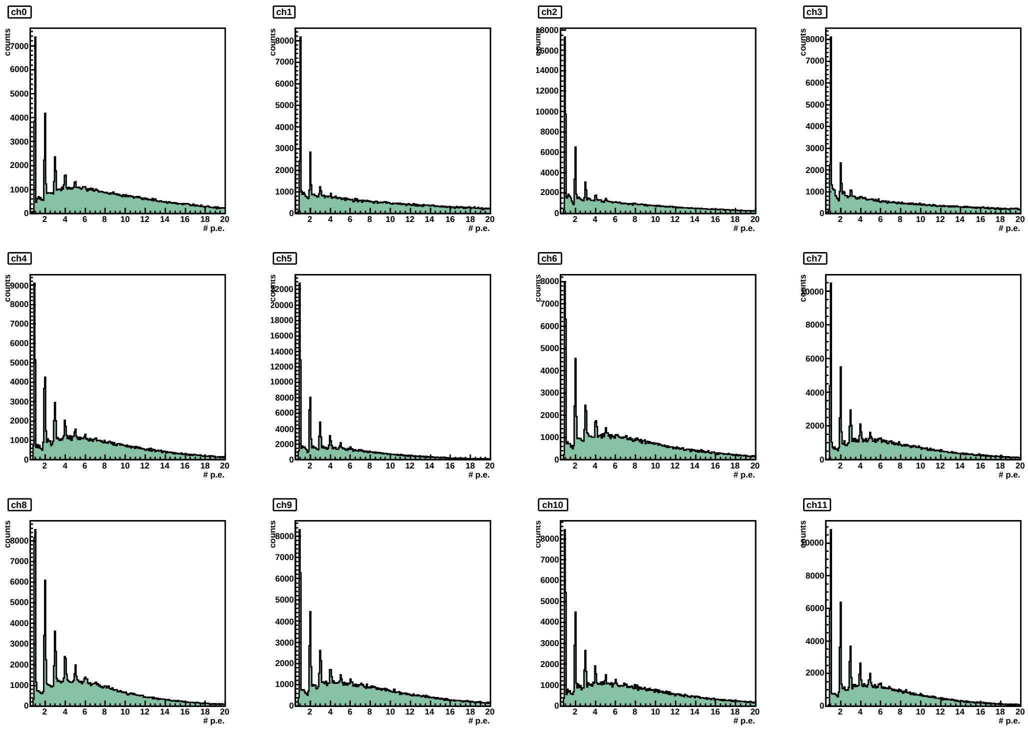

Figure 8.11: Background spectrum of the setup in LN. On the Y-axis the counts are given. The X-axis was calibrated to the number of pixels.

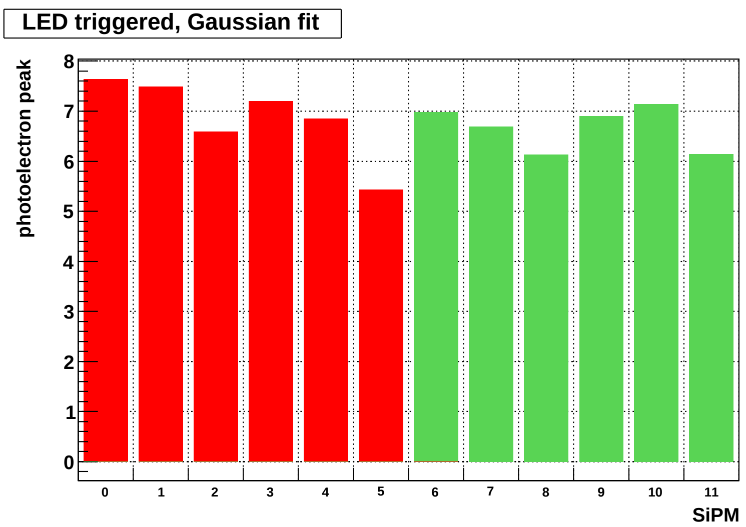

Figure 8.12: Average number of fired pixels for all SiPM in a background measurement. Red bars are used for SiPMs at the top of the dewar and green bars for ones at the bottom.

8.3 Measured light collection efficiency

Setup operated as LAr spectrometer Before filling the dewar with LAr the dewar and all mechanical parts were cleaned the same way as before. LAr [1] was filled into the dewar. It was certified to a purity of 4.6N (=99.996%). In this design the setup could be operated as a spectrometer.
Background data and the spectra of a ^{228}Th and a ^{60}Co source were recorded at three different SiPM V_{over}. An event was recorded when at least two SiPMs fired. The threshold was set to 0.5p.e. For each event a 6μs long pulse shape was recorded. The amplitudes were extracted from the pulse shapes. This was done by subtracting the value of the last 50 bins in the pulse shape from the value of the first 50 bins. Each bin had a length of 13.3ns. As we used integrating preamplifiers this method delivered the summed amplitude of all pulses within the 6μs pulse shape.
It is assumed that all SiPMs are always in the linear range. For all following statements this is a good assumption as the number of pixels firing is well below the number of total pixels for all SiPMs. Thus, the amount of detected light is proportional to the number of fired pixels (see Fig. 5.4).

In Fig. 8.13 the recorded spectra of ^{228}Th, ^{60}Co and the background are shown for three different SiPM V_{over}. All spectra have a strong signal at low light intensities in common. In the ^{228}Th and ^{60}Co spectrum enhancements are present that cannot be found in the background data.
In the ^{228}Th spectrum The characteristic bump at high light intensities corresponds to the 2.6MeV FAP (= full absorption peak). The bump in the ^{60}Co spectra results from two characteristic gamma lines that are of the energy 1332keV and 1173keV but cannot be resolved.
The resolution of the setup is not sufficient to resolve single peaks. This is because of inhomogeneous light collection efficiencies in the setup and statistical fluctuations.
Further the peak to background ratio is small. This is because LAr is a low density medium. In 4.2 it was shown that the mean free path of a 2.6MeV gamma in LAr is ~18cm. The radius of the dewar is only 12cm.
Knowing to which gamma lines these bumps correspond one can deduce the mean number of fired pixels N_{fired} per MeV energy deposit. In order to extract N_{fired} the background spectrum was subtracted from the ^{60}Co and the ^{228}Th, respectively. It was tried to fit the data with the sum of a Gaussian and an exponential function. However only the bump in the ^{288}Th spectrum could be fitted. In Fig. 8.14 the resulting spectra are shown for V_{over}=2.8V. In Table 8.4 the obtained N_{fired} per MeV energy deposit are listed for the different V_{over}=2.8V. The errors are the standard deviations of the fits. They are large because the resolution of the LAr spectrometer was not high.
N_{fired} per MeV energy deposit increases with increasing V_{over}.
In [19] it is reported that the increase of the PDE as a function of V_{over} is a saturated curve. Thus increasing V_{over} from 2.5V to 2.8V should result in a bigger increase of N_{fired}

[1] LAr bought from Westfalen [53]

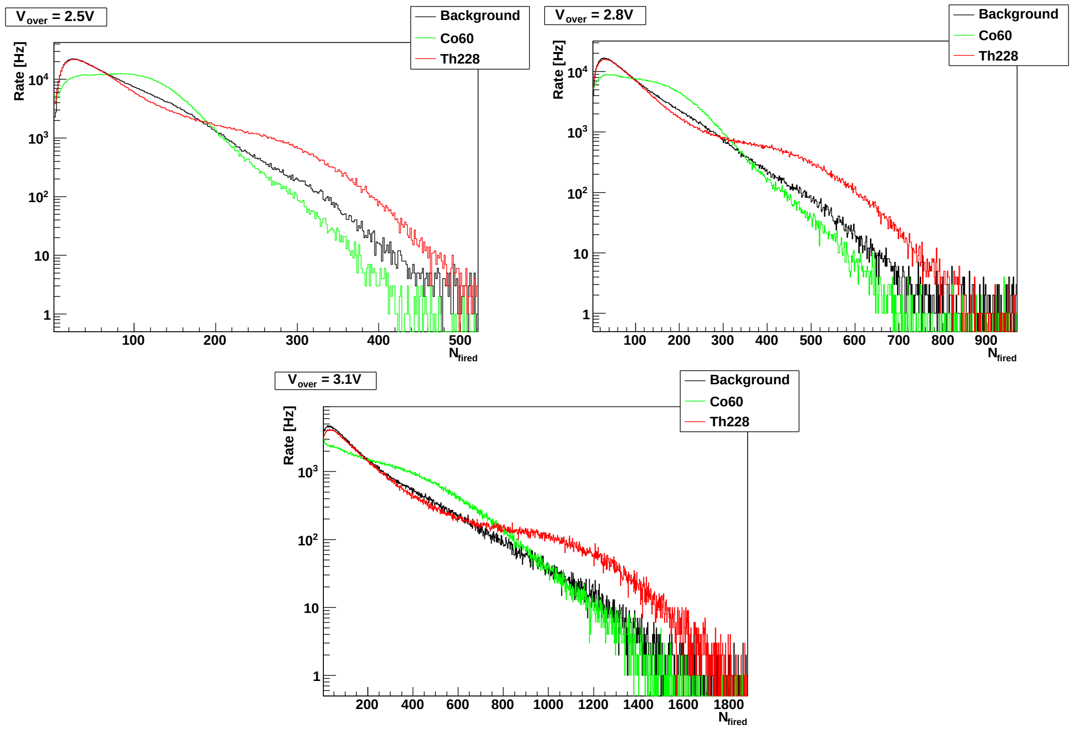

Figure 8.13: Spectra of ^{60}Co, ^{228}Th and the background for three different SiPM V_{over}. The 2614keV gamma line of ^{228}Th and the two gamma lines of ^{60}Co around 1.2MeV result in a bumps. The resolution of the spectrometer suffers form the low density of LAr.

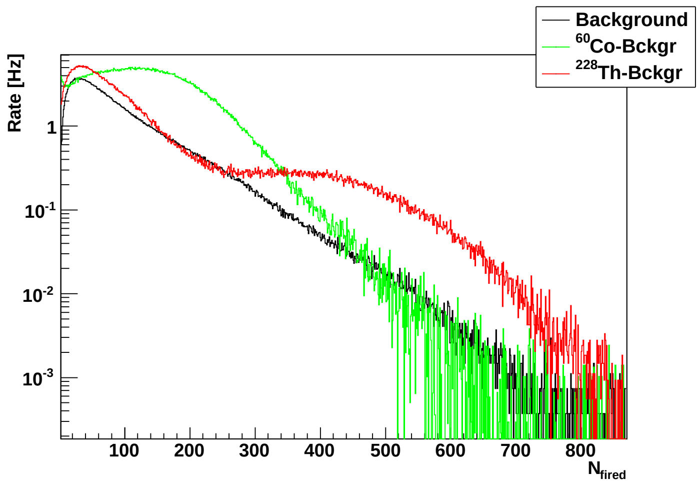

Figure 8.14: The background spectrum was subtracted from the ^{60}Co and ^{228}Th spectra. The resulting spectra were fitted with a Gaussian

than increasing V_{over} from 2.8V to 3.1V. However it is observed that increasing V_{over} from 2.8V to 3.1V results in a bigger increase of N_{fired} than increasing V_{over} from 2.5V to 2.8V. It will be shown that the increase of N_{fired} is not due to a higher number of detected photons but can rather be explained with the increase of the cross talk and afterpulse

Table 8.4: Number of fired pixels N_{fired} per MeV energy deposit received from the fit of the subtracted ^{228}Th spectrum at different SiPM over voltages.

V_{over}	2.5V	2.8V	3.1V
^{228}Th	98±20	169±31	354±96

probability with increasing V_{over} (see [30] and Sec. 6.2.5).
In chapter 6.2 a cross talk probability P_{CT} of ∼22% and an afterpulse probability P_{AP} of ∼27% was measured for the SiPM400 at V_{over}=2.8V. Neglecting fourth order effects this means that the number of detected photons per MeV energy deposit for V_{over}=2.8V can be estimated with

$$N_{photons} = \frac{N_{fired}}{1 + P_{AP} + P_{CT} + P_{CT}^2 + \ldots} \tag{8.3}$$

In this estimate all first, second and third order events that are due two afterpulses, cross talk and their combination are taken into consideration. This way the the light collection efficiency was evaluated for all three V_{over}. However this thesis lacks a measurement of the cross-talk probability at V_{over}=2.5V and V_{over}=3.1V. Therefore the corresponding cross talk probabilities were received from [54]. The calculated light collection efficiencies are listed in Table 8.5.
The errors are statistical errors. They are large and mainly due to the standard deviation of N_{fired}. The averaged light collection efficiencies are nearly the same for the measurements with V_{over}=2.8V and 3.1V. For the measurements with V_{over}=2.5V the averaged light collection efficiency is significantly less.
It can be concluded that the PDE saturates at V_{over}=2.8.

Table 8.5: Measured light collection efficiencies for different V_{over}

V_{over}	2.5V	2.8V	3.1V
P_{CT}	15%	22%	55%
P_{AP}	22%	27%	34%
LCE [p.e./MeV]	63^{+15}_{-14}	92^{+20}_{-19}	101^{+34}_{-28}

Signal shape of the scintillation light In Sec. 7.1 it was reported that LAr scintillation light consists of a fast and a slow component. The ratio of the fast component to the slow component is I_{fast}/I_{slow}=0.3.
Fig. 8.15 shows the signal shape of the scintillation light recorded with the setup. The fast and the slow component can be distinguished. However the fraction of the fast component appears smaller than reported in Sec. 7.1. There are two reasons for this. First, the decay time of the fast component is dominated by the decay time of the SiPM. Second, the time response of the setup is above the ns level. The time between production of the fast photons and the their detection is $\mathcal{O}$(100ns).

The decay time of the slow component is not dominated by the decay time of the SiPM. It was extracted from the fit of the data with an exponential function. It was found to be 830ns. In Sec. 7.1 it was reported that τ_{slow} for pure argon is 1.59μs. The deviation can be explained with N_2 contamination in the LAr. In Fig. 7.2 it is shown that a contamination of (2-4)ppm of N_2 in LAr leads to a reduction of the decay time of the slow component to 800ns-900ns.
The LAr was only certified to a purity of 99.996% meaning that a 40ppm contamination with impurities is well possible. The used argon is obtained through the liquefaction of air [53]. Thus, it is very well possible that N_2 residues remained in the LAr.

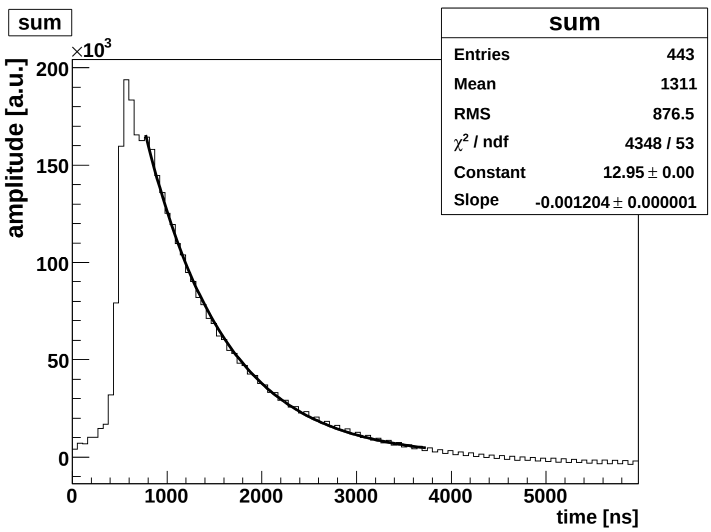

Figure 8.15: Pulse form of the scintillation light.

Assuming that the decay time of the slow component is 830ns one can calculate the quenching factor Q_F which is the ratio between the total light intensity of scintillation light emitted for a given contamination with respect to the case of pure argon. Q_F is given as

$$Q_F = \frac{I_{fast}^{N_2} + I_{slow}^{N_2}}{I_{fast} + I_{slow}} \tag{8.4}$$

It is assumed that the fast component is not quenched at all. As can be seen in Fig. 7.2 this is a good assumption for N_2-contaminations below 100ppm. Thus $I_{fast}^{N_2}$ equals I_{fast}. The ratio of I_{fast} / I_{slow} is 0.3 (see Sec. 7.1). The slow component of LAr scintillation light has a decay time of 1.5μs. Thus, I_{slow} is proportional to $\int_0^\infty e^{-t/1590\,\mathrm{ns}}\,dt$. Accordingly $I_{slow}^{N_2}$ is proportional to a factor $\int_0^\infty e^{-t/830\,\mathrm{ns}}\,dt$. Eq. 8.4 can be reduced by dividing through I_{slow}

$$Q_F = \frac{0.3 + \frac{\int_0^\infty e^{-t/830\,\mathrm{ns}}dt}{\int_0^\infty e^{-t/1590\,\mathrm{ns}}dt}}{0.3+1} = \frac{0.3 + \frac{830\,\mathrm{ns}}{1590\,\mathrm{ns}}}{0.3+1} = 0.63 \tag{8.5}$$

Thus a quenching factor of 0.63 with respect to clean LAr is expected.

8.4 Estimated light collection efficiency

In the following the light collection efficiency (LCE) of the setup will be estimated. The number of detected p.e. per energy deposit will be investigated. One important assumption will be that scintillation light is produced and distributed uniformly in the LAr volume. This assumption is reasonable because nearly all surfaces in the dewar were covered with highly reflecting mirror foils (see Eq. 8.5).
First the number of photons available to get trapped in the WLS fiber is investigated. Only photons that the coating of the mirror foil shifts to wavelengths that can be absorbed by the WLS fiber contribute to this number. The LCE will be proportional to this number. It can be given as

$$N_{photons} = Y \cdot Q_F \cdot E_F \tag{8.6}$$

Where Y is the number of primary photons per deposited energy in MeV, Q_F is the quenching factor and E_F is the flour efficiency. For pure argon Y is 41000 (see Sec. 7.3). Q_F was shown to be 0.64 (see Sec. 8.3).
E_F is the probability for the coated VM2000 foil to convert a 128nm photon into a photon that can be absorbed by the WLS fiber. The coated VM2000 foil emits light at a wavelength of about 400nm. In [55] a rate of 1.3 for the conversion of helium scintillation light into blue light was reported. This number is bigger than one because helium scintillates at a wavelength of ~80nm. A 80nm photon carries about 5 times more energy than a blue photon. This fact over-compensates losses in the fluorescence process. A 128nm photon carries only 60% of the energy of a 80nm photon. We will make the estimate that the conversion rate for argon is 60% of the conversion rate for helium thus 0.8.
In addition limited by the absorption spectrum of the fiber. The overlap of the emission spectrum of the coated VM2000 foil and the absorption spectrum of the fiber was graphically evaluated and found to be 0.5. Thus E_F can be estimated with 0.4.

Another important property of the setup is that the fibers are inside an optical cavity. Light that is not absorbed in the fiber is reflected by the mirror foil. The total light intensity on the fiber is proportional to a geometrical progression

$$I_{surf} = S + (1-S)R \cdot S + (1-S)R(1-S)R \cdot S + ... = \frac{S}{1-(1-S)R} \tag{8.7}$$

where R=95% is the reflectivity of the mirror foil and S is the ratio of the fiber surface to the reflector surface. S is a function of the fiber-length. For the used square shaped fiber S is proportional to $4 \cdot 1\,\text{mm} \cdot L$, where L is the fiber-length.
The first term in Eq. 8.7 corresponds to light that is trapped in the fiber subsequently after its production. The second term corresponds to light that reflected once at the mirror foil before it is trapped in the fiber. This term is proportional (1-S) because light that was already trapped in the first iteration has to be excluded. The description of the following terms is analogous.

The LCE will also be proportional to the light intensity at the fiber-end I_{fe}. Under the assumption that scintillation light is distributed homogeneously along the fiber. It can be written as

$$I_{fe}(L) = I_0 \frac{1}{L} \int_0^L e^{-\frac{x}{\lambda}} dx = I_0 \frac{\lambda}{L}(1 - e^{-\frac{L}{\lambda}}) \tag{8.8}$$

where I_0 is the incident light intensity on the fiber, λ=3.7m±0.1 is the attenuation length in the fiber and L is the fiber-length.
I_{surf} and I_{fe} are the only factors in the LCE that are functions of the fiber-length L. They represent two competing processes. By maximizing their product the optimal value for the fiber length can be determined. A longer fiber delivers a larger surface where light can be trapped thus I_{surf} increases. The competing process is the attenuation of light in the fiber. In long fibers the fiber ends and thus the SiPMs are on average more distant to the spot of light trapping. Consequently light is attenuated stronger before it is detected. It was found that the LCE peaks at a fiber-length of 2.5m. This is why 2.5m long fibers were used in the experiment (see Fig. 8.16).

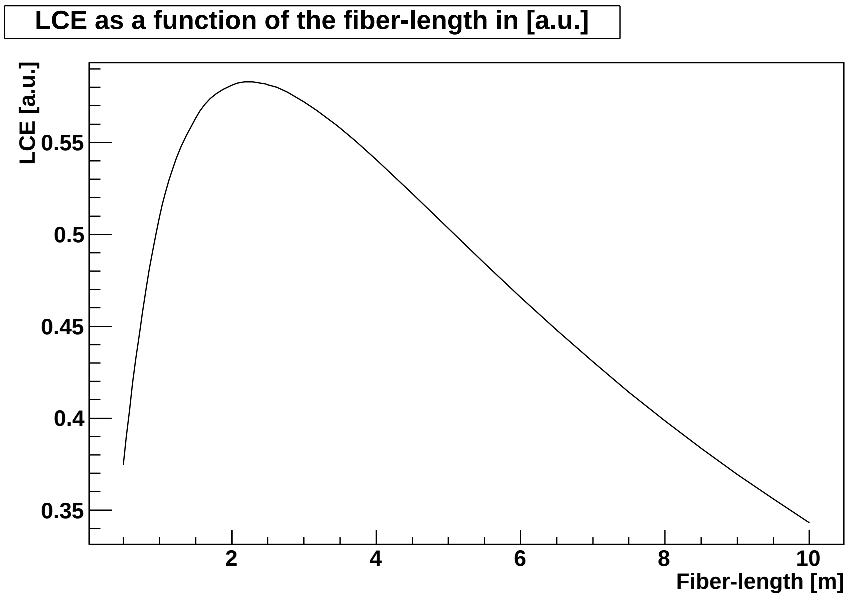

Figure 8.16: The LCE is proportional to the product of Eq. 8.7 and Eq. 8.8. This product and thus the LCE peaks at a fiber-length of 2.5m.

The total LCE in terms of detected photo electrons per energy deposit can written as follows:

$$N_{p.e.}/E_{deposit} = Y \cdot Q_F \cdot E_F \cdot \frac{S}{1-(1-S)R} \cdot I_{fe}(2.5m) \cdot E_{tr} \cdot PDE \cdot C_{OC} \cdot (1 - R_{OC}) \tag{8.9}$$

where E_{tr}=7.3% is the trapping efficiency of the fiber, PDE=25% is is the photon detection efficiency of the SiPMs, C_{OC}=0.6 is the conversion efficiency in the coupling and R_{OC}=0.04 is the reflection index between the fiber-end and the epoxy layer on the SiPM.

It is assumed that photons that hit the fiber but do not get trapped are lost.
Eq. 8.9 was evaluated for the geometry of the experiment and $N_{\text{p.e.}}/E_{\text{deposit}}$ was calculated to be

$$\mathrm{N_{p.e.}/E_{deposit}} = 122^{+47}_{-55}\ \text{p.e.}\,/\,\text{MeV} \tag{8.10}$$

Many parameters contribute to this number. Therefore calculated quantity can only be regarded as a rough estimate.
The comparison of the calculated photon detection efficiency in Eq. 8.10 with the measured photon detection efficiency in Eq. 8.3 shows that the calculation and the measurement are in good agreement.

Chapter 9

The LAr anti-Compton veto

The LAr anti-Compton veto for HPGe detectors consists of a LAr-spectrometer that is operated around the HPGe detectors.
Events in the HPGe detector that are due to the energy deposit of ionizing radiation can be identified as such if the ionizing radiation creates scintillation light in the LAr and the scintillation light is detected.
The $0\nu\beta\beta$ of ^{76}Ge is expected to be a local event meaning that energy is deposited within a small radius in the HPGe detector. The Q-value of the process is expected to be at 2039keV. For the search of the $0\nu\beta\beta$ in ^{76}Ge one of the most dangerous background events are gammas that deposit energy around 2039keV in the HPGe detector. Gammas in this energy range most probably interact with the germanium via Compton scattering. Segmented HPGe detectors can identify multiple Compton scattered events as background. If singly Compton scattered gamma escapes detector no identification as background is possible. Detecting the scintillation light in the LAr that a singly Compton scattered gamma produces enables the identification of these events (see e In Fig. 9.1).
Although the resolution of our setup was limited it performed well as a LAr anti-Compton veto for a HPGe detector. In this chapter the performance of the Setup as an LAr anti-Compton veto is described.

9.1 Setup and system response

The same setup as in Fig. 8.1 was used. In addition a HPGe detector, made by DSG Detector Systems GmbH, was inserted into the dewar. The detector is p-type with a true coaxial geometry. The hight is 70mm. The outer and inner radius are 75mm and 10mm, respectively. The detector has a six-fold segmentation in the azimuth angle. The detector was operated at 2500V. The depletion voltage is about 2000V. The detector had been damaged in the past and had a leakage current of about 6nA. The best resolution achieved was a full width half maximum (FWHM) of 15keV at about 1332.5keV on the core and slightly better on the segments (see Table 9.1). Nevertheless the resolution is sufficient for a proof of concept experiment. The detector was positioned in the middle

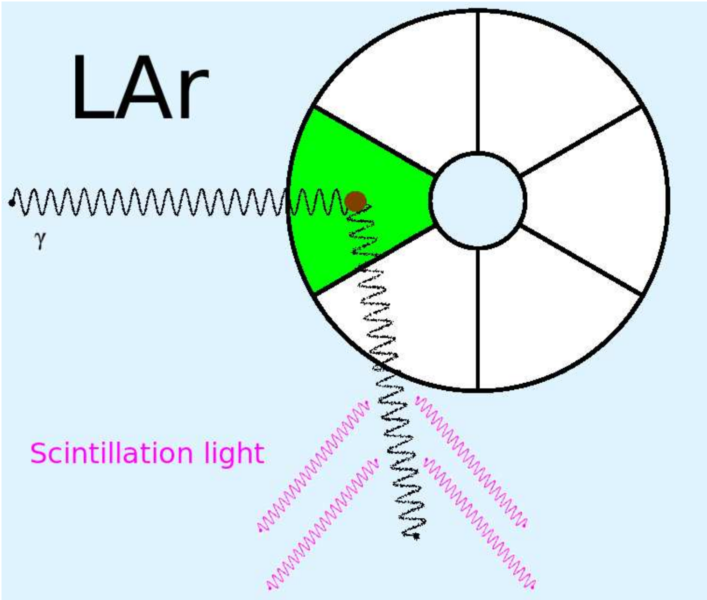

Figure 9.1: Schematic drawing of a gamma that singly Compton-scatters in the HPGe detector and produces afterwards scintillation light in the LAr.

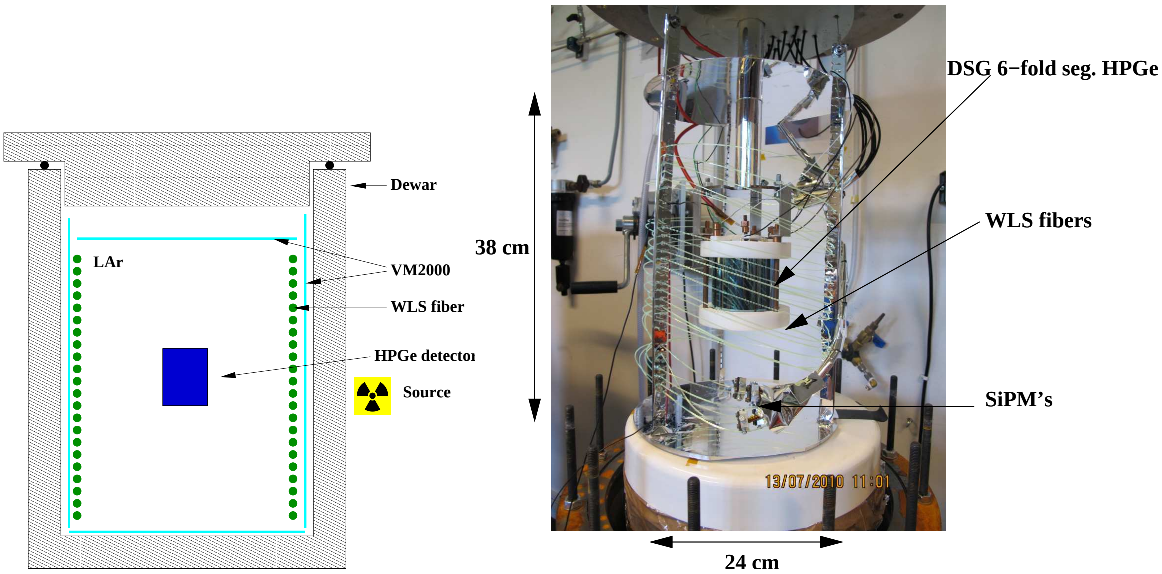

Figure 9.2: **Left:** Schematic drawing of the setup. An Al frame holds 6 × 2.5m of WLS fibers. 12 SiPMs are connected to the fiber-ends with home made couplers. The HPGe detector is mounted in the center. The whole structure is lowered into the LAr filled dewar. The dewar's walls are covered with TPB coated VM2000 foil. **Right:** Practical realization of the setup.

of the system with the WLS fibers being coiled around it. The dewar was filled with 4.6N LAr.
The detector itself could not be covered with VM2000 foil because its surface is too sensitive. The holder of the detector is made of Teflon. It could not be covered with

mirror foil neither because the mirror foil does not stick to it. However Teflon has a very high reflectivity. In the experiment photons were absorbed at these surfaces. Therefore the collection efficiency of the LAr scintillation light of this setup was worse than of the setup without the HPGe detector.

The schematics and a picture of the setup are shown in 9.2. The HPGe detector as well as the SiPMs were amplified by charge sensitive preamplifiers and connected to the DAQ (for specifications see Sec. 6.2). The DAQ was triggered on the core signal of the HPGe detector. The threshold was set on 800keV. Pulse shape data was recorded simultaneously for all 19 channels (HPGe core + 6 segments + 12 SiPMs). 6μs long pulses were recorded for all channels with a sampling rate of 13.3ns. The rise time of the preamplifers is 6ns.

Three datasets were taken with a 20.5kBq ^{228}Th source that was taped to the dewar wall from outside. The datasets only differed in the SiPM V_{over}. The applied V_{over} were 2.5V, 2.8V and 3.1V. High V_{over} was chosen to maximize the PDE. All three datasets consisted of 2.56 $\cdot 10^6$ events. The count rate in the detector was ~58Hz in all measurements.

The amplitude of the HPGe core and segments was given by the trapezoidal energy filter of the DAQ System [56]. The amplitude of the SiPMs was extracted from the pulse shaped in the same way as in the previous setup.

Table 9.1: FWHM of the distinct peaks in ^{228}Th spectrum in keV.

channel	2.6MeV FAP	1.6MeV FAP	DEP	1.4MeV ^{40}K FAP
core	16.3±0.0	15.6±0.3	15.9±0.3	14.4±0.1
Seg 1	6.6±0.0	5.9±0.0	6.5±0.0	5.6±0.0
Seg 2	10.1±0.0	11.1±0.7	9.9±0.1	8.0±0.3
Seg 3	8.1±0.0	8.7±0.6	8.3±0.1	7.0±0.3
Seg 4	11.6±0.1	12.9±1.5	11.6±0.3	10.7±0.3
Seg 5	10.8±0.1	11.8±2.2	11.4±0.3	9.2±0.2
Seg 6	9.7±0.1	9.7±0.9	9.6±0.2	8.8±0.2

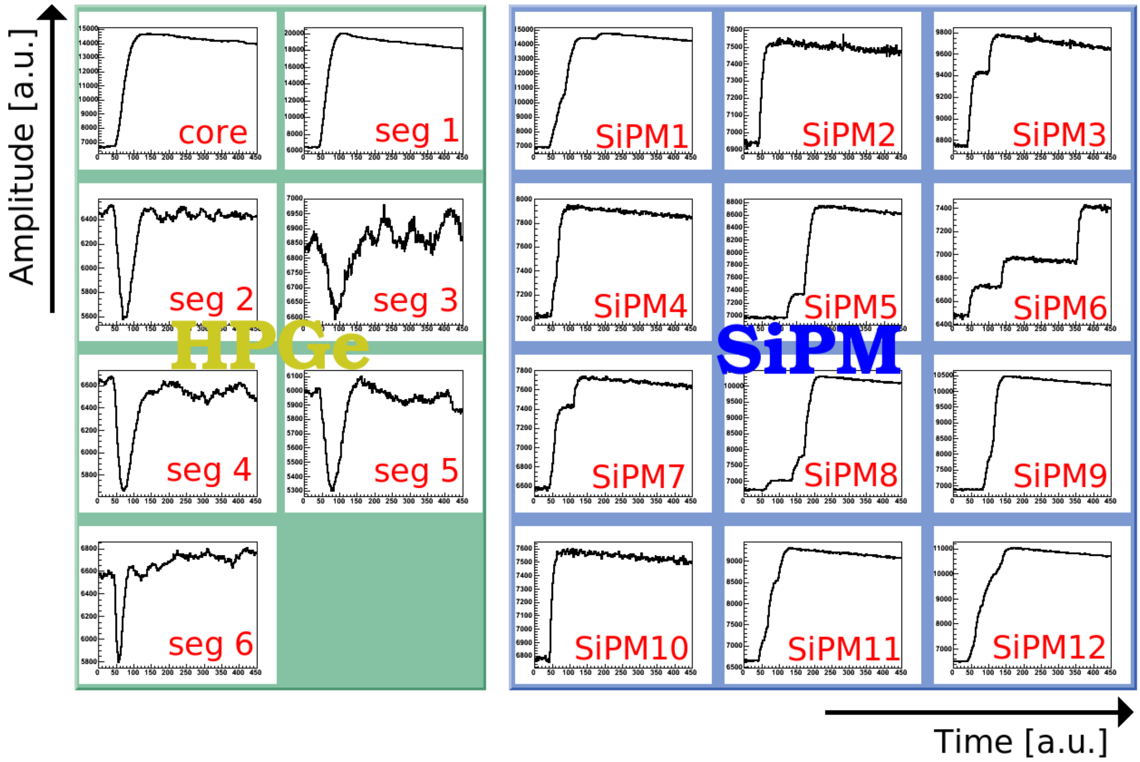

Figure 9.3: Pulse shapes for a typical event. The pulses in the two first columns correspond to the HPGe detector. The upper left pulse is the core channel. The six following pulses correspond to the segments. On the right side the 12 SiPM pulses are shown.

In Fig. 9.3 pulses of the core, all HPGe detector segments and all SiPMs for a typical single segment event are shown. The same energy deposition within the resolution can be seen in the core and segment 1. No energy was deposited in the other segments. The other segments only see mirror charges and no real energy deposition. Simultaneously all SiPMs detect a signal. This means that energy was deposited coincidently in the LAr and the HPGe detector. The event is thus most probably due to a gamma that singly Compton scattered in the HPGe detector and subsequently deposited some of its remaining energy in the LAr. In a GERDA like experiment this event could thus be rejected as background.

9.2 Anti-coincidence and coincidence cut

The analysis was divided into two parts. In a first part anti-coincidence between the signal in the LAr and in the germanium detector was required. In a GERDA like setup one would apply this kind of veto in order to suppress the Compton background in the HPGe detector. In a second part coincidence between the HPGe and the LAr signal was required. This was done to confirm the logical consistency of the analysis.

The veto was applied off line. It was required that the amplitude of at least one of the SiPMs exceeds a certain threshold within a time window of 6μs after the trigger. Different thresholds between 0.5p.e. and 1.5p.e were set. The threshold was set for each individual SiPM and not for the sum of the SiPMs amplitudes.

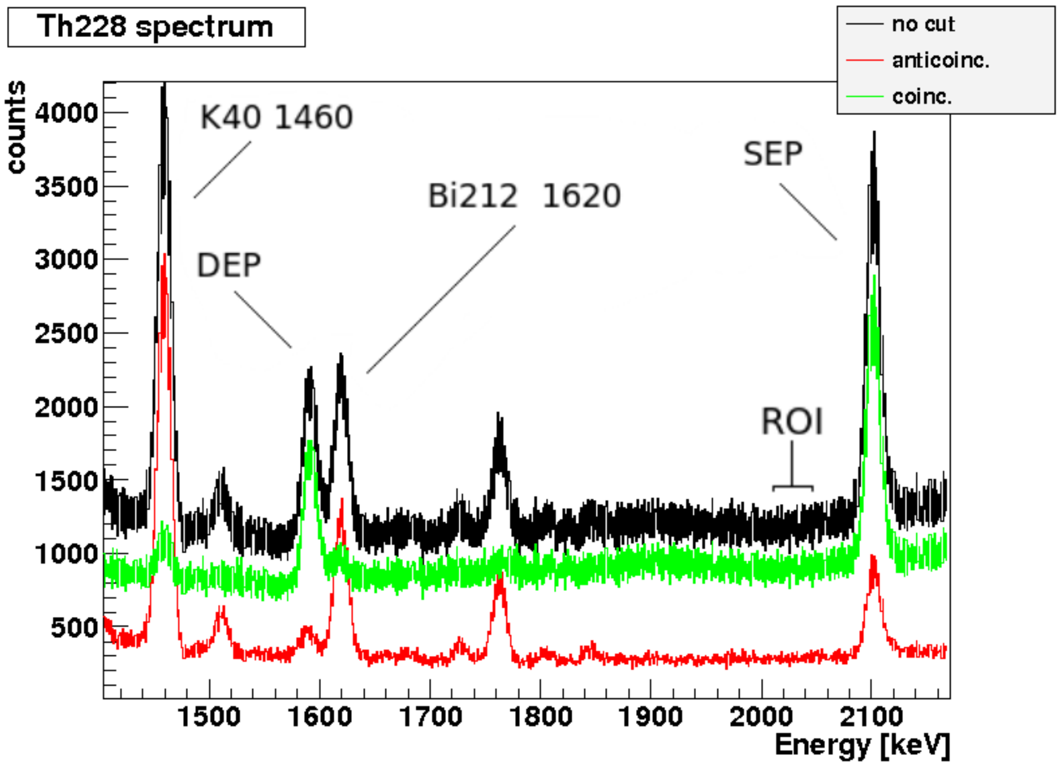

Figure 9.4: ^{228}Th spectrum with anti-coincidence and coincidence cut. For both cuts a threshold of 0.5p.e. was applied.

In Fig. 9.4 a ^{228}Th spectrum under application of anti-coincidence and coincidence cut is shown. The energy veto was used with an energy threshold of 0.5p.e.

Anti-coincidence (AC) Using the AC cut the single and the double escape peak are suppressed significantly. This is because in both cases gammas are emitted from the germanium detector. These gammas can produce scintillation light in the LAr which can then be used to identify such an event as background. The DEP is typically suppressed stronger than the SEP. This is because an event under the DEP comes together with two

511keV gammas an event under the SEP comes only with one.
As explained in Sec. 4.4 events in the ROI are typically due to gammas that Compton scattered in the HPGe detector and escaped again. The escaping gamma typically has an energy of ∼600keV. Gammas of these energy have a mean free path in LAr of ∼9.5cm (see Fig. 4.3 in Sec 4.2). The used dewar has a radius of 12cm and the HPGe detector of 3.75cm. It is thus likely that the escaping gammas interact with the LAr producing scintillation light allowing identification as background.
FAPs as the one at 1620keV which is due to the decay ^{212}Bi deposit their entire energy within the germanium detector. No energy is deposited in the LAr. Therefore they are not expected to be suppressed by the AC cut. However FAPs are often slightly suppressed. This can be explained with that fact that the gamma line results from a decay that is part of a cascade. Gammas that are due to other decays in these cascades deposit energy in the LAr as well. The decay of ^{40}K however is unlikely to come in coincidence with other decays [57]. This is why the corresponding peak is expected to be suppressed less.

Coincidence (CC) With the analog argumentation to the one above one can explain why the SEP and the DEP are not suppressed by the coincidence cut but the FAPs are.
The coincidence cut does not suppress the ROI as much as the AC cut does. Events in this region are mostly Compton scattered gammas (see Sec. 4.4). Only gammas that do not interact with the LAr after depositing energy in the HPGe detector are suppressed by the coincidence cut. The mean free path of these gammas is typically larger than the LAr layer that is penetrated. Thus only the minority of the events in the ROI is suppressed.

9.3 Tuning parameters

In order to find out the optimal parameters the suppression factor (SF) of the region of interest for the $0\nu\beta\beta$ (ROI) and the SFs of three peaks were investigated under different veto conditions. The three peaks under study were the double escape peak at 1592keV (DEP), the full absorption peak that is due to the decay of ^{212}Bi and at 1620keV (Bi212) and the 1460keV peak which is due to the decay of ^{K40}K (K40).
The SFs of the peaks are given by the ratio of events below the corresponding peak before and after the cut. In order to receive the number of events below a peak the histogram was fitted with the sum of a linear function and a Gaussian in the corresponding region. The histogram itself and the linear function were integrated within the one sigma region of the Gaussian. The number of events below the peak is given by the difference between the two integrals. A SF of 4 means that 25% of the events survived the cut. Accordingly 75% were successfully identified as a certain type of event.
The error bars in the following plots are all due to statistical errors. The statistical error of the number of events under the peaks was propagated into the error of the SF.

Adjusting V_{over}: Cross talk and the afterpulse probability, as well as the PDE increases with V_{over} [19]. However for the practical use in a veto system the cross talk and afterpulse probability of the SiPM are much less important than the PDE.
To be sure that the SiPM are operated with the highest possible PDE, data was recorded with three different SiPM V_{over}. Table 9.3 shows the SFs of the DEP, Bi212, SEP, ROI and the K40-peak as a function of the V_{over} of the SiPMs. Although 2.5 V is already a high V_{over} the SFs are still increasing until when V_{over} is increased to 2.8V. Increasing the V_{over} from 2.8V to 3.1V however does not lead to higher SFs. The calculation in Table 8.5 is thus verified. The increase of N_{pix} is mostly due to an increased cross talk and afterpulse probability and not due to a higher number of detected photons. Since increasing the SiPM V_{over} beyond 2.8V did not result in a further increase of the veto efficiency it can be concluded that the PDE saturated.
For further analysis V_{over}=2.8V was used.

Table 9.2: SFs as a function of the V_{over} of the SiPMs using the energy veto with a threshold = 0.5p.e.

V_{over}	2.5 V	2.8 V	3.1 V
DEP	5.89±0.08	6.21±0.09	6.18±0.09
Bi212	1.15±0.02	1.16±0.01	1.15±0.02
SEP	3.76±0.03	3.79±0.03	3.84±0.04
ROI	4.10±0.02	4.15±0.03	4.17±0.03
K40	1.11±0.01	1.10±0.01	1.12±0.01

Adjusting the photon detection threshold: In Table 9.3 the achieved SFs of the peaks as a function of the set photon detection threshold are shown. Increasing the photon detection threshold reduces the number of random triggers and thus increases the signal efficiency.
The K40 is not supposed to be suppressed by an LAr anti-Compton cut. Thus reciprocal of the SF of the K40 can be regarded as a measure of the signal efficiency. Increasing the photon detection threshold from 0.5p.e. to 1.5p.e. increased the reciprocal of the SF of the K40 only from 92% to 93%. This increase is small. Thus, it was decided to set the photon detection threshold to 0.5p.e. for the further analysis.

Table 9.3: SFs achieved with the energy filter using a 0.5 p.e. threshold, anti-coincidence cut

E_{THRESH}	0.5.	0.8	1.0	1.2	1.5
DEP	6.21±0.09	6.19±0.09	5.87±0.08	5.59±0.08	5.41±0.08
Bi212	1.16±0.01	1.15±0.01	1.15±0.01	1.14±0.02	1.13±0.01
SEP	3.79±0.03	3.74±0.03	3.6 ±0.03	3.47±0.03	3.38±0.03
ROI	4.15±0.03	4.09±0.02	3.93±0.02	3.77±0.02	3.67±0.02
K40	1.10±0.01	1.1 ±0.01	1.09±0.01	1.09±0.01	1.09±0.01

9.4 Veto efficiency as function of coincidence window

In order to study the veto efficiency as a function of the coincidence window a trigger veto was introduced. For this veto it was required that at least one SiPM fired within a given time window after the trigger. The veto efficiency with this method was studied for different time windows. In the following this veto will be referred to as trigger veto. The trigger veto was applied off line. Fig. 9.5 shows SFs achieved with the trigger veto as a

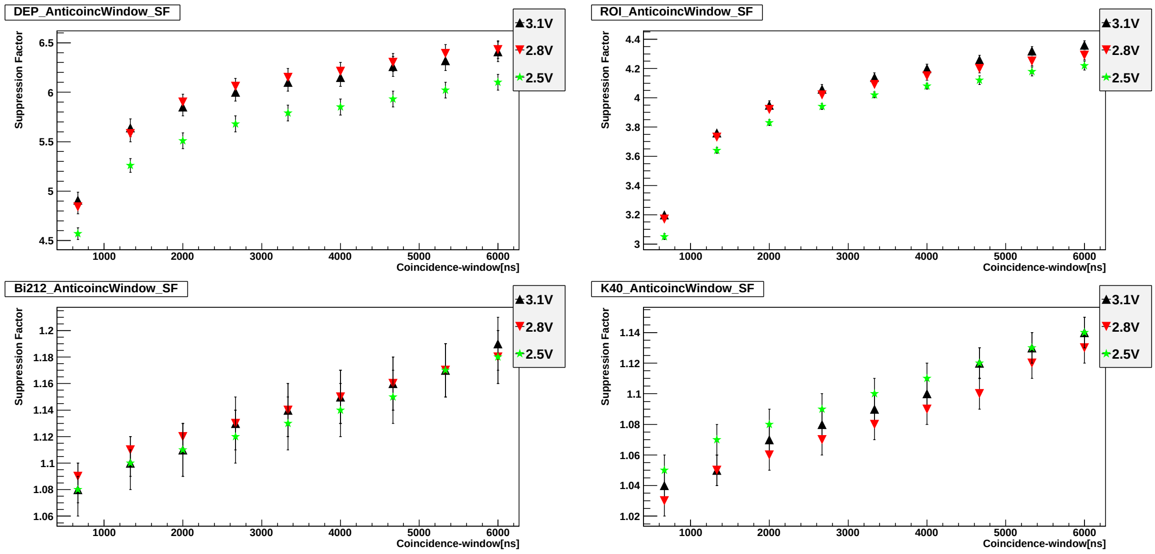

Figure 9.5: SFs of distinct peaks and the ROI as a function of the coincidence window. V_{over}=2.8V

function of the coincidence window. Coincidence windows between 667ns and 6μs were studied. The calculation was done for three different SiPM V_{over} (2.5V, 2.8V and 3.1V).
As expected the SFs increase with increasing coincidence windows. The increase of the SFs of the DEP and the ROI is stronger for small coincidence windows (> 2μ s). At a window length of 2μs-2.5μs the increase flattens. From this point on the SF increases linearly with increasing coincidence window.
The same behavior is observed for the Bi212. However the SFs are significantly smaller.
The SFs K40 is small (SF = 1.03-1.13) and increases linearly with increasing V_{over} over the whole the range.
These observations can be explained as follows: The strong increase of the SF of the DEP and the ROI for the coincidence window being increased from 667ns to 2.7μs is due to the slow component of the scintillation light (see Sec 7.1). The decay time of the slow component is $\mathcal{O}(\mu s)$. Therefore scintillation light is produced even microseconds after the trigger.
After 2.7μs no scintillation light is collected anymore. From this point on any increase of the of the SFs is due to background events (cosmic muons or external radiation). At this point afterpulses can be neglected as their time scale is $\mathcal{O}$(ns) [21].
The K40 is not expected to be suppressed at all because in the corresponding events no energy is deposited in the LAr. Thus, any increase of its SF must be due to background

Table 9.4: anti-coincidence cut, trigger veto, V_{over}=2.8V: SFs as a function of the coincidence window. An event is vetoed if at least one channel fires within the required coincidence window. The errors of the individual SF are marked with a Δ.

c.-window	0.67μs	1.33μs	2.00μs	2.67μs	3.33μs	4.00μs	4.67μs	5.33μs	6.00μs
DEP	4.70±0.08	5.31±0.09	5.57±0.09	5.66±0.09	5.69±0.10	5.70±0.10	5.73±0.10	5.71±0.10	5.69±0.09
Bi212	1.06±0.01	1.06±0.01	1.06±0.01	1.06±0.01	1.06±0.02	1.06±0.02	1.05±0.02	1.04±0.02	1.04±0.02
ROI	3.08±0.04	3.55±0.04	3.70±0.04	3.76±0.04	3.79±0.04	3.81±0.04	3.82±0.04	3.79±0.04	3.80±0.04

events. The slope of the increase is stable over the whole range because the probability of a background event is independent from the trigger and constant in time.
In order to correct for the random veto that is due to background effects all SFs were normalized to the SF for the K40.
The normalized SF as a function of the coincidence window are presented in Fig. 9.6 and in Table 9.4. The plots of the DEP and the ROI flatten out completely at a coincidence window of 2.7μs. From this point on the veto efficiency does not increase with increasing coincidence windows. This means that 2.7μs after the trigger no scintillation photons from the incident gamma are detected. As no scintillation light is measured later than 2.7μ s after the trigger it is evident that the slow component in the experiment must be quenched. This can be caused by N_2 contamination as explained in Sec. 7.3.
In Fig. 9.7 the calculated amplitudes of the slow component for the decay times τ=830ns and τ=1.59μs are shown. From the comparison of the calculated amplitude for τ=1.59μ s with Fig. 9.6 after $\sim$3μs, it is evident that the decay time of the slow component must be smaller than 1.59μ s. The amplitude of a slow component with τ= 830ns matches well with the results received from Fig. 9.6. Both imply that nearly no scintillation light is produced later than 2.7μs after the trigger.
The normalized Bi212 SFs are nearly unity over the whole range. This is in good agreement with the expectation. The deviation from one is due to secondary gammas that come in coincidence and produce scintillation light in the LAr.
In the further analysis a coincidence window of 6μ s was used. From Fig. 9.6 it is evident that all LAr scintillation light is collected using a 6μ s coincidence window.

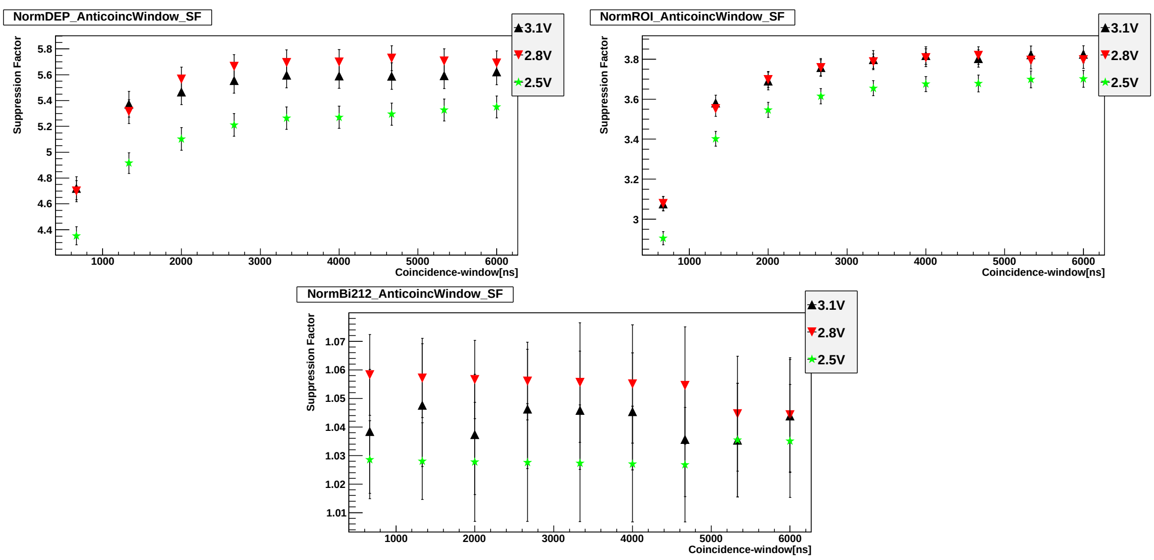

Figure 9.6: SFs of distinct peaks and the ROI as a function of the coincidence window. The SFs are normalized to the SF of the K40. V_{over}=2.8V

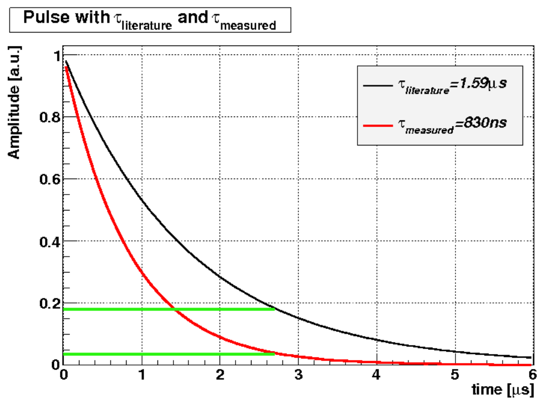

Figure 9.7: Slow component with decay time $\tau = 1.59\mu s$ and $\tau = 830ns$. After 2.67μ s the amplitude of the scintillation light should be negligible. This is only true if the decay time of the slow component is significantly smaller than 1.59μ s.

Table 9.5: anti-coincidence cut, trigger veto, V_{over}=2.8V: SFs as a function of the coincidence window. An event is vetoed if at least one channel fires within the required coincidence window. The errors of the individual SF are marked with a Δ.

c.-window	0.67μs	1.33μs	2.00μs	2.67μs	3.33μs	4.00μs	4.67μs	5.33μs	6.00μs
DEP	4.84±0.07	5.58±0.08	5.90±0.08	6.06±0.08	6.15±0.09	6.21±0.09	6.30±0.09	6.39±0.09	6.43±0.09
Bi212	1.09±0.01	1.11±0.01	1.12±0.01	1.13±0.01	1.14±0.02	1.15±0.02	1.16±0.02	1.17±0.02	1.18±0.02
ROI	3.17±0.02	3.73±0.02	3.92±0.02	4.02±0.02	4.09±0.02	4.15±0.03	4.20±0.03	4.25±0.03	4.29±0.03
K40	1.03±0.01	1.05±0.01	1.06±0.01	1.07±0.01	1.08±0.01	1.09±0.01	1.10±0.01	1.12±0.01	1.13±0.01

Coincidence analysis In the following the analysis requiring coincidence between the HPGe detector and the SiPM channels is presented. It was mainly performed to verify the logical consistency of the entire analysis.

Table 9.6: coincidence cut: SFs as a function of V_{over} of the SiPMs using the energy veto with a threshold = 0.5p.e.

V_{over}	2.5 V	2.8 V	3.1 V
DEP	1.20±0.02	1.19±0.02	1.19±0.02
Bi212	7.64±0.10	7.60±0.09	7.56±0.11
SEP	1.36±0.01	1.36±0.01	1.35±0.01
ROI	1.32±0.00	1.32±0.00	1.32±0.00
K40	10.4±0.07	10.2±0.08	9.53±0.08

Table 9.6 shows the achieved SF of the DEP, Bi212, SEP, ROI and K40 as a function of the V_{over} under requirement of coincidence. An event was vetoed if SiPM channel did not detect energy deposit above a threshold of 0.5p.e. within a coincidence window of 6μs after the HPGe detector triggered. As expected the Bi212 and the K40 are suppressed stronger than the other peaks. With increasing coincidence window the SF the peaks decreases because the probability of a random trigger that is e.g. due to cosmic muons or external radiation increases.

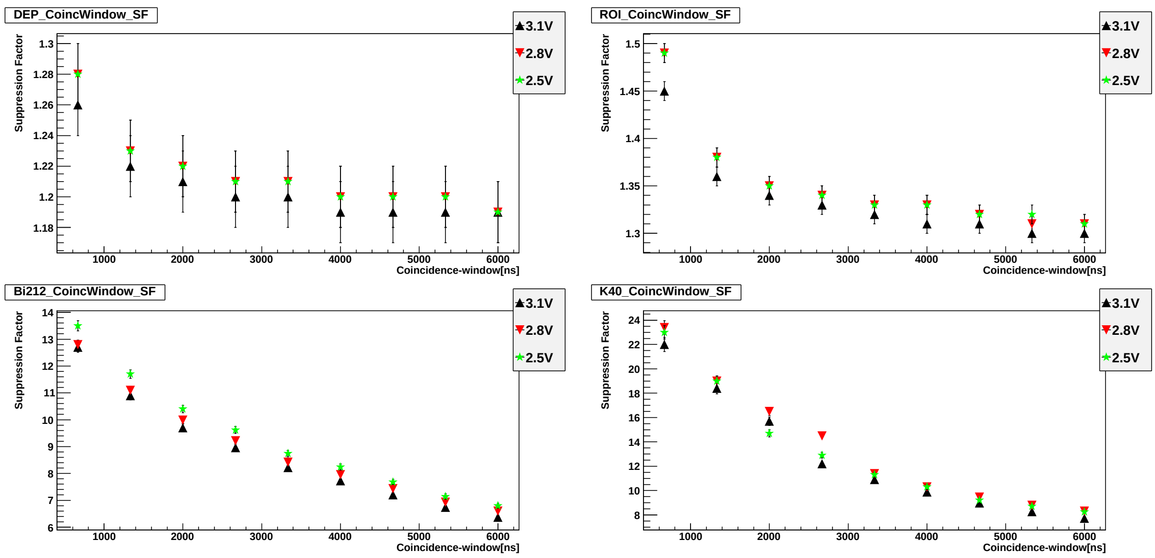

Figure 9.8: coincidence cut: Trigger veto, normalized SF as a function of the coincidence window, V_{over}=2.8V

In Fig. 9.8 and in Table 9.7 the suppression achieved with the trigger veto as a function of the coincidence window is presented. All SF decrease with increasing coincidence window. This is because the probability of a random trigger that can be caused by cosmic muons or external radiation increases with increasing coincidence windows.

Table 9.7: coincidence cut, trigger veto, V_{over}=2.8V: SFs as a function of the coincidence window. An event is vetoed if no channel fires within the required coincidence window. The errors of the individual SF are marked with a Δ.

c.-window	0.67μs	1.33μs	2.00μs	2.67μs	3.33μs	4.00μs	4.67μs	5.33μs	6.00μs
DEP	1.28±0.02	1.23±0.02	1.22±0.02	1.21±0.02	1.21±0.02	1.20±0.02	1.20±0.02	1.20±0.02	1.19±0.02
Bi212	12.8±0.17	11.1±0.15	9.99±0.13	9.22±0.12	8.42±0.11	7.95±0.11	7.43±0.10	6.93±0.09	6.60±0.09
ROI	1.49±0.01	1.38±0.01	1.35±0.01	1.34±0.01	1.33±0.01	1.33±0.01	1.32±0.01	1.31±0.01	1.31±0.01
K40	26.3±0.20	20.5±0.10	16.9±0.10	14.6±0.10	12.8±0.09	11.4±0.08	10.2±0.07	9.40±0.07	8.82±0.06

9.5 Results

The main result of this work is the suppression of the ^{228}Th induced Compton background in the ROI using the LAr anti-Compton veto. The most convincing quantities were achieved with a photon detection threshold of 0.5p.e and the SiPMs being operated at V_{over}=2.8V. In table 9.8 the achieved suppression factor of the distinct regions in the ^{228}Th spectrum are listed. The region of interest was suppressed by a factor 4.15. with the LAr anti-Compton veto.
The DEP peak is suppressed by a factor 6.2 while the neighboring Bi212 gamma line is only suppressed by a factor 1.2. The K40 peak is only suppressed by a factor 1.1. This corresponds to a signal efficiency of 92%. The fact that the DEP is suppressed strongly while the K40 is left nearly unchanged proves that the reduction of the Compton background is not due to a random coincidence.

Table 9.8: SF achieved with the LAr anti-Compton cut in the distinct regions. V_{over}=2.8V, the photon detection threshold was set to 0.5p.e

V_{over}	2.8 V
DEP	6.21± 0.09
B212	1.16± 0.01
SEP	3.79± 0.03
ROI	4.15± 0.03
K40	1.10± 0.01

In addition the segment anti-coincidence cut was applied to the spectrum. For the segment anti-coincidence cut it was required that the energy deposit in only one segment exceeds 20keV. The SFs that were achieved with the combination of the two cuts are listed in Table 9.9. Under application of both cuts the background in the region of interest was reduced by a factor of 8.58±0.07. Using the segment anti-coincidence cut the K40 peak cannot be regarded as a measure of the signal efficiency. The signal efficiency of this cut has to be received from Monte Carlo simulations.
In Fig. 9.9 the suppression of the ^{228}Th spectrum after application of the LAr anti-Compton and the combination of the LAr anti-Compton and the segment anti-coincidence is shown.

Table 9.9: SF achieved with the LAr anti-Compton and the segment anti coincidence cut in the distinct regions of the ^{228}Th spectrum. V_{over}=2.8V, the photon detection threshold was set to 0.5p.e

V_{over}	2.8 V
DEP	9.27± 0.10
B212	2.53± 0.03
SEP	10.4± 0.08
ROI	8.58± 0.07
K40	2.33± 0.02

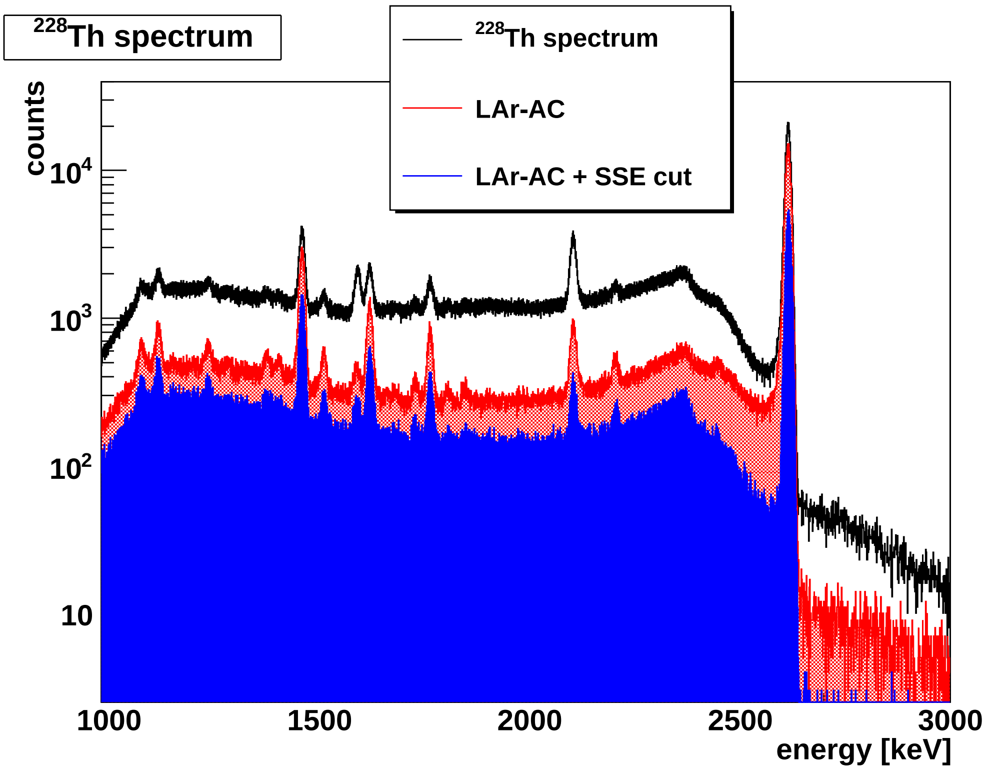

Figure 9.9: Thorium spectrum with LAr anti-Compton and segment anti-coincidence cut. A suppression of a factor 4.15 in the region of interest was achieved with the LAr anti-Compton cut and a suppression of a factor 8.58 was achieved under usage of both cuts.

Chapter 10

Summary & outlook

One of the most crucial questions in particle physics is whether the neutrino is its own anti-particle. Today the only feasible approach to answer this question is the study of the neutrinoless double beta decay. The GERDA experiment tries to observe this decay. In its first phase GERDA operates 17.66kg of enriched high purity germanium diodes in liquid argon (LAr). In Phase II new diodes that have to be produced will be added.
The required background index in phase I is planned to be less than 10^{-2} events/(kg keV year). It is planned to reach this background level with passive shielding and existing background recognition techniques. For phase II a background level of less than 10^{-3} events/(kg keV year) is required. For such a low background index new background recognition methods have to be implemented in GERDA.

In [1] it was shown that with a LAr anti-Compton veto that uses PMTs more than one order of magnitude background suppression can be achieved in HPGe detectors. However the usage of PMTs holds some disadvantages. The most prominent disadvantage is the contribution to the radioactive background which is due the components of PMTs.
In this work it has been demonstrated that the combination of SiPMs with wavelength shifting fibers is a viable alternative to large area PMTs for the detection of light in large volume LAr experiments. It was shown that the SiPMs made by Hamamatsu can be operated directly submerged in the cryo-liquid without major problems. The devices survived many cooling cycles without deterioration of their performance. It is worthwhile to note that these SiPMs can be operated at low temperatures with high gain and negligible dark rate.
A small scale LAr spectrometer using SiPMs and WLS fibers was built at the MPI für Physik, München. A light detection efficiency of roughly 90p.e./MeV energy deposit was achieved. This is competitive with light detection efficiencies achieved with PMTs [46]. The setup was successfully operated as an anti-Compton veto for a six fold segmented HPGe detector. A suppression of the thoriumbackground by a factor 4.2 in the region of interest was achieved. Together with a segment anti-coincidence veto a background suppression of 8.6 was achieved. The veto efficiency differs from the one in [46] due to different source positions and the active volume of the LAr.

The suppression factor of the LAr anti-Compton veto described in this work is limited by escaping gammas from the active LAr volume (8cm dewar radius compared to 18cm mean free path of 2.6MeV gammas in LAr).
The setup described in this paper was built with regard to the needs of GERDA. It is expected that the radioactive background induced by this solution is much smaller than the equivalent setup with PMTs. The weight of the WLS fibers used in this experiment is only about 16g. The holders and optical couplings can be further optimized and built from low activity materials. The activity of the materials needed for this setup is currently under evaluation. The full potential of the LAr anti-Compton veto based on SiPMs and WLS fibers is not reached yet. The setup used in this work suffered from the quality of the argon.
A future setup should focus on the purity of the LAr. Further the effect of attenuation in the fiber could be reduced, using many short fibers. The usage of larger area SiPMs to which multiple fibers are connected would allow to keep the number of electronic channels low.
Simulations could be performed to find out an ideal geometry of the light cavity and the WLS fibers.

Appendix A

Calculations on the SiPM linearity

In the following the response function of a SiPM to an arbitrary number of photons is calculated. Correction curves are provided.
For the calculations it will be assumed that all photons always hit the SiPM chip and no photon is lost. It will be further assumed that the probability to detect a photon is the same for all pixels. Second order effects like cross-talk, dark rate and afterpulses will be neglected.
If a SiPM is illuminated with exactly one photon the probability to detect this photon is given by the PDE. The probability for a given pixel to detect this photon and thus to fire is

$$\frac{\mathrm{PDE}}{\mathrm{N_{pix}}} \tag{A.1}$$

with $\mathrm{N_{pix}}$ being the total number of Pixels.
The probability for this pixel not to fire is thus

$$1-\frac{\mathrm{PDE}}{\mathrm{N_{pix}}} \tag{A.2}$$

If it is assumed that the SiPM is not illuminated with one, but with n photons the probability for the given pixel not to fire is

$$\left(1-\frac{\mathrm{PDE}}{\mathrm{N_{pix}}}\right)^{\mathrm{n}} \tag{A.3}$$

Accordingly the probability for this pixel to fire is

$$1-\left(1-\frac{\mathrm{PDE}}{\mathrm{N_{pix}}}\right)^{\mathrm{n}} \tag{A.4}$$

The expectation value $<\mathrm{k(n)}>$ for the number of pixels that fire if the SiPM is illuminated by n photons is thus

$$<\mathrm{k(n)}>=\mathrm{N_{pix}}\cdot\left(1-\left(1-\frac{\mathrm{PDE}}{\mathrm{N_{pix}}}\right)^{n}\right) \tag{A.5}$$

With N_{pix} being much bigger than PDE the formula can be rewritten into

$$< k(n) >= N_{pix} \cdot \left(1 - \exp\left(n \cdot \ln\left(\frac{N_{pix} - PDE}{N_{pix}}\right)\right)\right) \tag{A.6}$$

$\ln(1 + x) \approx x$ for small x. Because $N_{pix} >> PDE$ the final result can be written into

$$< k(n) >\approx N_{pix} \cdot \left(1 - \exp\left(-\frac{n \cdot PDE}{N_{pix}}\right)\right) \tag{A.7}$$

The formula can be checked by examining some limits.

$$\lim_{n \to 0} < k(n) >= 0 \tag{A.8}$$

$$\lim_{n \to 1} < k(n) >= PDE \tag{A.9}$$

$$\lim_{n \to \infty} < k(n) >= N_{pix} \tag{A.10}$$

Bibliography

[1] M. Di Marco et al., *LArGe: Background suppression using liquid argon (LAr) scintillation for $0\nu\beta\beta$ decay search with enriched germanium detectors*, Nucl.Phys.Proc.Suppl. **172:45-48,2007** (Nucl.Phys.Proc.Suppl.172:45-48,2007).

[2] Wolfgang Pauli, *Scientific Correspondence with Bohr, Einstein and Heisenberg*, Springer, 1985.

[3] CL. Cowan et al., *Detection of the free neutrino: A Confirmation*, Science **124** (1956), 103–104.

[4] Carlo Giunti et al., *Neutrino Mixing*, (2007).

[5] G. S. King, *Neutrino mass*, Contemporary Physics **48** (2007), no. 4, 195–211.

[6] A. Caldwell et al., *Signal discovery in sparse spectra: a Bayesian analysis*, Phys.Rev.D **74:092003,2006**.

[7] D. Fang et al., *Running sums for $2\nu\beta\beta$ decay matrix elements within the quasiparticle random-phase approximation with account for deformation*, Phys. Rev. C **81** (2010), no. 3.

[8] C. Arnaboldi et al., *Results from a search for the $0\nu\beta\beta$-decay of ^{130}Te*, Phys.Rev.C **78:035502,2008** (2008).

[9] C. E. Aalseth et al., *The Igex 76ge Neutrinoless Double-Beta Decay Experiment: Prospects for Next Generation Experiments, journal = Phys.Rev.D*, **65:092007,2002** (Phys.Rev.D65:092007,2002).

[10] H. V. Klapdor-Kleingrothaus et al., *Search for neutrinoless double beta decay with enriched germanium in Gran Sasso 1990-2003, journal = Physics Letters B*, **586** (2004), no. 3-4, 198 – 212.

[11] ______, *Critical view to IGEX ^{76}Ge neutrinoless double-beta decay experiment: Prospects for next generation experiments*, Phys. Rev. D **70** (2004), no. 7, 078301.

[12] I. Abt et al., *A New ^{76}Ge Double Beta Decay Experiment at LNGS*, (2007).

[13] J. Liu, *Development of Segmented Germanium Detectors for Neutrinoless Double Beta Decay Experiments*, Dissertation, Technische Universität München, München, 2009.

[14] G. F. Knoll, *Radiation Detection and Measurement*, 1999.

[15] Povh et al., *Teilchen und Kerne, Eine Einfuehrung in die physikalischen Konzepte*, Springer, 1994.

[16] K. Kröninger, *Techniques to distinguish between electron and photon induced events using segmented germanium detectors*, Ph.D. thesis, TU München, 2007.

[17] P. J. Doe et al., *Observation of tracks in a two-dimensional Liquid argon time projection chamber*, Nucl. Instrum. Methods **199** (1982), 639–642.

[18] M.J. Berger et al., *XCOM: Photon Cross Sections Database*, NIST Standard Reference Database 8 (XGAM) (2009).

[19] P. Eckert et al., *Characterisation studies of silicon photomultipliers*, Nuclear Instruments and Methods in Physics Research Section A: Accelerators, Spectrometers, Detectors and Associated Equipment **620** (2010), no. 2-3, 217 – 226.

[20] *Hamamatsu Photonics K.K., Multi-Pixel Photon Counter Catalogue (2008)*.

[21] H. Otono et al., *Study of MPPC at Liquid Nitrogen Temperature*, Proceedings of Science (2007).

[22] ______, *Study of the internal mechanisms of Pixelized Photon Detectors operated in Geiger-mode*, (2008).

[23] *LeCroy Europe GmbH Im Breitspiel 11, D-69126 Heidelberg, Phone Sales: + 49 6221 82700, Fax Sales: +49 6221 834655 Fax(Sales&Service): +49 6221 834655, Email Sales: contact.gmbh@lecroy.com Web: http://www.lecroy.de*.

[24] *XIA LLC, 31057 Genstar Rd., Hayward CA 94544, Phone: (510) 401-5760, FAX: (510) 401-5761*.

[25] *Creamt Inc., 45 Union St., Tel (617) 527 6590, Fax: (617) 527-2849, Web site: http://creamt.com*.

[26] *Jorway corportaion, Wall Strret 223, Hauntington, NY 11743 USA, Tel:(631)-351-1203*.

[27] *KGW Isotherm, Gablonzer Str. 6, D-76185 Karlsruhe, Tel: 0049 72195897-0 Fax: 0049 721 95897-77*.

[28] *HAMAMATSU PHOTONICS DEUTSCHLAND, GmbH Address: Arzbergerstr. 10, D-82211 Herrsching am Ammersee, Germany*.

[29] *Physical Review D*, The American Physical Society.

[30] K. Prothmann, *Comparitive Measurements of Silicon Photomultipliers for the Readout of a Highly Granular Hadronic Calorimeter*, Master's thesis, LMU & MPI, (2008).

[31] A. Gedanken et al., *Electronic Energy Transfer Phenomena in Rare Gases*, The Journal of Chemical Physics **57** (1972), no. 8, 3456–3469.

[32] R. S. MULLIKEN, *Potential Curves of Diatomic Rare noble gas molecules and their Ions with Particular Reference to Xe_2*, THE JOURNAL OF CHEMICAL PHYSICS **52:10** (1970), 5170–5180.

[33] A. Hitachi et al., *Effect of ionization density on the time dependence of luminescence from liquid argon and xenon*, Phys. Rev. B **27** (1983), no. 9, 5279–5285.

[34] ______, *Luminescence quenching in liquid argon under charged-particle impact: Relative scintillation yield at different linear energy transfers*, Phys. Rev. B **46** (1992), no. 18, 11463–11470.

[35] T. Pollmann, *Pulse shape discrimination studies in a liquid Argon scintillation detector*, Master's thesis, Max Planck Institut fuer Kernphysik (Heidelberg), 2007.

[36] O. Cheshnovsky et al., *Temperature dependence of rare gas molecular emission in the vacuum ultraviolet*, Chemical Physics Letters **15** (1972), no. 4, 475 – 479.

[37] N. Ishida et al., *Attenuation length measurements of scintillation light in liquid rare gases and their mixtures using an improved reflection suppresser*, Nuclear Instruments and Methods in Physics Research Section A: Accelerators, Spectrometers, Detectors and Associated Equipment **384** (1997), no. 2-3, 380 – 386.

[38] M. Miyajima et al., *Average energy expended per ion pair in liquid argon*, Phys. Rev. A **9** (1974), no. 3, 1438–1443.

[39] M. Martin, *Exciton Self-Trapping in Rare-Gas Crystals*, The journal of chemical physics **54:8** (1971), 3289?3299.

[40] L. Onsager, *Initial recombination of ions*, Phys. Rev. 54 **8** (1938), 554–557.

[41] T. Doke et al., *Absolute Scintillation Yields in Liquid Argon and Xenon for Various Particles*, Jpn. J. Appl. Phys. **41** (2002), 1538–1545.

[42] S. Kubota et al., *Dynamical behavior of free electrons in the recombination process in liquid argon and krypton and xenon*, Phys. Rev. B **20** (1979), no. 8, 3486–3496.

[43] R. Acciarri et al., *Effects of Nitrogen contamination in liquid Argon*, Nucl.Phys.Proc.Suppl. **197:70-73,2009** (2008), 242.

[44] *3M Deutschland GmbH, Adress: Carl-Schurz-Strasse 1, D-41453 Neuss*.

[45] P. M. Janecek, *Optical Reflectance Measurements for Commonly Used Reflectors*, Lawrence Berkeley National Laboratory. LBNL Paper LBNL-1791E.

[46] J. P. Pfeiffer, *Liquid argon as a active shielding and coolant for bare germanium detectors: A novel background surpression method for Gerda $0\nu\beta\beta$ experiment*, Ph.D. thesis, Universitaet Heidelberg, 2007.

[47] Isadore B. Berlman, *Handbook of Fluorescence Spectra of Aromatic Molecules*, Academic Pr, 2nd edition (June 1971).

[48] Saint-Gobain, http://www.detectors.saint-gobain.com, *Scintillating Optical Fibers Brochure*.

[49] S. Korpar et al., *Silicon photomultiplier based photon detector module as a detector of Cherenkov photons*, Nuclear Instruments and Methods in Physics Research Section A: Accelerators, Spectrometers, Detectors and Associated Equipment **In Press, Corrected Proof** (2010).

[50] Hamamatsu Photonics Rupert Maier, personal coversation.

[51] R. Dolenec et al., *Tests of a silicon photomultiplier module for detection of Cherenkov photons*, Nuclear Instruments and Methods in Physics Research Section A: Accelerators, Spectrometers, Detectors and Associated Equipment **In Press, Corrected Proof** (2010).

[52] Particle Data Group, *Particle physics booklet*, IOP Publishing, 2010.

[53] *Westfalen AG, Adress: Industrieweg 43, D-48155 Münster, Web: http://www.westfalen-ag.de/technische/argonproduktion.php*.

[54] E. Pomarico et al., *Room temperature photon number resolving detector for infared wavelengths*, Opt. Express **18** (2010), no. 10, 10750–10759.

[55] D. N. McKinsey et al., *Detecting ionizing radiation in liquid helium using wavelength shifting light collection*, Nuclear Instruments and Methods in Physics Research Section A: Accelerators, Spectrometers, Detectors and Associated Equipment **516** (2004), no. 2-3, 475 – 485.

[56] *User's Manual Digital Gama Fidner (DFP), PIXIE-4 XIA LLC*, 1.14 ed., 02 2007.

[57] Richard B. Firestone, *Tables of Isotopes*, Wiley-Interscience, 1999.